Microstructure and properties of powder metallurgical manufactured V-rich V-Si-B alloys for high-temperature application

Dissertation

zur Erlangung des akademischen Grades

Doktoringenieurin

(Dr.-Ing.)

von M.Sc. Janett Schmelzer

geb. am 28.07.1983 in Staßfurt

genehmigt durch die Fakultät für Maschinenbau

der Otto-von-Guericke-Universität Magdeburg

Gutachter:

Prof. Dr.-Ing. Manja Krüger

Prof. Kyosuke Yoshimi

Prof. Dr.-Ing. Martin Heilmaier

Promotionskolloquium am 08.02.2022

Kurzfassung

Zur Verbesserung des thermodynamischen Wirkungsgrades von Gasturbinen wird gezielt an neuen Hochtemperaturwerkstoffen, die über die Möglichkeiten von Nickelbasis-Superlegierungen hinausgehen, gearbeitet. Neben der Möglichkeit der Nutzung von hochschmelzenden Elementen bietet auch der Aspekt der Gewichtsreduzierung einen möglichen Ansatz, um das Ziel einer erhöhten thermodynamischen Effizienz zu erreichen. Vanadium zeichnet sich als interessanter Kandidat ab, da es im Vergleich zu anderen hochschmelzenden Metallen die geringste Dichte (ϱ = 6,11 g/cm^3) aufweist. Darüber hinaus entsteht in Legierung mit Silizium und Bor ein mehrphasiges Gefüge, welches aus einer V-Mischkristallphase (V_{ss}) und den intermetallischen Phasen V_3Si und V_5SiB_2 besteht und damit neben einer verbesserten Oxidationsbeständigkeit auch eine erhöhte Hochtemperatur- und Kriechfestigkeit bietet. In der vorliegenden Arbeit wird eine detaillierte Untersuchung des V-Si-(B) Pulverwerkstoffs hinsichtlich des Legierungsdesigns, des Mahlverhaltens beim mechanischen Legieren, der Gefügeentwicklung, Phasenbildung, der mechanischen Eigenschaften sowie der Verarbeitbarkeit des Pulverwerkstoffs vorgestellt. Der Mahlprozess wird im Hinblick auf die Mechanik und Kinematik der Planetenkugelmühle detailliert erläutert und numerische Berechnungen sowie eine numerische Simulation des Energieeintrags beim Mahlen vorgestellt. Das maßgeschneiderte, vorlegierte V Si(-B) Pulvermaterial wurde über zwei verschiedene pulvermetallurgische Verarbeitungsrouten, genauer mittels einem standardisierten feldunterstützten Sinterverfahren (FAST) und einem innovativen generativen Fertigungsverfahren (L-DED), kompaktiert und miteinander verglichen, um Mikrostruktur-Eigenschaftsbeziehungen zu ermitteln. Im Vergleich zu konventionell verwendeten Strukturwerkstoffen wie CMSX-4 und intermetallischen Legierungen auf TiAl-Basis erweist sich der Werkstoff V-Si-B als konkurrenzfähig in Bezug auf Härte, Festigkeit und Kriechfestigkeit.

Abstract

For improving thermodynamic efficiency of aircraft turbines it is necessary to develop new high temperature materials beyond the capability of Ni-based superalloys. Next to a high melting point the weight component is also an approach to achieve the target of increased thermodynamic efficiency. Vanadium points out as an interesting candidate, since it offers the lowest density (ϱ = 6.11 g/cm^3) in comparison to other high-melting point metals. Moreover, alloyed with Si and B a multiphase microstructure, consisting of a V solid solution (V_{ss}) phase next to the intermetallic phases V_3Si and V_5SiB_2 arises and offers enhanced high temperature strength and creep resistance next to an improved oxidation resistance. In the present thesis a detailed investigation on V-Si-(B) powder material in terms of alloy design, milling behavior during mechanical alloying, microstructural evolution, phase formation, mechanical properties as well as processabilty of the powder material is presented. The milling process is explained in detail with respect to the mechanism and kinematics of the planetary ball mill and numerical calculations as well as a numerical simulation of the energy input during milling are presented. Tailored pre-alloyed V-Si(-B) powder material was consolidated via two different powder metallurgical processing routes, namely a standardized field assisted sinter process (FAST) and an innovative generative manufacturing process (L-DED), and compared against each other in order to determine microstructure-property relationships. Compared to conventionally used structural materials such as CMSX-4 and TiAl-based intermetallic alloys, the V-Si-B material proves to be competitive in terms of hardness, strength and creep resistance

Contents

Figures

Tables

Abbreviations and symbols

Abbreviations

eV	Electronvolt
AM	Additive manufacturing
bcc	Body centered cubic
BDTT	Brittle-to-ductile transition temperature
BSE	Backscattered electrons
DED	Directed energy deposition
DEM	Discrete Element Method
DFT	Density-functional theory
EBSD	Electron backscatter diffraction
EDM	Electrical discharge machining
EDS	Energy dispersive X-ray spectroscopy
FAST	Field assisted sintering technology
FIB	Focused ion beam
FWHM	Full width at half maximum
GA	Gas atomization
HIP	Hot isostatic pressing
HT	Heat treatment
IM	Ingot metallurgy
ICP	Inductively coupled plasma
KAM	Kernel average misorientation

L-DED	Laser directed energy deposition
L-PBF	Laser powder bed fusion
MA	Mechanical alloying
MIM	Metal injection moulding
Mo_{ss}	Molybdenum solid solution
ODS	Oxide dispersion strengthening
OES	Optical emission spectrometry
PCA	Process control agents
PIPS	Precision ion polishing system
PM	Powder metallurgy
RT	Room temperature
SE	Secondary electron
SEM	Scanning electron microscopy
SLS	Selcetive laser melting
SS	Stainless steel
TEM	Transmission electron microscopy
V_{ss}	Vanadium solid solution
WC	Tungsten carbide
XRD	X-ray diffraction analysis

Symbols

ε_b	Size effect
F_f	Frictional force

ω	Angular frequency
T	Circular path time
k	Gear ratio planetary ball mill
SE	Stressing energy
SF	Frequeny of stressing
T	Temperature
T_m	Melting temperature
Q	Activation energy
$\dot{\varepsilon}$	Strain rate
Ψ	Sphericity
J_D	Number of mass particles passing a unit area per unit of time
k	Grindability
kp	Comminution rate
ffc	Flowability coefficient
$W_{s,B}$	Comminution law
A_i	Correction factor
W_{ic}	Modified work index
E_{Kano}	Impact energy
HV	Vickers hardness
a	Lattice parameter
G	Shear modulus
n	Stress or creep exponent
Q	Activation energy

B	Experimentally determined constant
ε_c	Critical shear stress
R_e	Yield point
σ_0	Resistance to dislocation motion in the grain
d	Diameter
σ	Stress
α	Constant
M_T	Taylor factor
ρ	Dislocation density
r	Radius
m	Mass
μ_s	Coefficient for friction
e	Coeeficient of restitution
λ	Wave length

1 Motivation and objective

There nearly is no other industry placing such high demands on materials as aircraft construction. Modern aircraft engines outperform in terms of mileage and service-life of all other types of drive. Nevertheless, improvements are constantly being sought, and research activities in this area want one thing above all: Lighter, quieter, more robust, reliable and powerful engines that also consume less fuel and burn with less residue. In the recent decades, engines have been developed that meet these market requirements more and more and have therefore achieved a high level of technical perfection. Due to the mature design, the further competition will take place with innovative materials and manufacturing processes [1]. Figure 1 shows a state-of-the-art aircraft turbine. For engine parts that are faced with moderate temperatures (> 500 °C) like the fan and the low-pressure compressor materials such as Ti, Ni, Mg, Al, steel and polymer- or ceramic-matrix composites find application [2]. In the vicinity of the combustor, where engine parts (high-pressure compressor, high- and low-pressure turbine) are exposed to a higher thermal load (temperatures > 500 °C), Ni-based superalloys have been state-of-the-art for many years, since they are characterized by high creep and fatigue strength as well as good oxidation resistance up to elevated temperatures of 1100 °C [3]. However, Ni-based superalloys come along with a high density (~ 8.5 g/cm^3) which is a drawback for flying applications. Weight reduction concepts are a decisive factor in increasing the efficiency of aircraft engines.

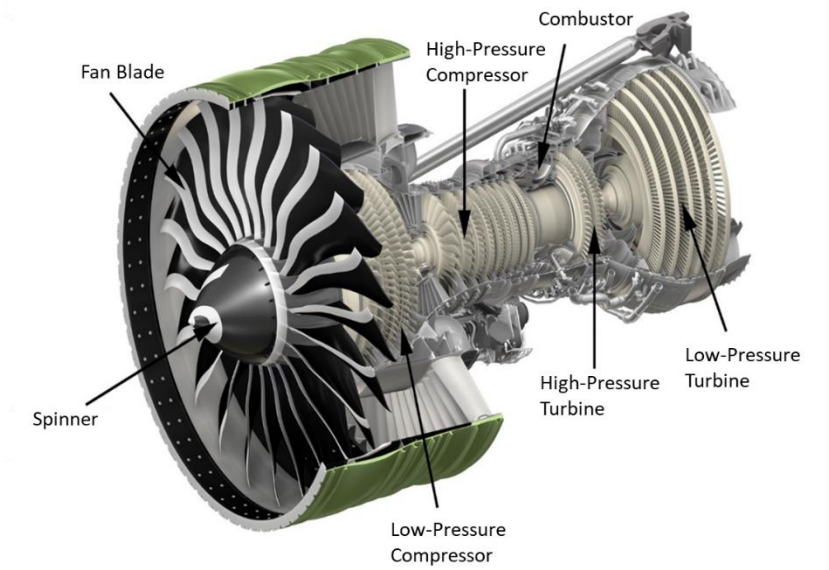

Figure 1.1: Aircraft turbine with a view on the individual components [4].

A density reduction of rotating components (i.e. turbine blades) would lead to a decreased moment of inertia and thus to a significant increase of efficiency [5]. Furthermore, a weight reduction of the components anyway results in less fuel consumption and a reduced amount of exhaust emissions. To this end, research activities focus on new light-weight materials with good high temperature properties to increase the thrust-to-weight ratio in aircraft engines by replacing Ni-based superalloys. In the last decades TiAl-based intermetallic alloys have been developed successfully as materials for high temperature structure applications and point out with their low density ($\varrho_{\gamma\text{-TiAl}} = 4$ g/cm^3) and high specific strength up to temperatures of 800 °C [6], [7].

New light-weight γ-TiAl alloys entered service with its first large-scale use on the commercial GEnx engine in 2011, which powers the Boeing 787 and Boeing 747-8 aircraft, and leads to a significant component weight reduction of ~ 40 % in comparison to blades (low-pressure turbine) out of conventionally used Ni-based superalloys [1], [4], [5]. However, TiAl-based intermetallic alloys are limited in their application temperature of max. 800 °C [8], [9].

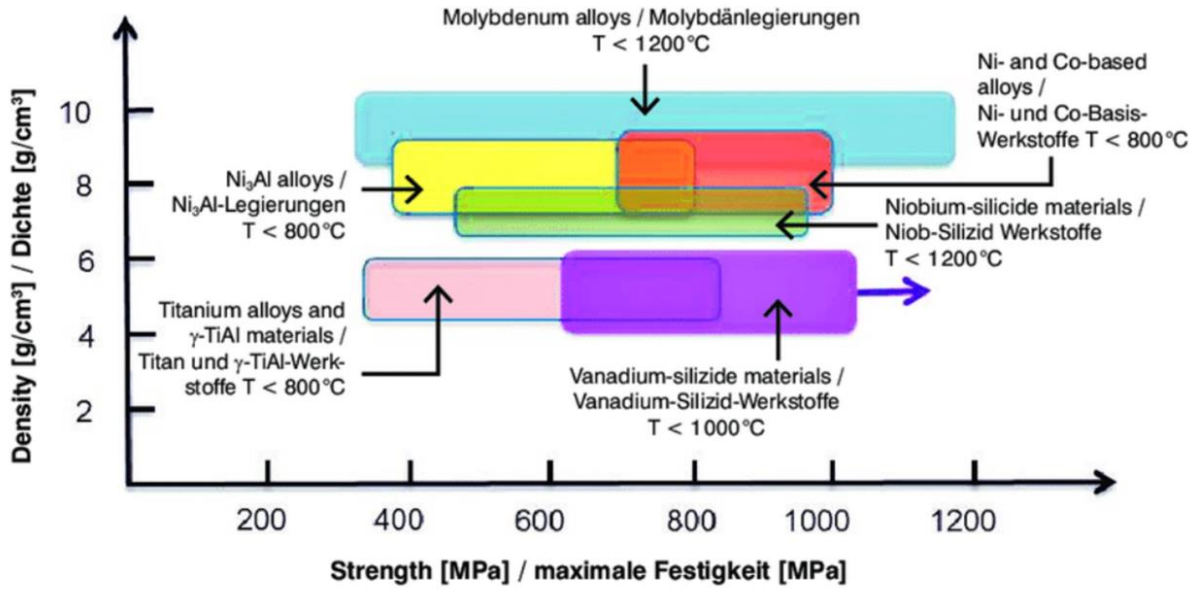

Figure 1.2: Strength potential and operation temperature of different metallic high temperature materials [10].

To overcome this problem, alloys based on vanadium could represent an innovative alternative. Vanadium points out with the lowest density of the high-melting point metals (6.1 g/cm^3). Vanadium alloys, such as V-9Si-13B [10], [11], are characterized by a good high temperature strength and a low density ($\varrho_{V\text{-base}} = 4{,}8 \ldots 6{,}2$ g/cm^3) which is comparable to TiAl materials (highlighted in Figure 1.2). The high melting point of vanadium ($T_{m,V} = 1910$ °C) and it`s silicides (e. g. $T_{m,V3Si} = 1925$ °C) may allow structural applications beyond the capability of TiAl-based intermetallic alloys [10]. Hence, in addition to recently discovered low-density, refractory high entropy alloys (e.g. Cr–Nb–Ti–V–Zr system, $\varrho \sim 6.5$ g/cm^3) [9], vanadium silicides are of central scientific interest.

The overriding objective of the present work is to investigate the potential of vanadium silicides for application as high temperature structural material. So far, little research has been done on V-based alloys and evidence for a possible use is referred to fuel element casings of V-Cr-Ti or V-Si-Ti alloys [12]–[14]. Basic research on V-based alloys, such as V-rich V-Si-B alloys (e.g. V-9Si-13B, V-9Si-5B), is currently being carried out mainly by the Krüger group [11], [15], [16]. However, many things still need to be fully clarified or holistically examined. This work aims to minimize the existing gaps in scientific studies on the Powder Metallurgical (PM) processing of V-rich V-Si-B alloys and to provide an overview of previously published studies on this class of material complemented by fundamental results on microstructure-property relationships from different PM routes. For this purpose, studies are first carried out on different V-Si and V-Si-B powder materials prepared by Mechanical Alloying (MA) to gain knowledge about the powder properties and phase formation of the alloy system. While Chapter 4 gives a detailed insight into the kinematics of the planetary ball mill and numerical calculations as well as simulations of the MA process, Chapter 5 provides in-depth investigations on the V-based powder material. Alloyed powder materials with different Si and B concentrations were investigated with respect to their milling behavior and microstructural evolution as well as properties before and after thermal treatment.

However, the use of innovative materials in industry is often limited by the manufacturing technology [17]–[20]. In particular, high-melting points and brittle materials such as vanadium silicide alloys can only be produced with great effort using conventional processes such as casting and forging. A powder metallurgical processing route characterized by solid state reactions could be a promising manufacturing route for this high temperature material. The resulting microstructure as well as investigations on the mechanical properties of a PM V-9Si-5B alloy, manufactured via Field Assisted Sintering Technology (FAST), are presented in Chapter 6. Furthermore, this work introduces a completely new and innovative manufacturing process for this class of materials with the use of Additive Manufacturing (AM). AM processes offer significant potential for extending the manufacturing limits in terms of cost efficiency and near-net-shape technology [18]. The printability of a near eutectic V-9Si-5B alloy using Laser - Direct Energy Deposition (L-DED) as a method for AM is presented in Chapter 6. Furthermore, due to increased requirements on the powder material for AM, V-9Si-5B powders manufactured by means of a gas atomization process are also presented (Chapter 6). Detailed investigations on the microstructural evolution of both manufacturing processes (FAST; L-DED) are carried out and compared to each other as well as to literature. In addition, in Chapter 6 initial mechanical properties at room and elevated temperatures as well as the oxidation behavior at 600 °C and 900 °C were investigated and compared. The results are critically discussed in order to show the effects of the different manufacturing processes on the microstructure property relationships and to evaluate the potential of V-rich V-Si-B alloys (e.g. V-9Si-5B) as possible new light-weight high temperature structural materials. Finally, Chapter 7 summarizes the most important points and offers some interesting prospects that should be followed up in future work.

2 Vanadium based alloys for high temperature applications

As mentioned before, V-based alloys gain more and more interest as structural materials for high temperature applications. So far, low alloyed V-4Cr-4Ti alloys or particle strengthened V-10Nb-2.6Zr-0.35C material mainly appear as structural materials for fusion reactors because of their low activation properties, high thermal stress factor and good mechanical properties such as high strength at intermediate temperatures (up to 700 °C) as well as ductility at low temperatures [12], [21]–[23]. Current research interest and also this work, however, are focused on V-rich V-Si-B alloys for the reasons mentioned in Chapter 1. Since V-Si-B alloys for high temperature applications have been little studied, this chapter summarizes the knowledge gained so far on binary V-Si and ternary V-Si-B materials (for use as high temperature structural material). The influence on the microstructural evolution and resulting material properties caused by different manufacturing processes was taken into account.

2.1 The binary V-Si system

According to Figure 2.1 the V-Si system provides the following phases, considering equilibrium conditions: V_{ss}, V_3Si, V_5Si_3, V_6Si_5, and VSi_2. The maximum solubility of Si in the cubic body centered vanadium is approximately 7 at. % at 1870 °C and decreases below 4 at. % at room temperature. Manufacturing processes like rapid solidification process or mechanical alloying (MA), evoking a non-equilibrium state, enable the formation of supersaturated V_{ss} phases with Si concentrations of more than 7 at.%. Solid solution formation often leads to hardening of the phase which is usually accompanied by embrittlement [24]. Investigations of Hasemann et al. [16] observed, however, room temperature plasticity under compressive loads for V_{ss} (manufactured via arc-melting) with Si concentrations ranging from 1 at. % to 7 at. %. A low brittle-to-ductile transition temperature (BDTT) for single phase V_{ss} (with Cr, Ti, and Si additions) in the range between -250 °C and 250 °C was also mentioned in [25] and thus emphasizes the benefit of the V_{ss} phase as a constituent in structural materials. The intermetallic phases V_3Si, V_5Si_3, VSi_2 are formed via congruent transformations. V_6Si_5 is a product of a peritectic reaction ($L+V_5Si_3 \leftrightarrow V_6Si_5$), decomposing in eutectoid manner at lower temperature ($V_6Si_5 \leftrightarrow V_5Si_3+VSi_2$) [26]. In contrast to the stoichiometric V_5Si_3, V_6Si_5 and VSi_2, V_3Si has an important range of solubility (ranging from Si solubility of 19 at. % to 25.5 at.%). Stoichiometric V_3Si melts congruently at 1925 °C and is stable at high and low temperatures [27]. Within the system four eutectic reactions are found: $L \leftrightarrow (V_{ss}) + V_3Si$; $L \leftrightarrow V_3Si + V_5Si_3$; $L \leftrightarrow V_6Si_5 + VSi_2$; and $L \leftrightarrow VSi_2 + (Si)$ [26].

Of particular interest are the stable silicides in the V-rich region, namely V_3Si and V_5Si_3. V_3Si is an intermetallic phase with an A15 crystal structure (according to Strukturbericht) and can be

assigned to the Frank Kaspar phases which is a complex, cubic structure derived from the bcc lattice (A2) with 8 atoms per unit cell [28]. The processing of V_3Si is very difficult as it shows hard and brittle behavior. The reason for this is the electronic structure of the V_3Si phase which leads to strong covalent bonding between the nearest neighbor V atoms [29]. V_3Si provides a high Young's modulus of 213 GPa [30] and a BDTT of about 1200 °C [31]. The creep behavior is characterized by subgrain formation, a dislocation climb controlled creep rate and a comparatively high activation energy of 2-11 eV/atom depending on the stress, temperature, and the composition [32]. V_3Si is of interest for application because of its superconducting properties and its high stability [33]. Recently, it gains more attention for structural, high temperature applications. Investigations from Bei et al. [22] observed a noteworthy second phase hardening effect in eutectic V_{ss}-V_3Si alloys due to the presence of the intermetallic V_3Si phase. This approach seems to be promising. A balanced combination of the ductile V_{ss} phase and the high-strength silicide phase V_3Si might overcome the brittleness problem [22], [28].

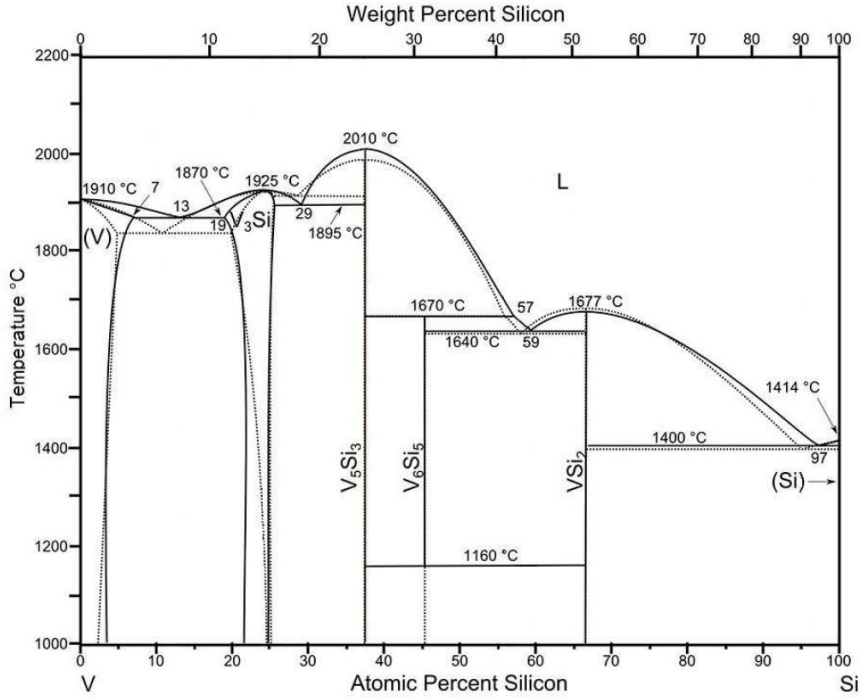

Figure 2.1: V-Si phase diagram [26] based on data from Smith [34], supplemented by thermo-dynamic results from Zhang et al. [35] (black dashed lines).

For the V_5Si_3 phase, there are two prototype structures. The stable $D8_m$ structure and the $D8_8$ structure which is assumed to be stable only in the ternary system, since its appearance depends on the presence of interstitial impurity atoms such as carbon, boron or nitrogen [36], [37]. This stabilized $D8_8$ structure belongs to the Nowotny phases, which are characterized as so-called filled Mn_5Si_3 structures [38]. Physical properties of the V_5Si_3 phase, in particular the anisotropic thermal expansion [39] and in comparison to other vanadium-based compounds a good oxidation resistance are known [40]. With increasing Si concentrations, the silicides, such as the V_6Si_5 and VSi_2, show lower metallicity by forming more readily continuous Si chains or networks in the

crystal lattice. This changes the type of bonding and results in a lower electrical conductivity, since the Si atoms are no longer isolated [28]. While the V_6Si_5 phase decomposes at 1160 °C , VSi_2 is stable and crystallizes with a hexagonal C40 structure [41]. VSi_2 exhibits a brittle behavior up to 400 °C and shows a drop of tensile strength in the temperature range of 300 °C to 600 °C from 250 MPa to <100 MPa [42]. VSi_2 is of interest to be applied in electronic devices and with this regard investigations on its thin-film formation reactions have been carefully carried out [43].

2.2 The ternary V-Si-B System

Up to now, the ternary V-Si-B system has tended to gain less interest in the field of high temperature materials, but is currently attracting more and more attention, particularly through the activities of the Krüger Group [11], [15], [16], [44], [45]. Early investigations on the V-Si-B phase diagram can be referred to Kudielka and Nowotny [46]. Their investigations revealed phase equilibria between V_5SiB_2-VB, V_5SiB_2 and V_5SiB_2-V_5Si_3-$D8_8$, where the $D8_8$ phase represents B-stabilized V_5Si_3, and were summarized in a partial isothermal section of the V-Si-B system at 1450 °C. Investigations on the V-rich V-Si-B system were also carried out by Nunes et al. [47] by interpreting various alloy compositions after annealing with regard to their phase equilibria. They postulated an isothermal section of the V-Si-B system at 1600 °C (see Figure 2.2) which confirms the stability of the ternary V_5SiB_2 (also referred as T2 phase with a $D8_1$ structure) and B-stabilized V_5Si_3 ($D8_8$ structure), with T2 having an important solubility range. Recently, Da Silva et al. [48] presented a ternary V-Si-B system thermodynamically modeled by means of the CALPHAD method. Their calculations based on data from literature of the V-Si and B-Si binary systems [35], [49], [50] augmented by re-evaluated parameters of the binary V-B system, which bases on new experimental information.

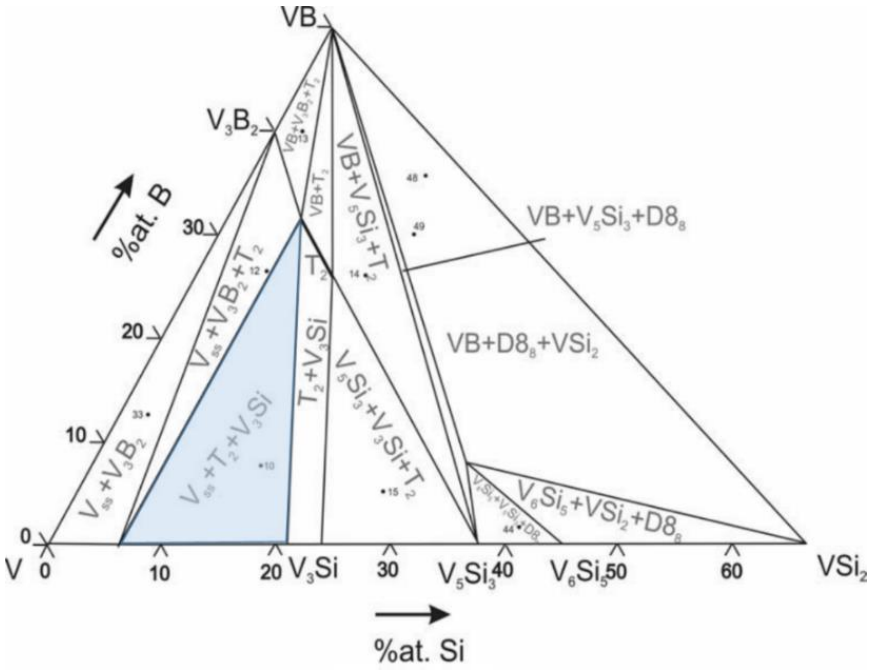

Figure 2.2: Isothermal section of the V-Si-B system at 1600 °C in the V-rich V-VSi_2-VB region [47].

Out of their investigations a calculation of an isothermal section at 1600 °C arises which is in good agreement with their experimental results as well as the isothermal section of the V-Si-B system at 1600 °C presented by Nunes et al. [47]. Kudielka et al. [46] identified V_5SiB_2 (T2) having the same Si/B ratio as compared to isomorphous Mo-Si-B systems [41], [51]–[53]. Furthermore, the Mo- and V-rich corners of the respective phase diagrams provide similar crystal structures, namely an A2 structured metal solid solution phase (Mo_{ss} and V_{ss}) and the silicides with an A15 crystal structure (Mo_3Si and V_3Si) and the $D8_1$ structured ternary phases (Mo_5SiB_2 and V_5SiB_2). This fact leads to the assumption that alloy concepts of the previously well-studied Mo-Si-B system can be transferred to V-Si-B alloys, such as investigated in [45].

As it has been widely reported that the mechanical strength of typical vanadium solid solutions drops at temperatures between 600 °C and 800 °C depending on the concentration of solute elements, second phase strengthening helps to improve the strength level at intermediate temperatures, but there is still a pronounced drop at temperatures above 800 °C [15]. The volume fraction of the phases (V_{ss}, silicides) as well as the evolution of the microstructure are decisive. From investigations of the isomorphous Mo-Si-B system microstructure property relations are well known and can be divided roughly into two groups [54]:

I. Alloys having a large and coarse volume fraction or even a continuous solid solution matrix with homogeneously distributed intermetallic/silicide phases. This combination of microstructural constituents provides high fracture toughness due to the predominant influence of the ductile solid solution phase. Intermetallic phases cause second phase strengthening. However, taking into account that reduced amount of intermetallic phases, those alloy compositions suffer from decreased oxidation and creep resistance.

II. Alloys providing a silicide matrix with a small or near zero volume fraction of a discontinuous solid solution phase. The predominant presence of the silicides contribute to the strength, creep and oxidation resistance but induces at the same time embrittlement.

A well-suited Mo-Si-B microstructure consists of a Mo_{ss} matrix phase strengthened by homogeneously distributed silicide phases, resulting in balanced mechanical properties at ambient and high temperatures [37], [38]. Similar properties are expected from alloys out of the V_{ss}-V_3Si-V_5SiB_2 phase field (blue colored triangle in Figure 2.2), which are the focus in this work. This phase field has not been studied well so far in terms of application as high temperature structural material. Both the V_{ss} and the silicides are of great importance since the V_{ss} phase has a significant influence on the ductility of the material while V_3Si and V_5SiB_2 are beneficial concerning oxidation resistance and mechanical properties such as strength and creep resistance [15]. At this time, many studies only refer to the microstructural evolution. Investigations on the ternary V_{ss}-V_3Si-V_5SiB_2 phase field in a V-10Si-6B alloy, conducted by Reis et al. [55], showed a microstructure consisting of binary eutectic V_5SiB_2-V_{ss} regions next to larger areas of the V_3Si phase. Nunes et al. [47] studied as well an alloy in this phase field (V-15Si-7.5B) manufactured via ingot metallurgy. After annealing of the V-15Si-7.5B alloy at 1600 °C a coarsened microstructure with large regions of V_3Si surrounded by small regions V_{ss} and V_5SiB_2 arises. Nunes et al. [47] confirmed the stability of the ternary T2 and $D8_8$ phases, with T2 exhibiting a solubility range.

Furthermore, a negligible B solubility in the silicide phases (V_3Si, V_5Si_3 and V_6Si_5) as well as that of Si in the borides (V_3B_2 and VB) was found [47].

Recently, an experimental study of the liquid-solid phase transformation in the V-rich portion of the V-Si-B system was published by Hasemann [56]. Hasemann carefully investigated more than 40 alloy compositions, located in the V-rich corner of the ternary V-Si-B system, in terms of their phase formation and microstructural evolution during cooling down from the liquid state. Figure 2.3 shows a comparison of the experimental results from Hasemann [56] compared to the V-Si-B liquidus projection calculated by Da Silva et al [48]. It can be stated that the experimentally obtained results are in good agreement with the liquidus surface predicted by calculations based on the CALPHAD method [48], [56]. Nevertheless, some discrepancies were found along the V_{ss}-V_3Si, V_{ss}-V_3B_2, V_{ss}-V_5SiB_2, V_3B_2-V_5SiB_2 and V_3B_2-VB two-phase reaction lines, which are discussed in detail in [56].

Figures 2.3 b) and c) give an example of the microstructures (as-cast) of V_{ss} primary solidifying alloys in the V_{ss}-V_5SiB_2-V_3Si phase field [56]. However, the formation of a microstructure consisting of a V_{ss}-V_5SiB_2-V_3Si ternary eutectic with a relatively high volume fraction of the primary V_{SS} phase, which is shown in Figure 2.3 c), should be mentioned as an important contribution from [56]. From the similar Mo-Si-B system it is known that alloys within a field of an A2 structured solid solution phase and A15 and $D8_1$ structured silicides show a balanced microstructure property relation in terms of high temperature (creep and oxidation resistance) and room temperature properties (fracture toughness), if the amount of the solid solution phase is around 50% [57], [58]. This alloy concept seems to be very promising for further investigations of the V-Si-B system with regard to its application as a low density high temperature structural material.

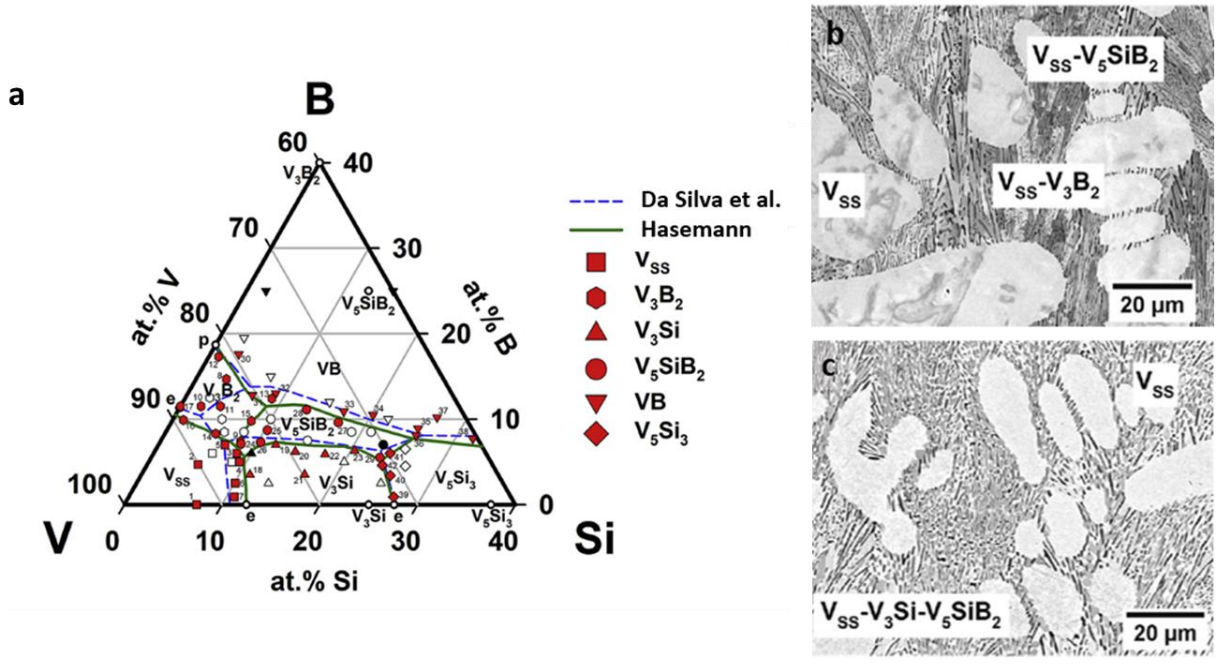

Figure 2.3: a) Comparison of the V-Si-B liquidus projection calculated by Da Silva et al. [48] with experimental results obtained by Hasemann [56] and V_{ss} primary solidifying alloys: b) V-5Si-5B, c) V-9Si-5B [56].

2.3 Review of processing and resulting material`s properties

As mentioned in Chapter 2.2 balanced properties concerning high temperature strength and oxidation resistance as well as more ductile behavior at room temperature are main goals in alloy design of future V-Si-B structural material. While the alloy composition mainly affects the phase distribution and volume fraction of the phases, the manufacturing process strongly influences the microstructure evolution and thus the mechanical properties. The following section presents the manufacturing process related microstructural evolution of V-Si-B alloys produced so far. In addition to conventional process routes covering ingot and powder metallurgy, latest research activities start to discover the additive manufacturing technology.

Ingot metallurgy

The ingot metallurgy (IM) is one of the oldest methods for metallic alloy production and includes classic methods such as casting or arc-melting. To achieve a homogenous alloy, ideally, the raw materials must be melted into a homogenized liquid before casting. High melting points or massive differences in the densities of the alloy components can result in an economic or procedural limit of the ingot metallurgical process routes [22], [55], [45]. In terms of refractory metal alloys, such as V-Si-B alloys, this might be a challenging point. Nevertheless, processing via IM enables the control and influence of the microstructural evolution in terms of phase distribution, grain size and homogeneity. Arc-melting was proven as an appropriate processing route for refractory alloys due to the possibility of achieving maximum process temperatures up to 3500 °C. However, casted alloys provide a rather coarse microstructure. Favorable microstructures of the ternary V-Si-B system possess larger primarily solidified V_{ss} regions embedded in an intermetallic matrix [56]. Representative microstructures already had been shown in Figure 2.3 b) and c) and reveal the typically larger regions of primarily solidified V_{ss} dendrites and secondarily solidified silicides or eutectic constituents [56].

There are only a few studies on the microstructure-property-relationship of casted V-Si-B material. Some only take into account the binary V-Si system like investigations of Henshall et al. [59]. Henshall studied the influence of the volume fraction of the V_{ss} phase on the fracture toughness of a V_{ss}-V_3Si eutectic structure. For a microstructure consisting of a nearly equal volume fraction of the ductile V_{ss} phase and strength V_3Si phase a promising fracture toughness was determined [59]. Investigations on the V-Si system were also conducted by Bei et al. [22]. For sample processing they used the directional solidification technique, which is a further possibility for casting, especially for high temperature materials [60]. The resulting well-aligned microstructures are said to have enhanced mechanical properties, such as a good creep resistance, due to a high amount of intermetallic phases and eutectic colonies [61]. Figure 2.4 shows the alloys processed in [22]. Figure 2.4 a) depicts a fully eutectic arc-melted V-12.6Si alloy. Subsequent directional solidification leads to a well-aligned broken-lamellar microstructure, typically arising from directional solidification, with a continuous V_{ss} phase and a discontinuous V_3Si phase which is shown in Figure 2.4 b) [22].

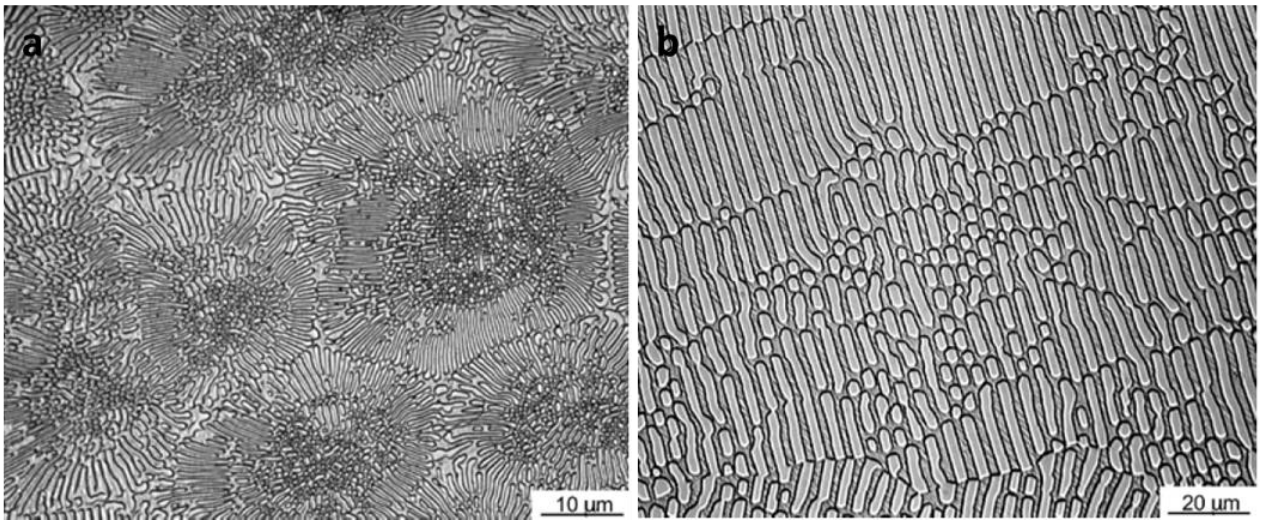

Figure 2.4: a) Fully eutectic microstructure of an arc melted V_{ss}-V_3Si (V-12.6Si) alloy and b) well-aligned broken-lamellar microstructure of directionally solidified V_{ss}–V_3Si eutectic alloy transverse to the solidification direction [22].

The lamellar binary V-V_3Si eutectic indicates a brittle to ductile transition temperature (BDTT) somewhere between 800 °C and 900 °C (BDTT of V_3Si =1200 °C [31]) [22]. Furthermore, in comparison to the solid solution alloy V-4Cr-4Ti, which is a very promising candidate for fusion reactor applications, a significant strengthening effect due to the presence of the V_3Si phase can be observed. The yield strength at a temperature of 800 °C is 250 MPa for the V_{ss} alloy while the V-V_3Si eutectic shows values of 600 MPa [22].This result clearly illustrates the benefit of the V_3Si phase on the second phase hardening effect. Thus, V_3Si is considered to be a good strengthening constituent because of its high melting point, high strength, good stability to 1965 °C, and relatively low density [22]. But at the same time it needs to be taken into account that an increase of the V_3Si phase leads to a more brittle behavior.

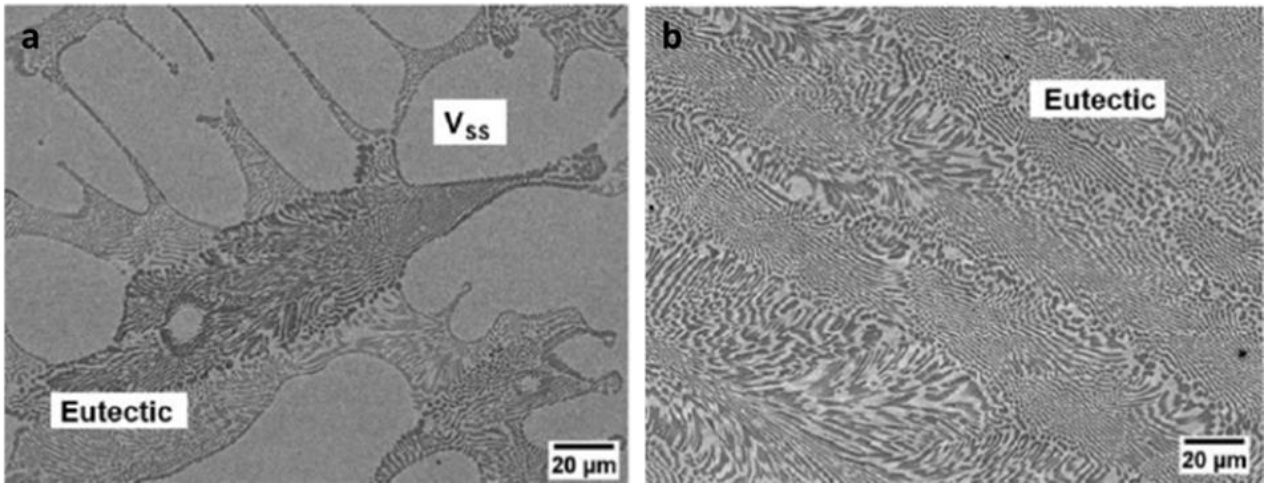

Figure 2.5: Microstructure of an a) hypoeutectic alloy V-9.75Si alloy and b) eutectic V-12.5Si alloy [62].

Current research of Regenberg et al. [62] again picked up this topic and showed results on as-cast hypo-and hypereutectic V-Si compositions with regard to the room temperature deformability. Figure 2.5 a) shows a casted hypoeutectic microstructure with larger regions of the primarily solidified V_{ss} phase surrounded by eutectic structures. Figure 2.5 b) displays the eutectic arrangement of a V-12.5Si alloy (as-cast state). Regenberg et al. [62] confirmed the above mentioned findings by showing an increase of yield strength with decreasing amount of the V_{ss} phase. However, room temperature ductility was observed for both alloy compositions [62]. This behavior might be beneficial concerning balanced strength/ductility properties for V-Si-B at room temperature.

The few studies available on investigations of the mechanical properties of casted V-Si-B alloys can be referred to Hasemann et al. [16] and Müller et al. [63]. Hasemann investigated the room temperature deformability of V-Si-B alloys and concentrates on alloy compositions located in the V_{ss}-V_5SiB_2-V_3Si phase field, which are also focused in this work. Room temperature plasticity, under compressive load, was observed for all alloys with a V_{SS} phase fraction of 30% - 100% [16]. Furthermore, Hasemann et al. [16] stated a significant influence of Si on solid solution strengthening that is not accompanied by a strong decrease in ductility. This might be favorable for balanced mechanical properties. Müller investigated the microstructure and compression properties of V_{ss}-V_3B_2 eutectic alloys in the V-Si-B system. Evaluations on an as-cast V-5Si-9B alloy after compression (at room temperature) showed as well a V_{ss} controlled deformability of the material [63]. Second phases such as silicides or intermetallics remain unaffected and act as second phase strengthener [16], [63].

Powder metallurgy

Powder metallurgy (PM) is concerned with the production of metal powders and their further processing into solid components by processes such as hot isostatic pressing (HIP), powder injection molding (MIM) and spark plasma sintering (SPS, or field-activated sintering (FAST)). Components manufactured via PM processes are characterized by a high dimensional accuracy, by a large and highly differentiated alloy diversity and a broad density spectrum, ranging from highly porous to fully dense. Corresponding to this metallurgical-technical variety, the range of applications for PM components is extraordinarily wide. Table 2.1 exhibits an overview of advantageous reasons for the use of PM processes.

Table 2.1: Advantageous reasons for the use of PM processes.

Advantage	Outcome
Near net shape production	Reduction in costs and the number of processing steps
Adjustment of microstructural properties	Design possibilities: small grain size, fine distribution of strengthening phases, porosity
Avoiding of very high melting temperatures	Energy saving
Alloying of any metallic phases and mixtures of metals with other groups of materials (e.g. oxide, carbide, polymer)	Almost unrestricted alloy design

PM processing routes typically starts from powder mixtures or mechanically alloyed (MA) powder material. Also powder processing via gas atomization route is possible, but is in comparison to mixing or MA technically more complex. According to high pre-heating temperatures and the expensive process gas, which are required to achieve homogeneous alloyed powder material, little cost efficiency occurs [64]. Via MA small powder batches in the laboratory scale as well as larger batches up to several kilograms can be produced by using ball mills or attrition mills. The MA process is aimed at comminution, homogenization and alloying of the multi-element powder mixtures up to the atomic level by forming a metastable supersaturated solid solution [65], [66]. Detailed information on the principle of MA can be found in Chapter 5. Lively research activities on vanadium powder material were carried out in the former Soviet Union in the 1970`s and 1980`s by Radomysel'skii [67], Kieffer [68] and others [69], [70] but then seemed to have lost its attractiveness. Current investigations refer mainly to the V-4Cr-4Ti powder material in terms of solid solution strengthening or particle hardening effect [13], [14], [71]. With regard to V-Si-B power material no fundamental investigations worth mentioning, apart from own investigations [44], [45] which are in detail described in Chapter 6, are available.

However, PM processes are very suitable for refractory metal alloys such as V-Si-B material, since the consolidation of the powder is conducted wide below their melting temperatures [72]. Among the sintering processes FAST, described in Chapter 3.2.1, seems to be a very promising compacting procedure. Short process cycles, due to rapid heating times, suppress grain growth and lead to micro- or even nano-scaled structures [73]. But full densification of these materials still remains a challenge not at least because the initial powder particle size has a significant influence and a possible oxygen contamination of the powder suppress the diffusion-driven mass transport during the sintering process [74]. Oxygen impurity content increases with decreasing particle size of the powder material and is as well affected by the powder processing e.g. MA, where oxygen impurities are introduced during milling. An increased oxygen content will lead to undesired embrittlement of the consolidated material [75].

For V-Si-B alloys secondary phases such as silicides or borides are formed in situ during sintering by precipitating out of the supersaturated V_{ss}. The precipitation of second phases increases the strength of the alloy due to the hindrance of dislocation movement. Another possibility for strengthening can be achieved by the addition of oxide particles to the powder material, which remain chemically unaffected during processing. This effect is called oxide-dispersion-strengthening (ODS) [72].

Currently, studies on PM V-Si-B alloys can only be found in publications of Krüger et al. [10], [11], [15]. In her research Krüger concentrates on a PM V-9Si-13B alloy. The intention of selecting this composition was to control an equalized proportion of silicide phases and solid solution phases, in order to enable a balance of high temperature strength and low temperature ductility as it is known from the related Mo-Si-B system [45].

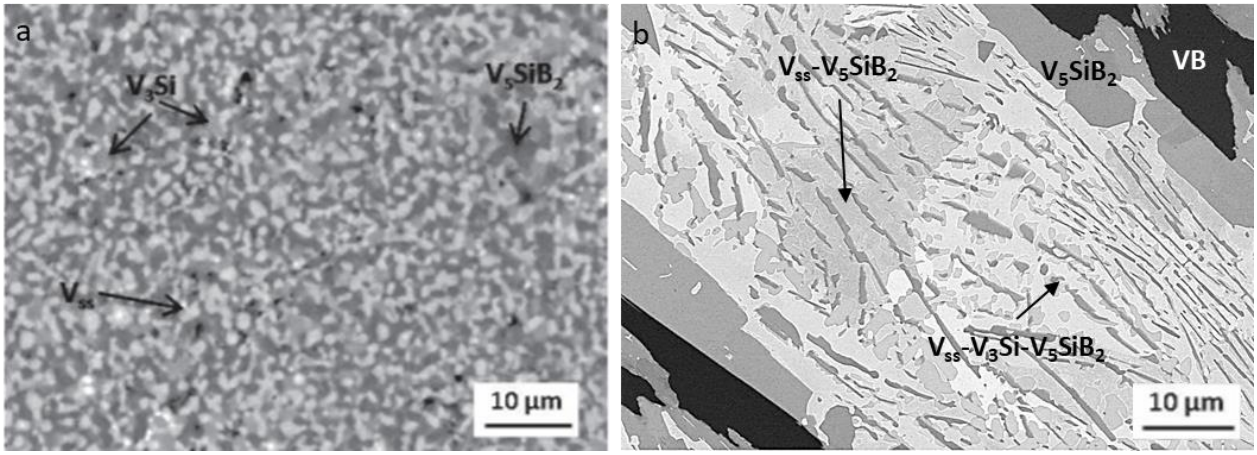

Figure 2.6: Microstructure of a) PM V-9Si-13B [10] and b) IM V-9Si-13B [56].

Figure 2.6 shows a comparison of a V-9Si-13B alloy with V_{ss}-V_3Si-V_5SiB_2 microstructure out of a PM (consolidated via FAST) and IM manufacturing processes. Process-related differences in microstructural evolution can be clearly identified. The depicted IM V-9Si-13B alloy in Figure 2.6 b) solidifies by forming a primary VB phase and a continuing solidification by forming a V_5SiB_2 phase next to binary eutectic V_{ss}-V_5SiB_2 and ternary eutectic V_{ss}-V_5SiB_2-V_3Si structures [56]. In contrast, the PM V-9Si-13B alloy (Figure 2.6 a)), consolidated via FAST, shows a finer grained microstructure where the V_{ss}, V_3Si and V_5SiB_2 are distributed homogenously due to homogenous distribution of the elementary components in the MA powder material [45]. The phase formation arose due to the precipitation of silicides (V_3Si and V_5SiB_2) out of the supersaturated V_{ss} phase during sintering. The dimensions of the individual phases are in the low micrometer range, due to the short process cycles. The advantage that PM produced alloys are not dependent on the different melting temperatures of the respective phases or the solidification path of the alloy leads to a significant different microstructural evolution in comparison to IM produced alloys. In [11], [15] first mechanical properties of a PM V-9Si-13B alloy are presented. Due to the precipitation of the silicide phases a notable strengthening of the resulting multiphase V_{ss}-V_3Si-V_5SiB_2 microstructure occurs since the silicide phases (V_3Si, V_5SiB_2) show, at a minimum, twice the hardness of V_{ss}. From compression tests a competitive flow stress of PM V-9Si-13B alloy with a commonly used high temperature CMSX-4 material (Ni-based superalloy) at 1000 °C can be derived, at lower temperatures the performance is even better [11]. Furthermore, PM V-9Si-13B provides a density of only 67 % of the density of CMSX-4 which clearly qualifies this new high temperature material.

Additive Manufacturing

The history of additive manufacturing (AM) started in 1983 in Japan when Charles Hull invented the stereolithography. In 1986 selective laser sintering (SLS) as 3D printing technique was established. Today AM is particularly used in the field of prototype construction. This new section of powder metallurgy scores with advantages such as an enormous geometric freedom, more efficient production processes and reduced costs, due to tool-less manufacturing, compared to more established PM processes. Recently, the manufacturing of end products gained more and

more attention. For manufacturing of metal powders, processes such as electron beam melting (EBM) as well as laser based AM processes like laser powder bed fusion (L-PBF) or directed energy deposition (DED) can be used. With the procedures mentioned, a limited range of metallic powder can be processed at the current time. While processing of common alloys like steel, nickel-based alloys, aluminum alloys, or cobalt alloys is state-of-the-art, manufactured parts find application in aerospace or medical industries [76]–[79], AM of refractory metals is more difficult. The high melting points hinder the production of powder material as well as the AM process itself as high thermal gradients are expected [80]. Few investigations on AM of V-based alloys have been reported, which can possibly be attributed to a lack of specialized commercial V-based powder material suitable for AM technology [81]. A first systematic study on AM of a V-6Cr-6Ti alloy was published by Jialin in [81]. Powder preparation by means of mechanical alloying as well as the subsequent consolidation via L-PBF as a method for AM were described. Figure 2.7 shows the microstructure of AM V-6Cr-6Ti exhibiting a homogenous and ultrafine grain size in comparison to IM and PM processed vanadium alloys. First investigations on mechanical properties at room temperature exhibited an increased compression strength compared to conventional manufactured V-based alloys [81], [82]. Based on the findings of Jialin [81] and comparable investigations on other material systems [77]–[79], [83], [84] laser based AM seems to be an attractive and promising AM technology for manufacturing V-Si-B material. Laser based AM might be able to efficiently overcome manufacturing challenges and can obtain novel tailored microstructures with mechanical properties that are close to or even superior to the properties achievable from conventionally processed materials [82]–[84]. In the case of V-Si-B alloys, however, there are no research activities on AM, but will be presented for the first time in this work.

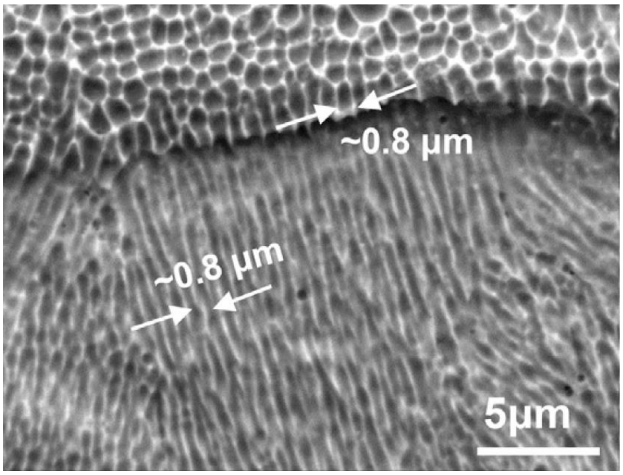

Figure 2.7: LPBF processed V-6Cr-6Ti alloy with a very fine grained microstructure [81].

2.4 Deformation and oxidation behavior of V-Si-B alloys at elevated temperatures

Rather coarse microstructures of V-Si-B material are obtained via ingot metallurgical processing routes. On the contrary, processing routes like FAST or AM reveal way finer microstructures. The manufacturing process influences the microstructural evolution in terms of

phase distribution, grain size, and homogeneity and has thus significant influence on the resulting mechanical properties. Especially for high temperature materials, properties such as creep or oxidation resistance are of importance. The following section deals specifically with material burden of V-Si-B material caused at elevated temperatures.

Creep performance

Material intended to be used as high temperature material, e.g. turbine blades, needs to withstand elevated operating temperatures in combination with tensile stresses in radial direction. In the long run, these loads cause the so-called creep of the blades. Due to that reason special attention needs to be paid on the investigation of the creep resistance of the compact V-Si-B alloys, since the materials would be faced with high temperatures as well as considerable loads for an extended period of time during their life cycle. Creep is a time-dependent, plastic deformation of a material that also occurs when the stress is lower than the yield stress. If a metallic or ceramic component is stressed at elevated temperatures i.e., at a homologous temperature T/T_m of at least 0.3 to 0.4, the strain of the component increases with time at constant load [85]. A typical schematic plot of the constant load creep curve and strain rate is shown in Figure 2.8.

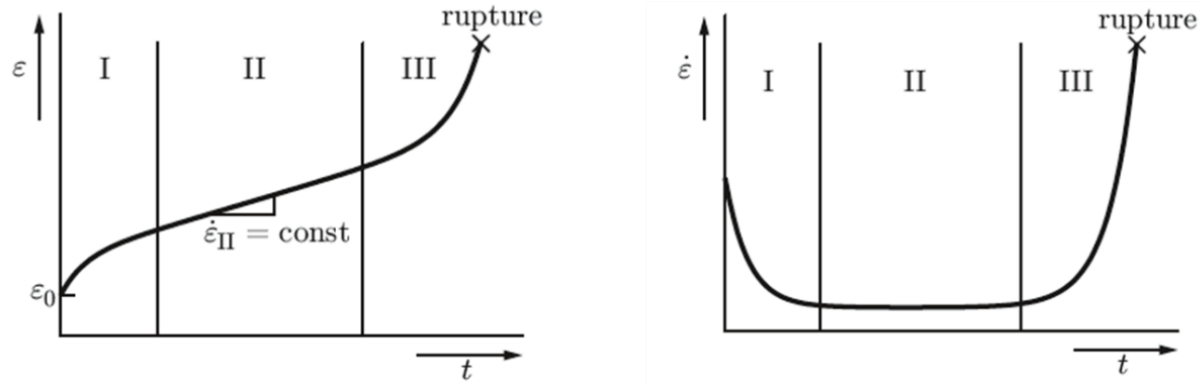

Figure 2.8: Schematic representation of (a) constant load creep curve and (b) plot of the strain rate vs. time [85].

A typical creep curve can be subdivided into three major regimes. Initially, the material shows an instantaneous time-independent strain ε_0. Strain hardening occurs over time due to the formation and interaction of dislocations. Structural changes due to the formation of subgrains (e.g. by rearrangement of dislocations) increase the resistance to dislocation motion of the material and leads to a continuously decreasing strain rate $\dot{\varepsilon}$. This region of the creep curve (region I) is called primary creep or transient creep. After this decreasing period a region (region II) of steady-state creep or secondary creep with practically constant strain rate follows. This constant (steady-state) creep rate emerges due to a dynamic balance between hardening and softening processes (dislocation multiplication and annihilation) in the lattice. After most of the life time has passed, the creep rate strongly increases until final fracture occurs. In this region of tertiary creep (region III), massive inner damage occurs in the material. This inner damage arises due to

microstructural changes such as necking, formation of grain boundary voids or intercrystalline fractures and lead to an increase of local stresses accompanied by materials failure at the end of the tertiary creep stage.

The secondary creep stage, which would persist for a considerable period of materials service life, is the most important section for technical application since the corresponding creep rate ε_2 depends on several extrinsic, intrinsic and materials parameters. This creep stage can be expressed mathematically via the so called Norton`s creep law:

$$\dot{\varepsilon}_2 = B\sigma^n exp\left(-\frac{Q}{RT}\right) \tag{2.1}$$

where B is constant, σ the applied stress, n the stress exponent (also referred as creep exponent), R the ideal gas constant (8.31 $\frac{J}{mol\ K}$), T the temperature, and Q is the characteristic activation energy for creep processes which is often similar to the self-diffusion energy of the base material [86] The creep exponent n is of major practical importance. The value of this exponent can provide information about the preferred creep mechanism in the investigated material. According to Norton`s creep law, Equation 2.1, the secondary creep rate is power law dependent with respect to the stress and depends exponentially on the temperature. The creep exponent can be graphically determined in the respective Norton plot, which is a representation of the minimum creep rate and the constant applied stress. The stress exponent (creep exponent) can be found as the slope:

$$n = \frac{\Delta log\dot{\varepsilon}}{\Delta log\sigma} \tag{2.2}$$

By means of the determined creep exponent an assignation of the occurring creep mechanism can be made. If the creep exponent can be determined with a value of 1 diffusional creep mainly affects the material. Due to the vacancy gradient between the grain boundaries migration of vacancies occurs with respect to the temperature, whereby high temperatures promote volume diffusion processes also known as Nabarro-Herring creep and lower temperatures induce vacancy migration along the grain boundaries which is known as Coble creep [87]. Another mechanism can be found in the grain boundary sliding. This typically occurs when the creep exponent is in the range of 2 and 3 [85]. Fine grained material enhances the possibility for sliding of grains against each other and thus promotes this kind of creep deformation. A creep exponent located between 3 and 8 indicates a mainly dislocation controlled creep behavior, which is characterized by diffusion controlled climbing of edge dislocations to overcome obstacles for dislocation movement due to the presence of high vacancy concentrations, especially at high temperatures [85]. The activation energy Q of the creep performance can be determined with the help of the graphical representation of $log\dot{\varepsilon}_{II} = f\left(\frac{1}{T}\right)$, as shown in [88].

$$Q = \frac{\Delta log\dot{\varepsilon}_{II}}{\Delta\frac{1}{T}}R \tag{2.3}$$

In general, V-based alloys possess a good creep resistance in comparison to comparable materials like Ni/Co superalloys [15]. However, V-Si-B materials out of various manufacturing

processes exhibit noticeable differences regarding their creep performance due to the process-related microstructural evolution. This can be seen by different creep rates as well as different creep exponents. In Figure 2.9 it is shown that the minimum or secondary creep rate of a PM V9Si-13B and an IM V-9Si-13B alloy differs by one order of magnitude [15]. In terms of creep resistance, the very fine microstructure, evolving from PM processing, has a negative influence on the creep rate, since the high amount of grain boundaries leads to suffering from increased grain boundary sliding. Grain coarsening of PM alloys by means of high temperature annealing can significantly improve the creep response [15]. However, next to the grain size the creep response of the V-Si-B material is as well significantly influenced by the distribution and amount of the silicide phases, since they offer an enhanced creep resistance in comparison to the V_{ss} phase.

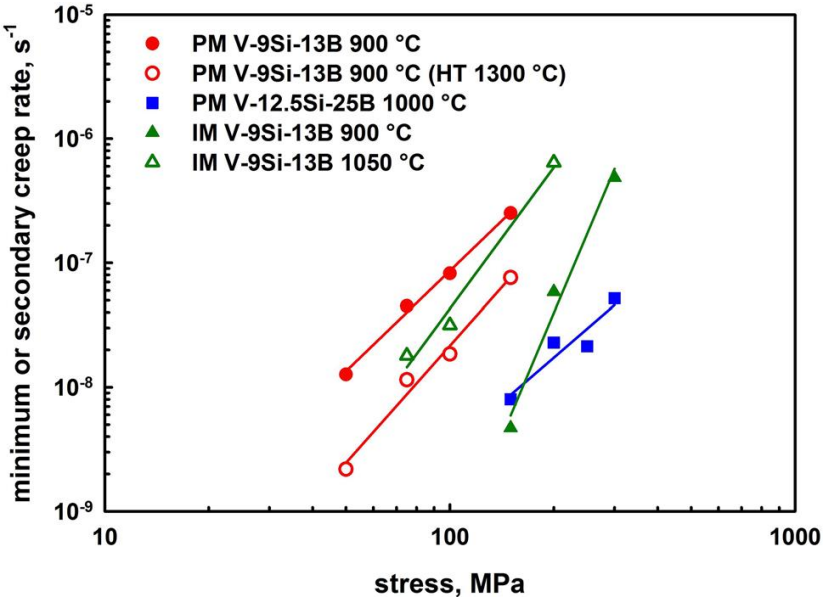

Figure 2.9: Illustration from [15] showing the creep response of the novel V-Si-B materials: Norton-plot of PM and IM V-Si-B materials at different temperatures.

Oxidation behavior of V-Si-B alloys

The application of V-based alloys at elevated temperatures (> 600 °C) under atmospheric conditions presents a fundamental problem. It is known that pure vanadium forms oxides, such as VO_2, V_2O, V_2O_5, in contact with pure O_2 or air environment. While VO_2 and V_2O exhibit melting points of 1970 ° and 1789 °C, the V_2O_5 phase starts melting at a temperature of 690 °C and thus, significantly affects the oxidation behavior of the V-based alloys at the foreseen elevated application temperatures (> 700 °C). Investigations of Natesan and Uz [89] show a dependency of the oxide formation on the O_2 partial pressure of the surrounding atmosphere. VO_2 was found to be the predominant oxide in specimens exposed to low oxygen environments; the oxide scales are continuous and tenacious. V_2O_5 was observed as the predominant phase in specimens oxidized in air and 100% O_2 environments [89]. By reaching temperatures above 690 °C, liquid V_2O_5 starts to drip off of the samples and as a result no protection or only little protection against the intrusion of oxygen to the metal/oxide interface can be observed [90]. Under atmospheric conditions, all structural applications of vanadium above 600 °C are thus excluded [91]. Investigations on the

low alloyed solid solution V-4Cr-4Ti alloy show that a slight increase of the concentration of the alloying elements (up to V-5Cr-5Ti) enhances the oxidation resistance at 600 °C, as it is depicted in Figure 2.10 a) [89]. Klicker and Bomberger [92] reported about a promising oxidation behavior with respect to the weight losses of a V-5Ti-20Al-10Cr-5Zr and V-20Ti-5Al-5Cr-20Zr alloy at 760 °C but liquid-oxide formation could not be suppressed completely. Alloy compositions with significantly increased Al and Cr/Ti concentration up to 30 at.% Al and 10 at.% Cr/Ti, investigated by Keller and Douglass [90], exhibit the most effective improvement in oxidation resistance in the temperature range of 700 °C and 1000 °C (see Figure 2.10 b)). The high Al concentration increases the viscosity of the liquid V_2O_5 layer which results in a delayed oxidation event. However, the dripping off of the liquid V_2O_5 phase only slowed down but could not be prevented. A further approach to enhance the oxidation resistance was observed by alloying V with Si and B [11][40], especially if the concentration of the alloying elements is high enough to enable the formation of intermetallic phases, such as V_3Si, V_5SiB_2, V_5Si_3 or V_3B_2. The intermetallic phases provide due to their superstructure, characterized by particularly strong bonds (predominantly metallic and covalent bonds) between the dissimilar atoms, an excellent oxidation behavior as well as outstanding high temperature strength and creep resistance. Second phase strengthening, due to the presence of intermetallic phases, plays an important role in enhancing high temperature properties of V-based alloys and represents a well-known strategy that has proven for a related Mo-Si-B system [93]. For the purpose of strengthening as well as for improvement of the oxidation resistance, the concentration and distribution of the intermetallic phases are decisive. Regarding the oxidation resistance, the silicide phases serve as Si reservoir which is released on contact with oxygen to form a protective SiO_2 layer. The presence of B in SiO_2 diminishes the viscosity at elevated temperatures and oxidizing environments [48]. Despite the positive influence of alloying with Si and B, the formation of V_2O_5 in the initial stages of oxidation deteriorated the oxidation resistance. Investigations of Williams and Akinc [40] attributed the V_2O_5 a faster grow rate in comparison to the protective SiO_2 layer, especially at Si depleted interface regions or pores and cracks, where the partial pressure of oxygen makes V oxidation favorable. Coating of V-Si-B materials represents an alternative solution to overcome this problem. The coating barrier prevents the diffusion of oxygen to the substrate surface. So far, only a few approaches have been mentioned in the literature. In [94] the coating of pure vanadium with layers based on Al_2O_3, CrO_3, NiO, TiO_2, Y_2O_3 and ZrO_2 was tested, but no long-term protective effect could be shown. Mathieu et al. [95] investigated multi-layered V_xSi_y silicides with an outer layer of VSi_2 as diffusion coating for V-4Cr-4Ti alloys. A protective effect of the coating layer in comparison to uncoated V-4Cr-4Ti was shown for isothermal oxidation up to 50 h at 650 °C. However, after 1500 h of cyclic oxidation (650 °C) V_2O_5 was detected on the surface of the coating layer [95]. Latest research activities of Hasemann et al. [96] made use of pack-cementation experiments to form a protective coating layer on V as well as a V-9Si-5B alloy. A two-step procedure involving the deposition of a Mo coating on the substrate that is followed by a pack cementation co-deposition of Si and B was carried out. Subsequent conditioning at temperatures between 1100 °C and 1300 °C enabled the formation of a multiphase multilayer coating with a protective borosilicate top layer. However, a successful coating application on V and V-based material was shown in [96] but oxidation experiments have

not been conducted yet. According to the state-of-the-art, there are no permanently technically usable coating concepts for V-Si-B alloys available yet.

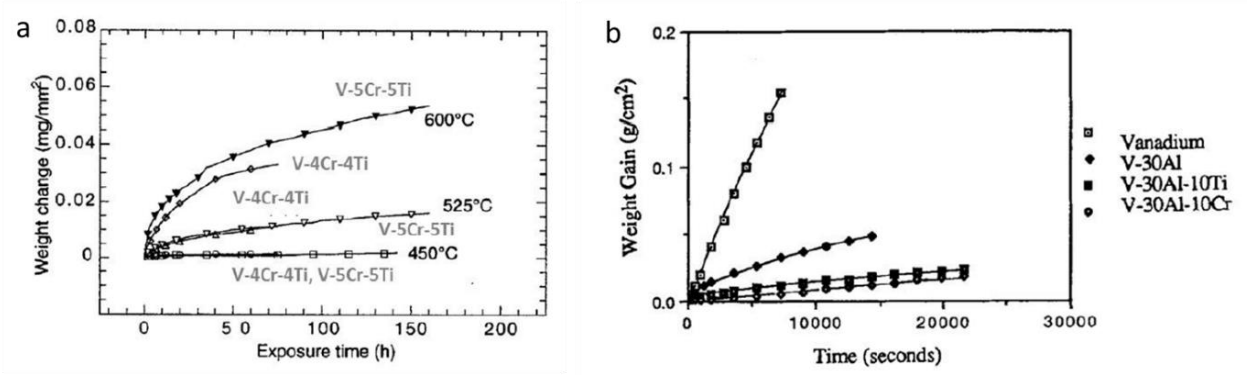

Figure 2.10: Oxidation behavior of a) V-4/5Cr-4/5Ti alloys [89] and b) V-based alloy compositions with increased Al and Cr/Ti concentration [90].

3 Materials and methods

3.1 Powder material

3.1.1 Mechanical alloying (MA)

For the production of alloyed powder material mechanical alloying (MA) was used. MA is a solid-state powder processing technique involving repeated cold welding and fracturing of powder particles in a high-energy ball mill [97]. For fundamental experiments both V–Si powder mixtures with Si concentrations of 2 at.%, 4 at.%, 15 at.% and 25 at.% and a ternary V-9Si-5B alloy (at.%), respectively, were prepared using pure V (purity: > 99.9%), Si (purity: 99.9%) and B powders (purity: 94 - 96%). In order to protect the highly reactive powders from contamination that can be caused by components of the ambient air (O_2 and N_2), the processing of the powder is always carried out under an inert Ar atmosphere in a glove box from M. Braun Inertgas-Systeme GmbH (O_2 content < 0.5 ppm). The weighed powder mixture (30 g) was filled into a vial (250 ml) together with the grinding balls (d = 10 mm) for a powder-to-ball ratio of 1:14. The vial was tightly closed in order to ensure MA under protective Ar gas atmosphere and subsequently fixed within the planetary ball mill (Retsch PM 400, speed ratio 1:-2.5, Figure 3.1). MA experiments were carried out at room temperature using vials and grinding balls made of steel at a rotational speed of 200 rpm. Table 3.1 provides an overview of the conducted MA experiments. Samples for analyses were taken by interrupting the milling process at defined periods of time (see Table 3.1).

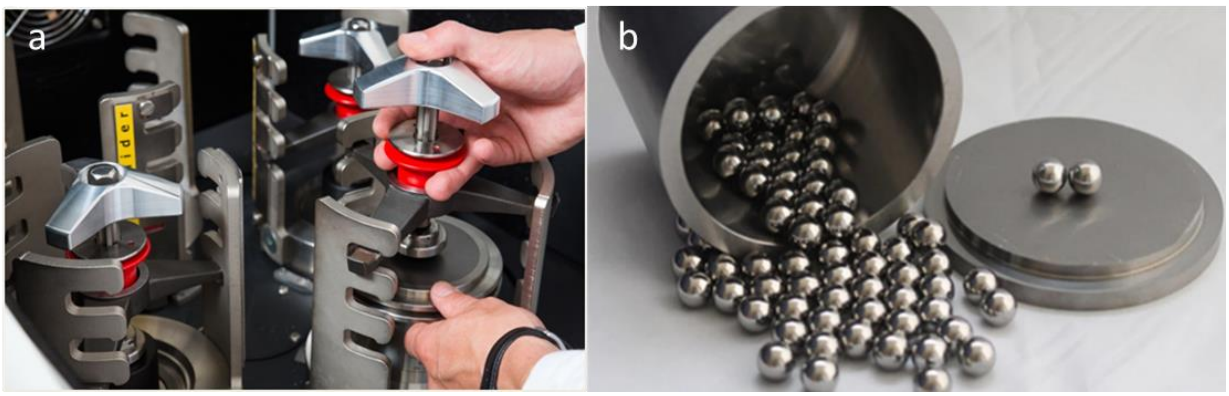

Figure 3.1: Planetary ball mill a) Fixing the vials on the sun disc (IWF, Otto-von-Guericke-University Magdeburg) and b) vial filled with grinding balls.

For all mechanically alloyed V-Si alloys with Si concentrations of 2 at. %, 4 at. %, 15 at. % and 25 at. %, a heat treatment under protective Ar atmosphere, covering a temperature regime of 1000 °C, 1100 °C, 1300 °C, and 1400 °C for a dwell time of 1 h (heating rate 3 K/min), was conducted in order to induce phase transformations. The mechanically alloyed V-9Si-5B alloy was thermally treated (under Ar atmosphere) at 1400 °C for 1 h dwell time (heating ramp 3 K/min).

Powder material for consolidation via FAST or DED (V-15Si, V-25Si, V-9Si-5B) was mechanically alloyed without interrupting for a duration of 25 h with the above mentioned parameters.

Table 3.1: Overview of MA experiments for powder characterization

Nominal alloy composition in at.%	Milling conditions	Milling time
V-2Si	Grinding tool: steel powder-to-ball ratio: 1:14 rotational speed: 200 rpm	1, 2, 5, 10, 20, 50, 100 h
V-4Si		1, 2, 5, 10, 20, 50, 100 h
V-15Si		1, 2, 5, 10, 20, 50, 100 h
V-25Si		1, 2, 5, 10, 20, 50, 100 h
V-9Si-5B		1, 2, 5, 10, 20, 50 h

3.1.2 Gas atomization (GA)

Gas atomization (GA) is a common method for metal powder production. A liquid metal column is passed through a nozzle at high pressure and then caused to explode by an inert gas jet such as argon or nitrogen forming a spray of micro-droplets that solidifies to powder particles. Powder production with designed properties gain more and more attention since currently a special focus lies on the use in additive manufacturing (AM). Powder material produced by gas atomization usually offers a spherical particle shape, benefitting flow properties, which are fundamental for application in AM processes. Due to very high cooling rates during the solidification of the particles, there is a very fine-grained and homogeneous microstructure after the solidification, however, the phase components possibly can be found far from thermodynamic equilibrium [6].

The gas atomization of the raw material was carried out by the company Nanoval GmbH & Co. KG. Therefore, the raw materials (V > 99.9%, Si > 99.6 % and B > 99.4 %) are stacked into a crucible with bottom pouring system, the outlet closed by a stopper rod. No pre-alloy was used. By means of an inductive heating system the metals are molten and superheated. Having reached the intended temperature melt flow as well as argon flow are released, melt and gas together pass a converging/diverging nozzle (Laval nozzle), where the melt stream is atomized into droplets/powder. After a cooling period the powder was classified with conventional sieves and an air classifier for the target fraction +15/-45 μm or +45/-90 μm.

3.2 Manufacturing of compacts

3.2.1 Field assisted sintering technology (FAST)

The Field Assisted Sintering Technology (FAST) has proven to be a promising powder consolidation technique capable for producing highly dense materials with a significant potential for grain size retention [98]. FAST is a pressure-driven consolidation by means of a pulsed direct electric current that passes through the sample compressed in a graphite matrix [99]. This direct way of heating allows the application of very high heating and cooling rates and thus leads to lower sintering temperatures and shorter sintering times in comparison to conventional sintering methods. A basic distinction can be made between solid-phase sintering and liquid-phase sintering. During solid phase sintering, the melting temperature of all phases involved is not exceeded, which means that the heat activated mass transfer processes are only controlled by diffusion processes. For liquid phase sintering at least one liquid phase needs to be present. However, the success of the sintering process can be seen in the large amount of free energy of the disperse powder bulk which arises due to [100], [101]:

I. excess free surface energy present in the system, especially of fine particles
II. the presence of imperfections in the crystal structure which are formed as a result of non-equilibrium conditions prevailing in the production of the powder material.

The fundamental driving force for the process is the reduction of the internal interface (grain boundaries) or surface (matter/atmosphere interface) energy and can be described as

$$\Delta(\gamma A) = (\Delta\gamma)A + \gamma(\Delta A) \tag{3.1}$$

where γ is the interface energy density and A is the interface area.

For single-phase systems, specific ways to minimize energy differences are given by reducing the outer (pore walls accessible from the outside) and inner surfaces (grain boundaries, walls of enclosed pores) as well as by reducing structural defects, in particular by minimizing surface defects due to atomic level mechanisms. For multi-phase systems (heterogeneous powder material) with a required solubility of the components, in addition to the points mentioned above, the prevailing state of imbalance needs to be repealed [72]. Diffusion processes, driven by the striving for a balance of concentration, play an important role here. Depending on the type and condition of the system, different material transport mechanisms can be taken into account. On the microstructural scale, sinter bonding is characterized by cohesive necks which grow between the contacting particles by converting the particle contact surfaces into high angle grain boundaries. On the atomic level growth of neck connections is a result of mass transport events by surface, volume and grain boundary diffusion, evaporation and condensation as well as plastic flow (dislocation motion under applied pressure causing flow of material) [102].

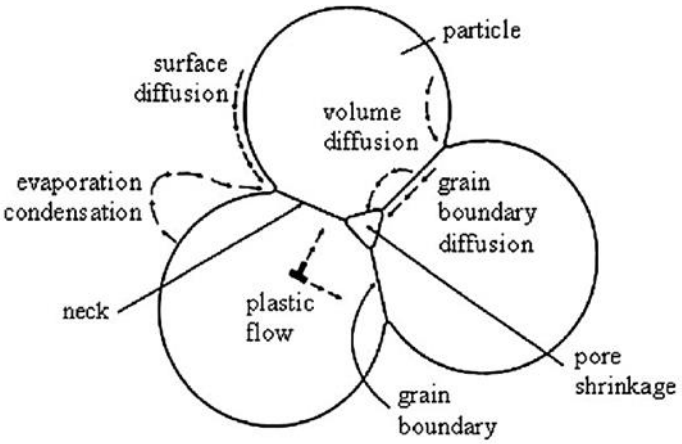

Figure 3.2: Various mass transport paths during sintering [102].

Figure 3.2 illustrates the mass transport paths of diffusion, plastic flow as well as evaporation and condensation processes during solid-state sintering. In general, diffusion is the movement of atoms, ions and molecules and occurs in systems with different concentration gradients due to the Kirkendall effect as inter lattice movement or movement via vacancies. A certain amount of energy has to be applied for the mass transport to occur. This activation energy is taken from the thermal energy of the mass particles/matter or the lattice and can be explained on the basis of Fick´s laws of diffusion [24]:

$$\overrightarrow{J_D} = -D\frac{\delta x}{\delta r} - D\vec{\nabla}x \tag{3.2}$$

$$\frac{\delta x}{\delta r}\vec{\nabla}\left(D\vec{\nabla}x\right). \tag{3.3}$$

Fick's first law (3.2) describes the proportionality between the diffusion current j_D (number of mass particles passing a unit area per unit of time) and the local concentration gradient $\frac{\delta x}{\delta r}$. The diffusion coefficient D depends on the temperature, the diffusing component, the crystal structure, and defcts. Fick's second law (3.3) represents the change of concentration as a function of location and time, and states that the differences in mass flow in a volume element has to match the change of concentration. There is no change of the total number of the mass particles [24], [103]. Furthermore, a distinction between densifying and non-densifying mechanisms can be made. From Figure 3.2 it can be noticed that the densification happens only if atoms move along the boundaries creating a continuous mass flow into the pores which leads to a macroscopic shrinkage of the sintering bodies. Grain boundary diffusion and volume diffusion leads to movement of atoms to the surface of the pores resulting in elimination of porosity and an increase of the density. Hence, they are designated as densification mechanisms[102]. In contrast, surface diffusion, volume diffusion from surface and evaporation-condensation occur without densification due to the rearrangement of the atoms on another surface or part of the same surface, i.e. they rearrange the matter inside of pore volumes and do not cause pores to shrink. Therefore,

they are considered as non-densifying mechanisms. The sintering process is divided into three stages, which are described in Table 3.2.

Table 3.2: Stages of the sintering process [102], [104].

Initial stage	Intermediate stage	Final stage
	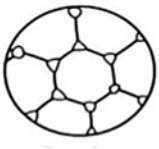	
Formation of sinter necks -loose particles and pores rearrange their positions into more preferable packing arrangements -formation of new contacts -sinter necks form at the contact areas and begin to grow due to diffusion processes -increase of density: 60-65%	**Densification and pore size reduction** -pores form interconnected cylindrical channels locate along the grain boundaries -reduction of cross section of pores leads to densification. -pores become unstable and separate from each other -increase of density: 65-90%	**Final densification** -isolated pores are located at the grain corners -growth of larger grains in addition to the consumption of smaller grains -pore diameters reduce gradually until final closure -densification from the isolated pore state to final densification -increase of density: 95-99%

The sintering process for the V-Si-B powder material, was carried out by the Karlsruhe Institute of Technology (KIT), Karlsruhe, Germany.

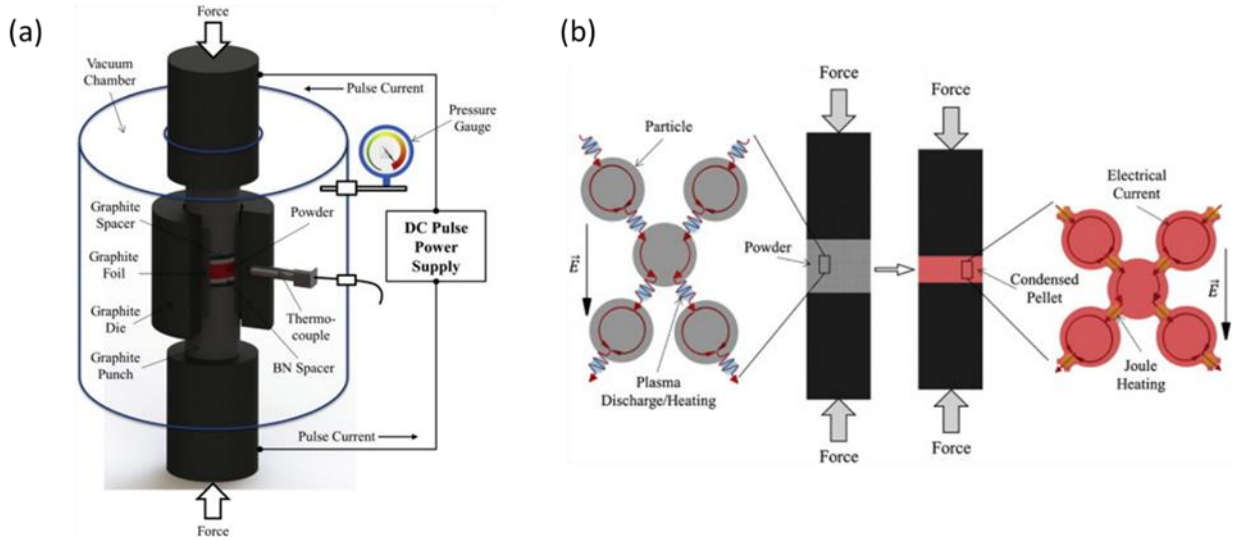

Figure 3.3: Experimental setup for field assisted sintering technology (FAST) at the Karlsruhe Institute of technology (KIT), Karlsruhe, Germany a) structure of the manufacturing plant b) sintering mechanisms of powdery materials [98].

Figure 3.3 shows the experimental setup used in the present work. The mechanically alloyed powder material was filled into a graphite die and the punch unit was heated by means of a direct current (DC) via Joule effect (Figure 3.3 b)). The pulsed electric current causes a partial heating and the formation of an electric field at the grain boundaries of the powder particles and leads to densification over sinter neck growth resulting in fusion of the particles [105], [106]. The quasi-static compressive stress, applied in FAST, leads to better contact between the single particles, changes the amount and morphology of those contacts, enhances the existing densification mechanisms already present in free sintering (grain boundary diffusion, lattice diffusion and viscous flow) or activates new mechanisms, such as plastic deformation or grain boundary sliding [74].

V-Si and V-Si-B compacts were manufactured via FAST by using a heating rate of 100 K/min and holding times of 15 min at 1100 °C and 1400 °C. The whole process was performed under mild vacuum (P < 10Pa) and uniaxial pressure of 50 MPa. Samples for examination by scanning electron microscopy (SEM) and thermomechanical investigations were prepared from the sintered buttons (diameter 20 mm and 30 mm, height each 9 mm). A part of these samples were thermally treated at 1400 °C for 10 h in order to achieve grain coarsening which is supposed to be beneficial in terms of creep resistance.

3.2.2 Laser - Direct energy deposition (L-DED)

Laser - Direct energy deposition (L-DED) is a generative manufacturing process for metals and alloys. A focused energy source (Laser) generates a melt pool on the surface of the substrate material or component into which the metal powder is injected through a nozzle. Beads are welded together, which create structures on existing basic bodies or entire components. The manufacturing via DED of the V-Si(-B) alloys was conducted by the Fraunhofer – Institute for Laser Technology (ILT), Aachen, Germany.

L-DED is achieved through the supply of a continuous material feedstock being fed into the laser focal area on the substrate where the material (powder or wire) is melted and forms a melt-pool which becomes solidified [20]. To minimize potential oxidation events, the powder material is injected (by a coaxial nozzle) under protective shielding gas. Shielding/carrier gas also enhances the deposition efficiency but material losses due to a possible overspray need to be taken into account as well [107]. By means of L-DED processing there is a possibility to create a new part on existing parts with strong metallurgical integrity for part modification, repair or remanufacturing processes which is one of the advantages that DED has over other AM technologies and any conventional manufacturing process [108]. Another advantage can be seen in the flexibility of using more than one material simultaneously, which enables the ability of manufacturing functionally graded parts. In general, there are five basic steps (shown in Figure 3.4) which are involved in the AM/DED process.

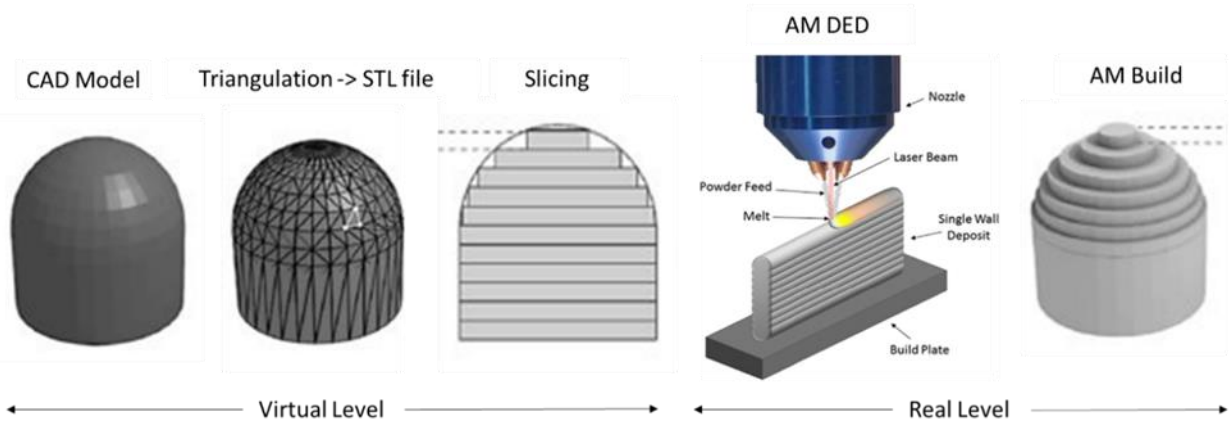

Figure 3.4: Development of AM objects [107], [109].

Microstructural evolution during L-DED processing strongly depends on the solidification process. The melt pool starts to solidify directly when the laser moves away from the melt pool region. Factors influencing the solidification can be seen in the processing parameters as well as in the initial temperature of the substrate before the laser is applied. A large melt pool, induced by a prolonged material interaction due to a high laser power and a slow scanning speed, results in a low solidification rate which causes melting or re-melting of the substrate material or the preceding layer. In contrast a high scanning speed causes a low laser-material interaction and the melt pool solidifies rapidly. The same effect can be achieved if the substrate material (or preceding layer) has a low initial temperature as this causes a heat sink [20].

Solidification during L-DED processing starts from the interface between the melt pool and the substrate or preceding layer (solid-liquid interface region) which is the nucleation site for the crystal grain growth [110]. The crystal growth follows a crystallographic orientation with respect to the substrate crystal or the preceding layer crystal (epitaxial grain growth). With continuing solidification process grain growth continues in perpendicular direction to the substrate and in the opposite direction to the direction of the heat flow and a characteristic columnar structure, that is typically observed in L-DED processes, arises [111]. Figure 3.5 shows a schematic illustration for the formation of a columnar fine near-equiaxed structure with traversing heat affected zones of a titanium alloy as a general example of a L-DED microstructure. The microstructure of the heat affected zones, arising due to the layer-by-layer laser melting, is characterized by more globular grains which occurs due to the re-melting effect that is happening in the overlapping region in both the tracks and the layers. These grains, very close to the melt pool region, gain enough heat to induce grain growth which finally leads to the globular microstructure. This phenomenon is depicted in the schematic illustration in Figure 3.5, where coarser globular grains can be found along the fusion line (overlapping region). In contrast, the grain size is reduced if the position is further away from the melt pool region. Regarding the entire build, the produced microstructure will keep changing as layers are added which can lead to the development of complex, heterogeneous, and anisotropic microstructures. Thus processing parameters are an essential key to achieve a desired microstructure and hence desired mechanical properties. Strong influence is given by the scanning velocity, the solidification rate as well as the

cooling rate. High scanning velocities lead to high solidification rates resulting in a columnar, equiaxed grain growth. A more equilibrium microstructure arises with a lower solidification rate. Next to this, high cooling rates promote the formation of a fine grained microstructure. However, important points for the formation of DED microstructures are both the processing parameters and the influence of the complex thermal history of the several layers [20].

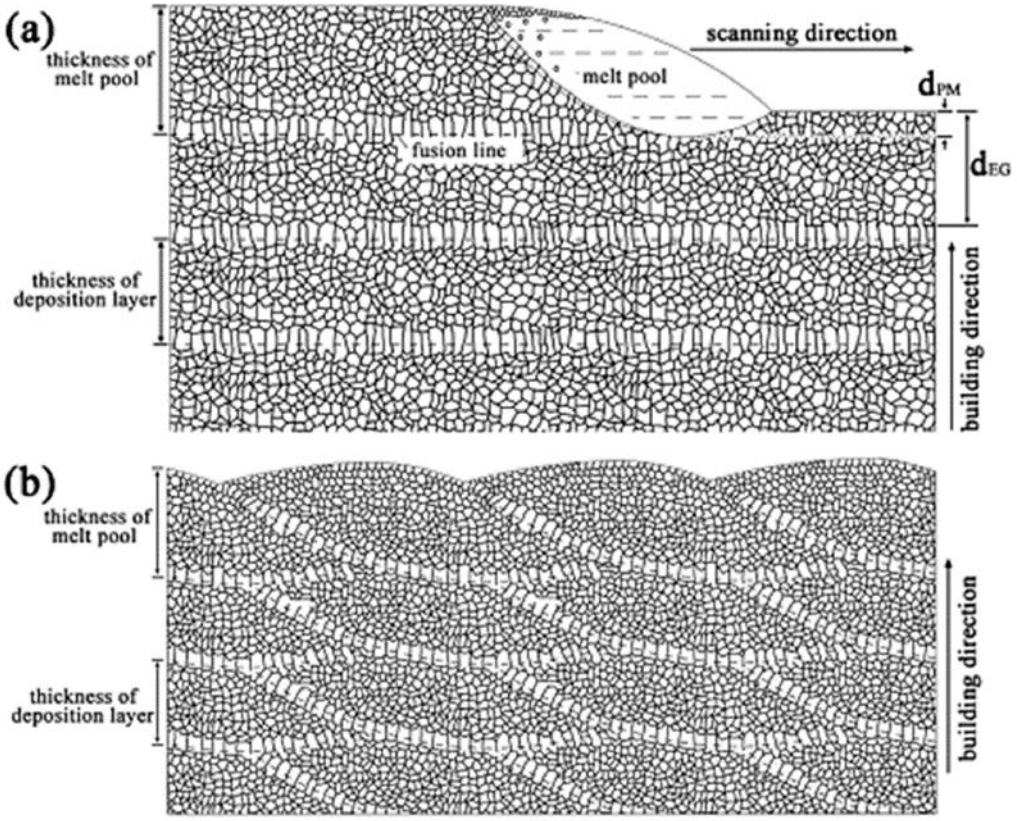

Figure 3.5: Schematic illustration for the formation of fine near-equiaxed grains for titanium alloy components during the layer-by-layer laser melting in a) longitudinal and b) transverse cross sections [112].

A sketch of the general setup for the L-DED experiments is depicted in Figure 3.6. For processing a 2 kW diode laser and a continuous coaxial powder nozzle were used. The experiments were carried out in an inert gas chamber providing an oxygen content below 50 ppm. As carrier gas, for the protective inert gas stream of 15 l/min and global shielding, argon 4.6 was used.

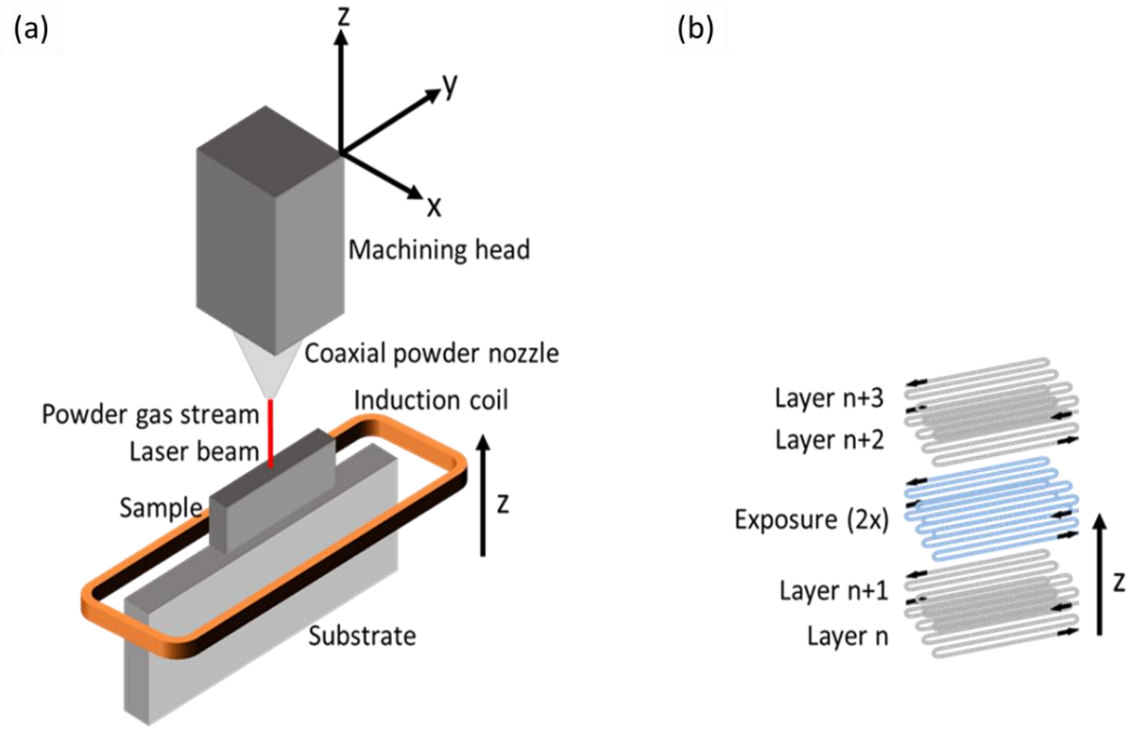

Figure 3.6: a) Sketch of the setup and b) final scanning strategy.

The substrate material was preheated to approx. 710 °C. The setup includes a freely movable induction coil in the "z" built direction which ensures a constant preheating temperature in the respective processing plane. As scanning strategy an alternating bidirectional strategy with double exposure without powder feed subsequent to the built of every second layer (Figure 3.6 b)) was used. This strategy improved the surface smoothness due to the re-melting and thus stabilized the structure of the subsequent layer. The used L-DED parameter are presented in Table 3.3. The height of each layer was 0.2 mm and DED samples of 4 x 5 x 10 mm³ in size were built. A Ni-base superalloy, namely Monel® Alloy 400 with the nominal composition $NiCr_{33}Fe_{2,}$ was chosen as substrate material.

Table 3.3: L-DED parameters used in this work.

Parameter	Symbol	Unit	Value build-up	Value re-melting
Laser beam power	P_L	W	175	120
Laser beam diameter	D	mm	0.6	
Scanning velocity	v_v	mm/s	6.67	
Overlap	Δy_s	mm	0.3	-
Powder mass flow	V_P	cm³/min	0.56	-

Both the compacts manufactured via FAST and the compact manufactured via L-DED was thermally treated at 1400 °C under Ar atmosphere for a 10 h dwell time using a heating rate of 3 K/min.

3.3 Analytical methods

3.3.1 Powder characterization

In order to characterize the materials behavior during the MA process as well as before consolidation, where the powder material also emerges from a gas atomization process, detailed investigation of the powder particles is necessary. The properties of the applied raw materials substantially influence the processability as well as the material properties obtained in the products. Hence, detailed investigations provide a fundamental understanding of the influence of powder characteristics on component integrity for different powder metallurgical processing routes. Depending on the intended use, the following analytical methods were used to characterize the powder material.

The particle size distribution of the powder material was determined via laser diffraction analysis in a wet dispersed state using a Malvern Mastersizer 2000. In addition, the sphericity of the powder was investigated using the imaging Morphologi G3 module. A decisive value for the characterization of powder materials is the oxygen concentration, which varies significantly due to the manufacturing process. The oxygen impurity concentration of the present powder material was determined by means of hot gas extraction technique using a Bruker ON/H-mat 286 analyzer which is designed to handle compact samples. Therefore, the powder samples had to be filled into Ni capsules (each with 25 mg powder) under protective argon atmosphere. The samples were measured under helium atmosphere for 45 s to 60 s. For processing via AM the powder flow is a compelling characteristic because uniform build rates leads to less porosity of the AM compacts [17], [113]. The flowability of a bulk solid is characterized by its unconfined yield strength σ_c, in dependence on consolidation stress σ_1, and storage period t. Usually the ratio ff_c of consolidation stress σ_1, to unconfined yield strength, σ_c, is used to characterize flowability numerically [114]:

$$ff_c = \frac{\sigma_1}{\sigma_c} \tag{3.4}$$

The larger the ff_c value is, i.e., the smaller the ratio of the unconfined yield strength, σ_c, to the consolidation stress, σ_1, the better a bulk solid flows [114].To determine the flowability of the powder particles a standardized ring shear test was conducted [115].

3.3.2 Inductively coupled plasma optical emission spectroscopy (ICP-OES)

Inductively coupled plasma (ICP), is one method of optical emission spectrometry (OES). Atoms of component elements are excited by plasma energy generated via ionized argon gas. When the excited atoms return to low energy positions, photons are released and their

wavelengths are measured [116]. While the element type is obtained by the energy position of the photons, the content of each element is determined based on the photons intensity. For measurement the powder material as well as the solid sample material is completely dissolved by digestion and is then introduced into the inductively coupled argon plasma using a pneumatic atomizer system. As a result, elements are excited to emit light that is rated according to its specific wavelength and intensity. ICP-OES measurements were provided by the Forschungszentrum Jülich, Germany. For digestion of the samples 3 mL HNO_3, 3 mL HCl, 2 mL HF were used.

3.3.3 Metallographic preparation

The microstructural analysis of sample material is an important parameter for understanding the material behavior. For investigation different preparation techniques and analytical methods can be used. Most of them involve metallographic preparation steps such as mounting the samples into a cold or hot, conductive or non-conductive resin. The choice of resin depends on the type of sample and the purpose of study. After embedding, grinding, and polishing steps follow and in some cases etching. Fast and easy microstructural investigations can be carried out by optical microscopy offering a maximum of 2000 times magnification and a limit of 1 µm resolution. A higher resolution range, to investigate the microstructure down to nanometer scale, can be obtained by using scanning electron microscopy (SEM) or transmission electron microscopy (TEM).

To investigate the microstructure and to achieve properly sized samples material for mechanical testing and oxidation tests, bulk material was cut via electrical discharge machining (EDM). All samples, the powder material as well as the compacts, were embedded in a hot mounting polymer (Struers PolyFast). Subsequently they were ground using SiC grinding paper with a grit of 500, 800, 1200, and polished with a 3 µm and 1 µm diamond suspension. For compact samples a colloidal silicia suspension (OPS with NH_3 and H_2O_2 additions) was additionally used for polishing.

3.3.4 X-ray diffraction analysis (XRD)

The XRD analysis is based on the diffraction of monochromatic X-rays at the planes of crystalline materials. The interaction of the incident rays with the sample produces constructive interference (and a diffracted ray) when conditions satisfy Bragg's Law [117].

$$sin\theta = \frac{\lambda}{2d_{hkl}} \tag{3.5}$$

θ is half the angle between the diffracted beam and the original beam, λ is the wave length of the X-rays and d_{hkl} is the interplanar spacing between the planes that caused constructive interference of the beam. In this work XRD measurements were conducted using an X'Pert X-ray diffractometer (PANalytical) with Bragg-Brentano geometry and Co-$K_{\alpha 1,2}$ radiation (α_1 = 1.789 Å and α_2 = 1.793 Å). Measurements were performed on powder material using backloading

preparation. All measurements were taken in the scanning range of 20° - 140°and a measurement time of 500 s per step. The phase identification was obtained using the software X´Pert High Score Plus (by PANalytical).

3.3.5 Scanning electron microscopy (SEM)

The scanning electron microscope (SEM) permits the observation and characterization of heterogeneous organic and inorganic materials on a nanometer (nm) to micrometer (μm) scale [118]. The area to be examined is irradiated with a finely focused electron beam, which is swept in a raster across the surface of the specimen to form images or to obtain an analysis at one position [118]. The types of signals produced from the interaction of the electron beam with the sample include secondary electrons, backscattered electrons, characteristic x-rays, and other photons of various energies. These signals are obtained from specific emission volumes within the sample and can be used to examine characteristics such as surface topography, crystallography, composition, etc [118]. The secondary and backscattered electrons are the most important signals for imaging. In the secondary electron (SE) contrast the electrons are emitted from a very thin surface layer, providing a high signal-to-noise ratio beneficial for imaging surface topologies [119]. The backscattered electrons (BSE), which reveal with higher energies in comparison to the SE ($E_{BSE} \sim E_{primary}$, $E_{SE} < 200eV$), enable imaging of composition contrasts, since various BSE intensities are emitted due to the different atomic numbers of the elements/phases [119]. The interaction of the electron beam with the sample also provides the emission of characteristic X-ray radiation. The analysis of the characteristic X-ray radiation emitted, namely energy dispersive X-ray spectroscopy (EDS), can yield both qualitative identification and quantitative elemental information (except e.g. B, C, N and O) of the specimen [118]. Targeted phase identification can be implemented using electron backscatter diffraction (EBSD). This method is based on inelastic scattering of electrons hitting the lattice planes at the Bragg´s angle. The backscattered electrons describe Kikuchi patterns which provide information about the crystal structure, orientation, and stress. Automated indexing of patterns and computer-automated crystal lattice orientation mapping allow this technique to identify phases, qualitatively as well as quantitatively, and show misorientation across grain boundaries, respectively [118]. A combination of EDS and EBSD is a useful tool for explicit phase identification by utilizing both, chemical and crystallographic information.

The microstructural observations in this work were carried out by using a SEM (SEM – FEI ESEM XL30 FEG) equipped with EDS. In order to investigate the multi-phase microstructures of V-Si(-B) alloys BSE mode (acceleration voltage $10 - 25$ keV) was typically applied for a composition contrast differentiation of the individual phases. The morphology of the V-Si(-B) powder particles, however, was examined in SE mode. EBSD analysis of the V-Si(-B) powder material and compacts was performed to identify phase distribution using a Zeiss Merlin SEM with Nordlys EBSD camera and Aztec software package (Oxford Instruments) provided by the Forschungszentrum Jülich. Further EBSD analysis were carried out at the Institute of Materials and Joining Technology (Otto-von-Guericke-University Magdeburg, Germany) by using of

DualBeam FEI Scios. The scan size of 88.5 x 86.5 µm² was investigated with a step size of 0.3 µm. Inverse pole figure (IPF) color coding as well as grey scale (by the way, rest in peace Karl Lagerfeld) with confidence index, was used.

3.3.6 Sample preparation for TEM using focused ion beam (FIB)

Focused ion beam (FIB) milling is a technique used for the preparation of electron transparent foils for transmission electron microscopy (TEM) investigations. A finely focused beam of Ga ions, operating at high beam currents, was used for this. Material is removed as the Ga ions hit the sample surface and a thin lamellae were milled out of the metallographic sample. Manufacturing of a lamella with the dimension of 10 x 5 µm² and a thickness of approx. 200 nm, to be electron transparent, was used in this work. The milling was carried out using a FEI Strata FIB. The lamella was post-processed using a precision ion polishing system (PIPS) to obtain high quality samples.

3.3.7 Scanning transmission electron microscopy (STEM)

STEM investigations were carried out at the Institute of Physics, Otto-von-Guericke-University Magdeburg, Germany using a FEI STEM Tecnai F20(FEG). STEM images were typically obtained as bright-field images using an acceleration voltage of 200 kV.

3.4 Mechanical testing

3.4.1 Microhardness testing

Hardness measuring of a material provides a quick and easy to implement option to get a first impression of the mechanical properties at room temperature. Microhardness measurement for embedded powder material (section 3.3.3) as well as for the compact specimens were carried out according to DIN EN ISO 6507 – 1 [120] by indenting a Vickers pyramid with a force of 1 N (HV 0.1) for a holding period of 5 s. The indents were performed by means of the automatic microhardness tester Wilson VH3300 (Buehler) equipped with the software DiaMet enabling direct evaluation of the hardness values. The Vickers hardness HV can be calculated using the projection left by the indenter, including consideration of the 136 ° angles, using the following equation:

$$HV = 0.102\frac{F_i}{A_{HV}} = 0.102\frac{2F_i sin\left(\frac{136\,^\circ}{2}\right)}{d_{HV}^2} \approx 0.1891\frac{F_i}{d_{HV}^2} \tag{3.6}$$

Where F_i is the indentation load and A_{HV} is the projected indent area, which is described by the pyramid`s diagonal d_{HV} [121].

3.4.2 Mechanical testing from RT up to 900 °C

Compression and Creep

For assessing the mechanical properties of the V-Si-B material mechanical testing was carried out. Uniaxial compression tests were conducted using a Zwick/Roell Z100 electromechanical testing machine equipped with a Maytec furnace. Specimens were cut via EDM to a geometry of 2mm x 2mm x 3.5 mm. Uniaxial compression tests were carried out using an initial strain rate of $1 \cdot 10^{-4} s^{-1}$ and constant displacement. Tests have been performed at RT as well as 600 °C and 900 °C using a protective flowing Ar/H_2 atmosphere.

Creep of materials is classically associated with time-dependent plasticity under a fixed stress at an elevated temperature, often greater than roughly 0.5 T_m, where T_m is the absolute melting temperature [122]. More detailed information can be found in Chapter 2.5. For determination of creep properties, the compact V-Si-B alloys were cut via EDM to dimensions of 2mm x 2mm x 3.5 mm. The creep tests were conducted using the Zwick/Roell Z100 electromechanical testing machine equipped with Maytec furnace under compressive mode. The experiments were performed under protective Ar/H_2 gas flow, to prevent the occurrence of oxidation processes, at a temperature of 900 °C by applying a constant true stress of 50 MPa, 100 MPa, 150 MPa and 200 MPa.

3.5 Cyclic oxidation experiments

Next to properties like high temperature strength and creep resistance the oxidation behavior of the material is an important criterion for application. The oxidation resistance of a material can be reliably examined using cyclic oxidation tests. Cyclic oxidation tests imitate real conditions of exposure and allows an assessment of the oxidation behavior and thus, an assessment of alloy life cycle.

The exposure time during the initial stage (< 1 h) covered 10 min and was subsequently raised to a 1 h cycle up to 8 h, followed by 24 h cycles up to 104 h and a 36 h cycle up the final exposure time of 140 h [89], [123]. The cyclic oxidation tests were performed by the Institut für Korrosions- und Schadensanalyse (IfKorr), Magdeburg, Germany. All tests were carried out under static air in a box furnace (ThermConcept KLS50/14) at 600 °C. Further tests were conducted at 900 °C. However, these were stopped after a few minutes due to failure of the sample by draining material. Before starting the exposure, a precise determination of the initial weight was carried out. The geometry of the samples used was 2 mm x 2 mm x 3.5 mm (rectangular specimen, cut via EDM). At the end of each cycle the samples were removed from the furnace, cooled down to room temperature under atmospheric conditions and carefully weight to determine their weight change after certain exposure times. The samples were then re-exposed to the particular temperature of the above described testing regime. The specific mass change was carefully measured by means of an analytical balance with an accuracy of 0.0001 g. In order to get a better understanding of the oxidation process, occurring microstructural changes or scale forming of the oxidized samples were studied via SEM. A Zeiss stereomicroscope was used to record the surface conditions

photographically. Macro-images were taken to visualize the sample quality/morphology after the oxidational exposure. The resulting weight change curves were plotted vs. the exposure time.

3.6 Density functional theory (DFT) simulation

In order to determine the Gibbs reaction and formation enthalpies of B_2O_3, SiO_2, V_{ss}, V_5SiB_2, V_3Si, V_2O_5 and V_3O_5, one needs the internal energy after structural relaxation as well as the vibrational and electronic Helmholtz energy. The structural relaxation was carried out with Quickstep [124] implemented in the CP2K version 5.1 program package [125]. The first-principles calculation for the structural relaxation using the Gaussian plane wave method (GPW) [126] were executed until a total energy self-consistency of 10^{-6} Ha and until the self-consistency for the forces and maximum geometry change of 10^{-5} Ha/Bohr and 10^{-5} Bohr, respectively were achieved. The energy cut-off for the plane waves on the grid were 1200 ryd and the k-mesh sampled via the Monkhorst-Pack algorithm [127] were 14x14x8, 12x12x12, 20x20x20, 12x12x6, 12x12x12, 16x6x12 and 6x12x8 for B_2O_3, SiO_2, V_{ss}, V_5SiB_2, V_3Si, V_2O_5 and V_3O_5 respectively. For V, Si and B the DZVP-MOLOPT-SR-GTH basis set [128] for the atomic centered Gaussian functions were chosen, while for the interatomic part the GTH-pseudopotentials were used [129]–[131]. Exchange and correlation in this density functional theory (DFT)-based method were treated with the PBE-GGA functional by Perdew, Burke and Ernzerhof [132].

To calculate the temperature dependent vibrational Helmholtz energy PHONOPY [133] with Quickstep as the calculator was used. For the PHONOPY calculations supercells of the solid state phases were created and the k-mesh changed to 4x4x4 for all supercell calculations in the energy and force determination. The electronic Helmholtz energy were calculated with the density-of-states of the solids as parameter which were carried out using the tight-binding, linear muffin-tin orbitals with the atomic spheres approximation (TB-LMTO-ASA) [134], [135] as implemented in the TB-LMTO 4.7 program [136]. Exchange and correlation were treated with the PW91-GGA functional by Perdew et al. [137]. The k-mesh was chosen to be 20x20x10, 18x18x16, 30x30x30, 16x16x16 19x19x19, 26x8x18 and 10x18x12 for B_2O_3, SiO_2, $V_{(ss)}$, V_5SiB_2, V_3Si, V_2O_5 and V_3O_5, respectively.

For the oxygen molecule in the reactions and formations, the internal energy of a single O_2 molecule was calculated with Quickstep in a large 10 Å x 11 Å x 12 Å simulation box with a Gamma centered k-mesh. The translational, rotational and vibrational energy at temperatures above 0 K were then calculated using the thermodynamics of the well-known ideal gas approximation.

4 Considerations on the ball milling process

The process of mechanical alloying (MA) is an important part of this work and is therefore explained in detail with respect to the mechanism and kinematics of the planetary ball mill at the beginning of the following chapter. In the course of this chapter (Section 4.2) numerical calculations as well as a numerical simulation of the energy input during milling will be presented. The purpose of this chapter is to present the impact events and the energy required for MA as more tangible quantities.

4.1 Theoretical description of the MA process

4.1.1 Mechanical alloying of metal powder

While elemental powder material can be manufactured via several processes (such as comminution, reduction, electrodeposition, etc.) pre-alloyed powder material requires processes like mechanical alloying (MA), gas atomization (GA) or surface modification [72]. MA proves to be an advantageous process for high temperature materials. The often very high melting temperatures of the alloying components are not process-relevant, since the alloying process is driven by high energetic impact during milling in a planetary ball mill [138]. The MA process was first introduced by Benjamin [139] in 1970, showing the manufacturing of an oxide dispersion strengthened alloy via solid-state route, independent of any ingot metallurgical procedure. Mechanical alloying, also known as high-energy ball milling, generates homogeneous materials in a solid state by milling at least two different powder materials (elemental or pre-alloyed powder) in a certain ratio under high energy input in a vial filled with milling balls [138]. While conventional ball mills only reduce the powder particle size, the possible high energy transfer in a planetary ball mill promotes fracturing as well as welding processes [97]. The aim of this process is to create a balance between both processes (comminution and cold welding) in order to obtain a homogenization of the powder material down to the atomic level. For an optimal alloying result, the following milling parameters must be taken into account according to the material to be alloyed and the desired target [140]:

- grinding tool (vial material, grinding ball material and size)
- process parameters (rotational speed, duration time, process temperature)
- ball-to-powder ratio, vial filling level
- additives and atmosphere (inert gas).

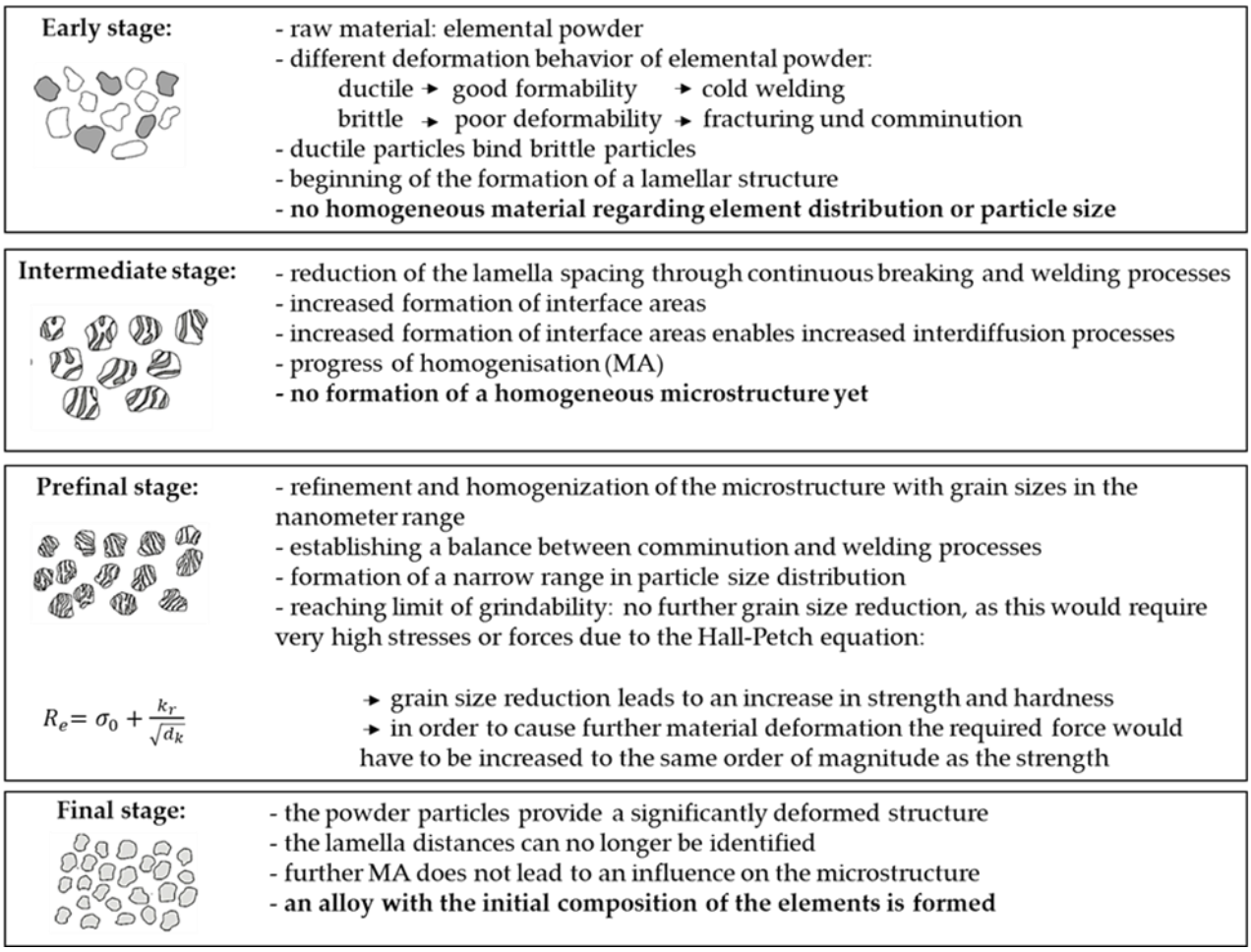

Figure 4.1: Powder modification and microstructural evolution during MA [72], [138], [140].

The modification of the powder material during MA driven by impact events of the grinding balls, the powder material and the vial wall as well as collisions between the powder particles themselves is shown in Figure 4.1. Depending on the properties of the individual alloy components as well as the grinding tools and process parameters, repeatedly flattening, cold welding, fracturing and re-welding of the particles occur during MA. During milling the high kinetic energy of the grinding balls is transferred to the powder particles in form of mechanical stresses. The impact energy causes a strong deformation of the powder particles, which leads to movement and pile up of dislocations and thus, to hardening of the particles. With exhausted deformation capacity fracturing of the particles occur and atomically pure surfaces are formed. This reactive surfaces promote welding processes in the subsequent collisions events [140]. In general, the MA process can be divided into four stages, which are described in Figure 4.1.

After MA particles exhibit a significant deformed but homogenized microstructure. The alloying elements are dissolved in the crystal lattice (host lattice) which occurs in form of a saturated or supersaturated solid solution. Mechanically-induced phase formation (e.g. intermetallic phases) is possible as well. The increase in strength, induced by the high energy

transfer during MA, results from the increased resistance to plastic deformation based on the dislocation movement. These dislocation movements in the crystal lattice can be restricted by various mechanisms or obstacles [85]. MA typically evokes hardening mechanisms, such as solid solution strengthening, grain refinement as well as work hardening.

Solid solution strengthening

Solid solution strengthening bases on elastic lattice distortions induced by alloying elements soluble in the crystal lattice. Lattice strain field interactions between dislocations and solute atoms lead to restrictions of dislocation movement. This increases the fundamentally present resistance against dislocation sliding, namely the Peierls-Nabarro stress, in a defect-free lattice [87]. The dissolved atoms can occupy interstitial sites (interstitial solid solution; form when the solute atom is small enough to fit at interstitial sites between the solvent atoms) as well as the position of the original host atoms by forming a substitutional solid solution. The factors controlling the tendency to form a substitutional solid solution are given by the Hume-Rothery rules [141]. In the case of V-Si-B: Si additions to V lead to the formation of a substitutional solid solution, since the difference of atomic radii is less than 15% and there is similar number of valence electrons (Si: 4 valence electrons, V: 5 valence electrons). For V-B the difference of atom radii exceeds the 15% and B will thus occupy interstitial positions. While substitutional solutes produce primarily volumetric changes, interstitial solutes (insertion of atoms into octahedral and tetrahedral positions) result in either volumetric and distortional (shear) strains [142]. Thus, the more efficient influence on strengthening is attributed to interstitial atoms.

However, formation of substitutional solid solutions dominate the V-Si-B alloy systems investigated in this work. When substitutional solid solutions are formed the nature and effect of the interaction with the dislocations depend on the concentration and size of the impurity atoms. Substitutional solutes generally stretch the lattice uniformly producing hydrostatic (spherical) strain fields around the solutes [142]. Figure 4.2 depicts the influence of size of the impurity atoms. While larger atoms cause local compression strain, smaller atoms burden the lattice with tensile stresses. Interaction between foreign atoms and dislocations caused by the size differences of the substitute and matrix atoms, are called size effect. Another interaction between dislocation and dissolved atoms occurs since the strength of bonding between the dissolved atom and its neighbor atoms differs from that of the pure crystal which leads to a change of the modulus of elasticity as well as the shear modulus in the vicinity of the impurity atom [85]. The elastic interactions, that arise due to the different elastic properties of the solute and matrix elements, are called modulus effect. If the shear modulus of the solute is smaller in comparison to the shear modulus of the solvent, the energy of the strain fields around the dislocations will be reduced which leads to an attraction between the solutes and the dislocations. Lattice misfit strains are proportional to the local change in lattice parameter per unit concentration of the solute [85]. Size and modulus effect are detailed described in some of Fleischer´s classic papers: [30], [143].

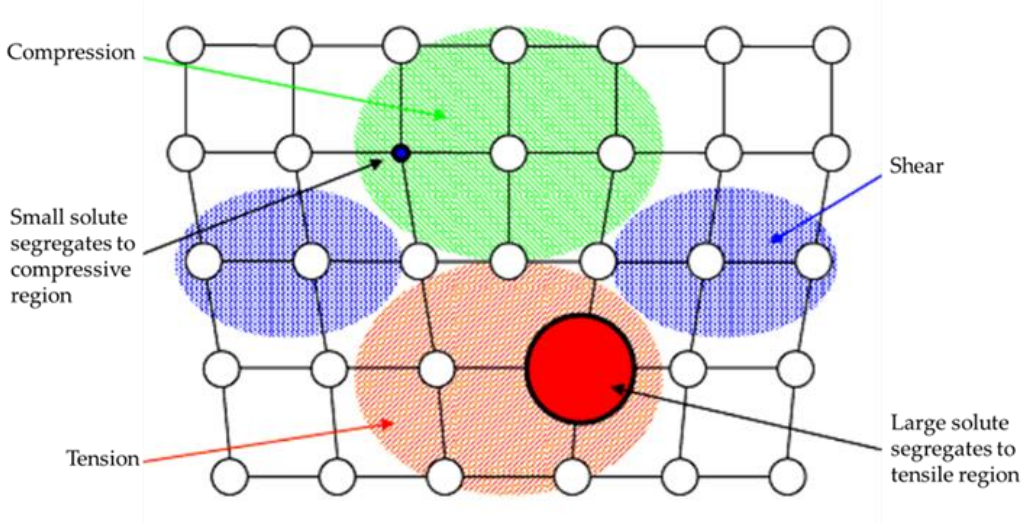

Figure 4.2: Interaction of solute atoms with the crystal lattice [142].

If the size of the atoms a is taking into account a size effect ε_b arises and can be described as [144]:

$$\varepsilon_b = \frac{1}{a}\frac{da}{dc}. \tag{4.1}$$

According to Fleischer [143] the following relation applies by taking the shear modulus into account:

$$\varepsilon_G = \frac{1}{G}\frac{dG}{dc}. \tag{4.2}$$

The total strain caused by both lattice and modulus mismatch arises as [143]:

$$\varepsilon_{cF} = \left|\varepsilon`_G - B_{\varepsilon_b}\right|, \tag{4.3}$$

whereby B is an experimentally determined constant and $\varepsilon`_G$ is defined as:

$$\varepsilon`_G = \frac{\varepsilon_G}{1+\frac{|\varepsilon_G|}{2}}. \tag{4.4}$$

Fleischer's approach is based on the interaction between moving dislocations and practically static foreign atoms that are statistically distributed on lattice sites. These static foreign atoms act as frictional forces against the direction of movement of the dislocation lines. The order of interaction is determined by the mean distance between the foreign atoms [91]. The critical shear stress results from ε_{cF} according to Fleischer and the concentration c as follows [145]

$$\tau_{cF} \backsim \varepsilon_{cF}^{\frac{3}{2}} c^{\frac{1}{2}}. \tag{4.5}$$

Further investigations in this regard were carried out by Labusch [146] postulating the interaction of size and modulus effect in the following correlation

$$\varepsilon_c = \sqrt{\varepsilon`_G^2 + B_{\varepsilon_b}^2}. \tag{4.6}$$

The relationship between critical shear stress with the parameter ε_c is described as follows:

$$\tau_{cL} \backsim \varepsilon_c^{\frac{4}{3}} c^{\frac{2}{3}}. \tag{4.7}$$

Labusch extended Fleischer's approach by means of statistical theory and took into account the mean statistical distance of the solutes along a dislocation line.

The elastic interaction effects (size effect and modulus effect) dominate solid solution strengthening for most crystalline materials. However, in some materials chemical bonding is also significant. For example some of the charge associated with solute atoms of dissimilar valence remains localized around the solute atom [142]. Other types of solid solution strengthening effects, such as stacking fault interactions or order hardening (short range order interaction, long range order interaction), can also occur but are not discussed further here.

Strengthening by grain size reduction

Strengthening in polycrystals due to grain boundaries has been experimentally established by Hall [147], [148] postulating a relation between the grain size and the yield stress. Grain boundaries act as barriers to the movement of dislocations, which cannot penetrate due to the discontinuity of the crystal planes at the grain boundaries [85]. This leads to a dislocation pile-up against the grain boundaries, thereby causing a stress concentration. If a critical stress level is reached, the activation of the gliding system of the neighboring grain is effected and yielding starts. The Hall-Petch theory [147], [148] describes a relation between the yield point R_e and the grain diameter d considering k as a measure of the local stress needed to initiate plastic flow at the grain boundary and σ_0 as the resistance to dislocation motion in the grain

$$R_e = \sigma_0 + \frac{k}{\sqrt{d}}. \tag{4.8}$$

The strengthening contribution due to grain refinement σ can be calculated on the basis of

$$\Delta\sigma = \frac{k}{\sqrt{d}}. \tag{4.9}$$

With decreasing grain size and thus, increasing strength due to grain refinement, the ductility of the material does not suffer any losses. The disadvantage, however, is that with increasing temperatures grain boundaries display an increase of the atomic disorder degree accompanied by increased diffusivity and mobility of the grain boundaries resulting in softening of the material [149]. Furthermore, grain boundary sliding is more pronounced at higher temperatures [85]. Strengthening by grain size reduction is therefore only advantageous in the low temperature range.

Work hardening

Work hardening (or strain hardening) increases the strength of a metal material due to plastic deformation. When a metal is plastically deformed, dislocations move and additionally they are generated originating from dislocation sources such as Frank-Read sources [85]. The higher the dislocation density within a material, the more it will interact and become pinned or tangled. This results in a decrease in the mobility of the dislocations and thus a strengthening of the material

occurs. The influence of dislocation density on the strength of the material can be estimated considering that a dislocation is perpendicular to dislocation obstacles, which are arranged at a distance of 2λ (assumed distance of the dislocation obstacles) and the dislocation obstacles can be cut (in contrast to the Orowan mechanism). The increase of yield strength due to dislocation obstacles $\Delta\sigma_{WH}$ can be expressed as follows [85]

$$\Delta\sigma_{WH} = \alpha M_T G b \sqrt{\rho} \tag{4.10}$$

where α is a constant between 0.1 and 0.2 according to [85], M_T the Taylor factor to convert shear stress to tensile stress considering an uniaxial load and ρ the dislocation density, defined as number of puncture points per unit, and

$$\sqrt{\rho} = \frac{1}{2}\lambda \tag{4.11}$$

applies. However, the increase in dislocation density also results in a reduction of ductility, which can be problematic if the ductility is inherently low. Another disadvantage is that with increasing temperatures the mobility of dislocations increases and strength caused by work hardening decreases due to recovery processes.

For the sake of completeness hardening mechanisms like second phase strengthening and precipitation hardening also have to be mentioned. Both mechanisms play a minor role in the conventional MA process and MA is currently used as the method of choice for doping powder material with reinforcing particles for subsequent processing steps [80]. Second phase strengthening by intermetallic phases, such as silicides or borides which occur in V-Si-(B) alloys impede dislocation movement and affect mechanical properties directly via their volume fractions and distribution. Due to the obstacle effect particles will be cut or bypassed (Orowan mechanism) by dislocations. Strengthening depends on type of particles (i.e. coherent, semi-coherent, and incoherent), particle radius, volume fraction and type of distribution of the particles.

4.1.2 Kinematics in planetary ball mills

In planetary ball mills, comminution takes place in a grinding vial in which a mixture of freely moving grinding media and ground material circulates. Balls, cylpebs, rods or stones can be used as grinding media. In this work, grinding balls made of stainless steel with a diameter of approx. 10 mm were used. The mechanical loading of the feed stock is induced by impacts between the grinding media as well as between the grinding media and the jar walls. The energy required for this is supplied to the grinding media by rotating the grinding jar (cylindrical). In a planetary ball mill, several grinding jars are arranged eccentrically on a turntable, the so-called sun wheel. The functional principle of planetary ball mills is shown in Figure 4.3 a). The grinding jars rotate with the sun wheel and at the same time in opposite directions on their own axis. Movement states are aspired in the grinding jar that resemble the cataract effect in horizontally running ball mills, which is described in [150]. However, the grinding balls in the planetary ball mill have a significantly higher impact energy compared to gravity ball mills due to their higher speed and the superimposed rotational movement, since the effective centrifugal acceleration can reach a

multiple of the acceleration due to gravity. This results in a very high grinding performance or a correspondingly short grinding time [151]. The movement of the grinding media depends on the speed and geometry of the planetary ball mill as well as of the degree of filling and the external and internal friction. Figure 4.3 b) shows various modes of ball motion occurring in a planetary ball mill. In contrast to the ball mill, the grinding media movement in the jars of the planetary ball mill is not only determined by the rotational speed, but also by the gear ratio $\frac{\omega_v}{\omega_e}$ and the radius ratio $\frac{r_V}{r_M}$ [151]. Since the geometry of the planetary ball mill is specified, the rotational speed is left as a variable for regulation. When the rotational speed is too slow, the balls roll back down the vessel side (sliding mode), while a too high speed results in high centrifugal forces and keeps the balls from falling (centrifugal mode) and only pressure and friction applies. Under optimal conditions, the grinding balls are lifted up along the jar wall, become detached and collide with the material to be milled (cataract mode). This type of motion leads to impact loads, which occurs additional to the stress induced by pressure and friction due to the simultaneous cascading of the balls. The increased energy transfer in planetary ball mills enables mechanical alloying, which was explained in Section 4.4.1.

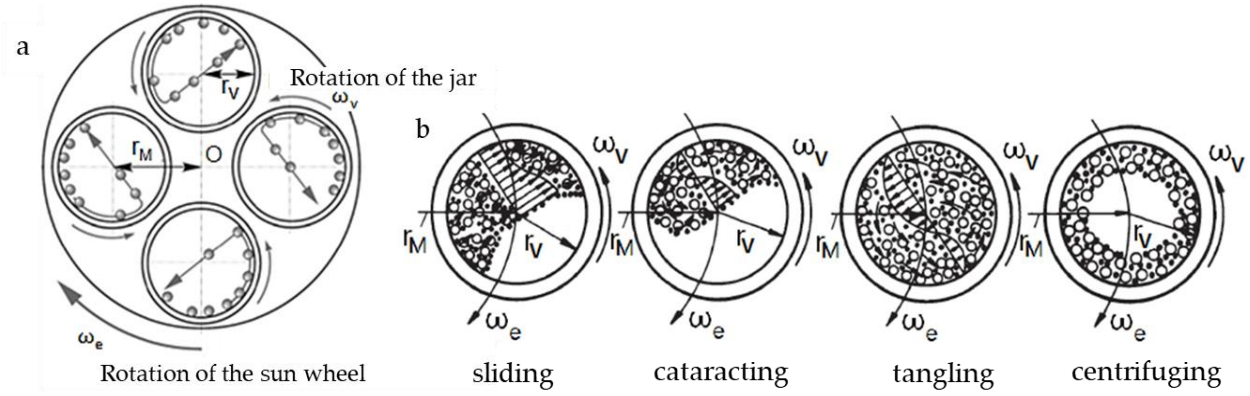

Figure 4.3: a) Operating principle of a planetary ball mill and b) modes of ball motions in a planetary ball mill [151].

Homogeneously structured powder particles with a small deviation in particle size can be created if there is a balanced relationship between comminution and welding processes. The grinding progress depends crucially on the energy that is transferred from the grinding balls to the material to be ground during the collision events. If previously only the type of movement of the balls was considered, the effect on the powder material is now also contemplated. The grinding or rotation speed determines the energy input and thus the influence on the powder material as follows: A low rotational speed is accompanied by a low energy input, which can lead to strong structural inhomogeneities, so that longer grinding times are required in order to achieve a homogeneous structure or a supersaturated solid solution [140]. On the other hand, if the speed is too high grinding balls might heat up and thus the powder might heat up as well, which leads to a sticky behavior among the powder particles as well as the jar wall due to an increase in

ductility with rising temperatures. In addition, a high rotational speed promotes abrasion of the ball and jar material, which subsequently contaminates the powder material. With increasing ball-to-powder mass ratio, the energy input initially increases. However, an unbalanced ball-to-powder ratio can turn into reduction of energy input, since the free path length of the balls is significantly reduced. In general, the optimized ball-to-powder ratio is between 10:1 and 20:1. The energy input is also determined by the ball material, whereby the density of the balls used is decisive. Balls and grinding jars made of metal (stainless steel, tungsten carbide) can be used, but ceramic materials (agate, zirconium oxide) are also possible [138]. Since in this work only grinding material and grinding jars made of stainless steel were used, this field will be left undiscussed here. However, in Ref. [152] the milling process of V-Si-B alloys with different grinding materials was investigated.

Various authors [138], [153], [154] dealt with the calculation of the force and energy transfer in a planetary ball mill during MA. The working principle of the planetary ball mill has already been described in the previous section. The forces acting in a grinding jar are shown in Figure 4.4.

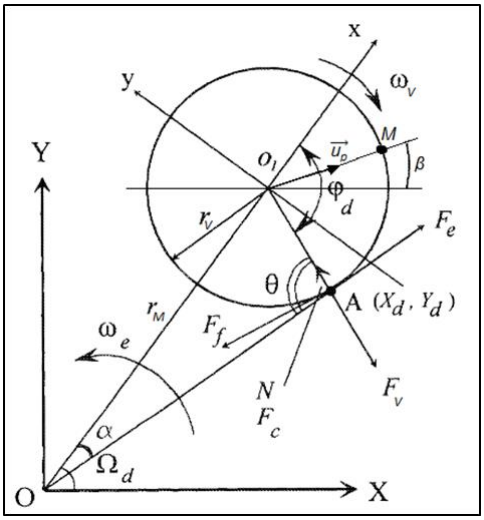

Figure 4.4: Acting forces and moments during the grinding process in a planetary ball mill [58].

According to Lü and Lai [138], the following forces act on a mass point A:

- the centrifugal force F_v caused by the rotation of the grinding jar,
- the centrifugal force F_e, which acts outwards from the center of the sun disk,
- the Coriolis force F_c,
- the friction force F_f due to the interactions between the grinding balls and the jar wall,
- the gravitational force.

The grinding ball is assumed to be a point mass for the following descriptions. Furthermore, according to Lü and Lai [138], the frictional force F_f can be neglected as well as the influence of gravity since the ball motion takes place in a horizontal position. According to this, the forces can be summarized within classical physics as follows

$$\sum \vec{F} = m \cdot \left(\vec{F}_e + \vec{F}_v + \vec{F}_c\right) \tag{4.12}$$

where m is the mass and $\overrightarrow{F_e}$, $\overrightarrow{F_v}$ und $\overrightarrow{F_c}$ are the amounts of the individual acceleration vectors. These acceleration vectors result from [138]

$$\overrightarrow{F_e} = \overline{OA} \cdot \omega_e^2 = \frac{r_M + r_v + \cos\varphi}{\cos\alpha} \cdot \omega_e^2 \tag{4.13}$$

$$\overrightarrow{F_v} = r_v \cdot \omega_v^2 \tag{4.14}$$

$$\overrightarrow{F_c} = 2 \cdot \omega_e \cdot \omega_v \cdot r_v. \tag{4.15}$$

4.2 Theoretical description of the energy input during MA

4.2.1 Numerical calculations of the MA process

To assess the effects on the multi-component powder material during the ball milling process well-accepted approaches for modeling of grinding processes were considered. Maurice und Courtney [155] showed in numerical calculations that solely the collision events, which occur between the milling balls, the powder particles and the vial wall are responsible for the phase transition in the ground powder material. Investigations of Kano et al. [156] on ball motion patterns during the milling process validated (by means of DEM simulations) the presence of the important cataract regime, where the grinding balls are lifted up the wall, become detached and drop down onto the powder particles to be milled. This effect, also mentioned by Lü and Lai [138], is of high importance during the ball milling process as the cataract motion provides the required impact forces and leads to a high energy transfer which is necessarily needed for comminution and cold welding processes during MA [157],[71]. The amount of energy that can be transferred to the powder particles depends on the kinetic energy of the milling balls immediately before the collision occurs [158]. This kinetic energy E_{kin} of a milling ball is defined by Abdellaoui and Gaffet [159] by

$$E_{kin} = \frac{1}{2} m_b v_c^2 \tag{4.16}$$

In this equation, m_b is the mass of a milling ball and v_c its velocity at the time of collision between the milling ball, the powder particle and the vial wall. v_c can be determined by the following equation:

$$v_c = \sqrt{r_m^2 \omega_e^2 - 2 r_m \omega_e r * \omega_r sin\alpha + r^{*2} w_r^2} \tag{4.17}$$

where r_m is the distance between the center of the vial and the center of the sun disc of the planetary ball mill, ω_e is the angular speed of the basic disc, r* the effective radius (i.e., the

difference between the vial radius and the ball radius), ω_r is the angular speed of the vials and α the angular position of the ball in the vial. A description of the geometric arrangement and the specific dimensions of the planetary ball mill can be found above in Figure 4.4. Calculations in this work based on the geometry of the planetary ball mill PM 400 (Retsch) operated at a rotational speed of 200 rpm (rotational speed of the sun disc), a steel vial with 250 ml volume, and an amount of 100 milling balls (d_{mb} = 10 mm) made of steel. Since the kinetic energy according to equation (4.16) considers only kinetic energy of a single milling ball, an estimation of the complete energy during the milling process requires the determination of the number of collisions within a defined period of time. For this purpose, the general formula of the angular frequency which is given by

$$\omega = \frac{2\pi}{T} \tag{4.18}$$

was used [160]. ω is defined as the angular speed and T describes the circulation path time of a ball in the vial. After transposing this equation and replacing ω with

$$\omega = \frac{v_c}{r} \tag{4.19}$$

the circular path time of a milling ball in a vial can be determined by

$$\mathrm{T} = \frac{2\pi \mathrm{r}}{\mathrm{v_c}}. \tag{4.20}$$

Since the cataract motion of the grinding balls comprises of a line movement along half of the vial wall and a fall distance until the impact event occurs, the estimation of the circular path time needs to consider this fall height [160] by using the equation

$$h = \frac{1}{2} g t^2. \tag{4.21}$$

In this fundamental physical law of the freefall, the term g is replaced by the centrifugal acceleration a, which can be determined by

$$\mathrm{a} = 4\pi^2 \mathrm{r n}^2. \tag{4.22}$$

In this equation r is the radius of the vial and n the rotational speed of the vial, obtaining from the gear ratio k of the planetary ball mill, which is defined by the geometry of the mill with

$$\mathrm{k} = \frac{\mathrm{n_{vial}}}{\mathrm{n_{sundisc}}} = -2. \tag{4.23}$$

The value for $n_{sundisc}$ is 200 rpm and reflects the rotational speed which is set as operating speed for the milling process. After solving equation (4.21) for the time t, an addition of the grinding ball motion time calculated from equation (4.20) and (4.21) results in a determination of the circular-path-time $t_{circular}$, which has to be considered for 100 grinding balls used in the current milling experiments. Table 4.1 presents the absolute velocity of grinding balls as well as the resulting maximum transferable kinetic energy of a ball, depending on the possible multilayer formation of up to three balls, which is considered as the ceiling option in the used vials. Since the effective radius (i.e., the difference between the vial radius and the ball radius) of the vial diminishes with the number of the milling balls´ layers, the circular-path-time $t_{circular}$ for a cataract motion of a ball

simultaneously decreases due to the lower drop in height. This results in an increase of collision events ranging from 71428 up to 136363 collisions within a second for the assumed 1 to 3 layers of balls (see Table 4.1). Variations in circulation path time and number of collision events due to changing ball motion patterns were also reported by Kano et al. in [156]. Further consideration of the numerical calculated values will be carried out in comparison to the simulated values in the next chapter (Chapter 4.2.2).

Table 4.1: Kinetic energy of the milling balls before impact in dependence of the number of ball´s layers calculated for the rotational speed of 200 rpm.

Layer of balls	1	2	3
v_c [ms^{-1}]	3.17	3.07	3.06
E_{kin}/milling ball [mJ]	20.62	19.38	19.27
$t_{circular}$ [s]	0.084	0.067	0.047
number of collisions [s^{-1}]	71428	89552	136363
P [W]	1474.99	1732.25	2429.88

4.2.2 Numerical simulation of the MA process based on DEM

The numerical simulations based on the Discrete Element Method (DEM) was kindly provided by Christine Burmeister from the Technische Universität Braunschweig. The following text passage was prepared in close cooperation with C.B. and also published in [161]. DEM allows the calculation of stressing conditions regarding frequency and energy and considers each grinding ball as a discrete element [162]. For each ball collision the forces of compression and shear are determined by using a contact model, here the contact model of Hertz [163] and Mindlin [164]. The resulting velocities and accelerations after the contact are calculated according to Newton's law of motion. Thus, each discrete collision event has a certain contact time and energy dissipation which can be extracted from the software. For simulating the commercially available program EDEM, which is well suited for ball milling applications [165], [166] but has limitations regarding computational capacity and number of computed elements, was used. The simulation considers the powder particles by the adjustment of boundary conditions, rather than as discrete elements [166]. For a sufficient reproduction of the system's behavior including powder particles, the coefficients of friction and restitution are determined by correlating experimental and simulation data [65], [167]. The coefficient of restitution provides the energy dissipation due to deformation and conversion, so it describes the fraction of kinetic energy that is converted into internal energy. At a restitution of one ($e = 1$) the contact is totally elastic and no energy is dissipated. At a restitution of $e = 0$ the maximum possible amount is dissipated into internal energy due to the totally plastic contact. The internal energy of a single collision then is calculated considering the energy and momentum conservation. By including the restitution, the stressing energy SE of a ball collision is determined to:

$$SE = \frac{m_{GM}}{4} {v_{rel,n}}^2 (1 - e^2). \tag{4.24}$$

While a collision of a ball to the vial wall is calculated as:

$$SE = \frac{m_{GM}}{2} {v_{rel,n}}^2 (1 - e^2). \tag{4.25}$$

The complex movement of balls and their different velocities inside the ball charge lead to a distribution of stressing energies. Thus, a mean value of stressing energy $\overline{SE}$ is used to discuss and to compare different parameter settings:

$$\overline{SE} = \frac{\sum SE}{Number\ of\ collsions}. \tag{4.26}$$

The mean value of stressing energy multiplied by the frequency of stressing SF as stressing events per second determines the calculated power P_{DEM}:

$$P_{DEM} = \overline{SE} \cdot SF. \tag{4.27}$$

The determination of the coefficients of friction and restitution requires an extensive need for time, while only a single parameter setting was simulated. Thus, suitable boundary conditions of a comparable system were chosen according to [166]: the coefficient of rolling friction $\mu_R = 0.01$; the coefficient for static friction $\mu_S = 0.7$ and the coefficient of restitution e = 0.2 [161].

While the numerical calculated results only allow an insight into the maximum possible performance, the conducted DEM simulations provide information about the performance that could be actually realized. Table 4.2 reveals the results from the DEM simulation as well as the used input parameters. The DEM indicates a value of 131980 collision events per second. By means of the calculated circular path time (Table 4.1) numerical calculated values presents values ranging from 71428 up to 136363 collisions per second depending on the position of the milling balls in the vial. Deviations can be the result of the more detailed considerations of the random ball motion patterns in the DEM simulation but both values are of the same order of magnitude and thus in good agreement. Figure 4.5 presents the differently developed kinetic energy of the milling balls (DEM). As assumed in the numerical calculations and approved in [156], the kinetic energy of the milling balls varies dependent on the position in the vial respectively the ball motion pattern. Accordingly, the simulation depicts kinetic energies of the balls (before impact occurs, Hertzian contact) which ranges from 15.7 mJ up to a maximum of 36.8 mJ. In comparison, the numerical calculated values (Table 4.1) ranging from 19.27 mJ up to 20.62 mJ. Conformity can be stated when taking into account the simplified model. However, these energies do not represent the effective dissipated energy. Out of DEM a dissipated energy of 0.037 mJ per hit was simulated which can be extrapolated more descriptive to $17.5 \cdot 10^3$ J for a milling duration of 1 h (considering no friction losses).

Table 4.2: Input parameters and results from DEM simulation of the milling process of Mo-Si-B powders in a 250 ml vial.

Input parameters	
rotational speed [rpm]	200
diameter milling ball [mm]	10
vial volume [ml]	250
amount of milling balls	100
Results from DED simulation	
dissipated energy per hit [mJ/hit]	0.037
number of collisions [s^{-1}]	131980
effective dissipated power [W]	4.88

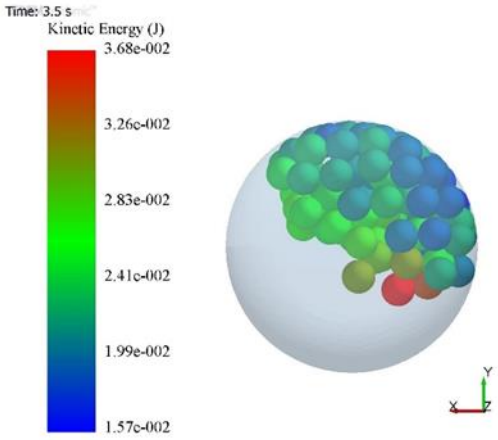

Figure 4.5: DEM simulation of the milling process in a planetary ball mill (Retsch PM 400) showing the evolved kinetic energy of the milling balls during process.

Regarding the power P of the system, determined by simulated data, which is given with a value of 4.88 W (effective dissipated power, Table 4.2), a significant lower value in comparison to the numerical calculated power, shown in Table 4.1; can be noted. Out of numerical calculations values of 1474.99 W (minimum) and 2429.88 W (maximum) was determined. Considering the real drive power of the used planetary ball mill, which is device-related given with 1500 W, it gets clear that the calculated power is too high as the whole kinetic energy cannot be dissipated during the collision events. The numerical calculations represent the maximum kinetic energy of the balls respectively the maximum resulting power before colliding. Numerical calculations of the dissipated energy or corresponding power could be done by considering the principle of conservation of energy. For a collision event of two bodies 1 and 2, the dissipated energy results as [160]

$$\Delta E = \frac{m_1 m_2}{2(m_1+m_2)} {v_{rel,n}}^2 (1 - e^2) \tag{4.28}$$

and is dependent on the relative velocity $v_{rel,n}$ and the corresponding mass for the carried out numerical calculations the relative velocity was equated to the absolute velocity of a ball. This only occurs if the ball hits a stationary body (v = 0) and practically does not happen in a planetary ball mill. Furthermore, the coefficient of restitution e is of interest. Perfect plastic impact events,

which would result in a restitution of 1 (e = 1), cannot be assumed. It is difficult to estimate the coefficient of restitution since the dissipated energy is not directly proportional to the kinetic energy. Thus, equation (4.28) is only mentioned for the sake of completeness and information on the dissipated kinetic energy can only be obtained from the DEM simulation.

5 Results and discussion: Alloying of V-Si(-B) powders

In Chapter 4 the theoretical mechanical alloying (MA) process as well as the energy appearing during the process were described in detail. The production of the powder material is an important step in the process chain for production of compact PM materials, since the properties of the powder material, in addition to the manufacturing technology, have a significant influence on the arising mechanical properties of the consolidated material. For powder material, properties such as particle size, particle shape, residual stress of the powders, and chemical composition are important criteria, since they influence powder flow, powder packing, interparticle friction, and thus, the resulting microstructure, especially porosity. Inconsistent material properties will result in inconsistent properties of the compacts [72]. In this chapter, results on investigations of MA V-Si(-B) powder material, manufactured for subsequent consolidation, are given.

5.1 Milling progress and phase formation of V-Si powder material

As mentioned in Chapter 2.3 PM processing routes typically start from powder mixtures or MA powder material. MA V-Si powder particles show up as saturated or supersaturated solid solutions due to the substitution of V atoms by Si atoms. In the following, the solid solution formation, microstructural evolution and the grindability of various V-Si systems as well as resulting powder material properties are investigated in detail in order to obtain basic knowledge about the behavior of this class of materials during MA as well as for subsequent consolidation.

5.1.1 Microstructural evolution

V–Si powder mixtures with Si concentrations of 2 at. %, 4 at. %, 15 at. % and 25 at. % were milled in planetary ball mill. Samples for analyses were taken by interrupting the milling process at defined periods of time (1 h, 2 h, 10 h, 20 h, 50 h and 100 h) to analyze the progress of milling.

As described in Chapter 4.1.1, MA is characterized by comminution and welding processes. The powder modification during MA using the example of the V-4Si (single-phase material) and V-25Si (two-phase material) is discussed in detail in this chapter. Additional results of alloy V-2Si and V-15Si are placed in the appendix. Figure 5.1 illustrates the microstructural evolution during milling. The corresponding XRD patterns are shown in Figure 5.2. At the initial state of the MA process elemental V and Si components are separate from each other and reflexes of elementary silicon (highlighted with *) and elemental vanadium (remaining reflexes) can be seen for the alloys V-4Si and V-25Si, shown in Figure 5.2 a) (0 h) and b (0 h). The intensity of the Si reflexes depends on the Si concentration of the alloy and increases with increasing Si concentration. With the onset of energy input by high energy ball milling, cold welding of the ductile V powder particles and comminution of the brittle Si particles occurs, resulting in binary powder particles with a layered

or particle/matrix structure. This progress strongly depends on the concentration of the alloying component, in this case Si, as well as the milling time. The solubility limit for Si in the V lattice is given at 1870 °C with a maximum of 7 at. %, whereas at room temperature only a solubility of 2.5 - 4 at. % Si is given [26]. Indicators for the dissolution of Si in the V lattice are the peak shifting (marked with the red line in Figure 5.2) as well as an elimination of the clear separation of the K_α and K_β peak due to the varying particle parameters by the formation of a V(Si) solid solution. While for the V-4Si alloy after 1 h of milling small amounts of elemental Si can be observed, the V-25Si composition still offers a remarkable amount of residual Si and a lamellar structure consisting of elemental V and Si is clearly visible (highlighted in Figure 5.1).

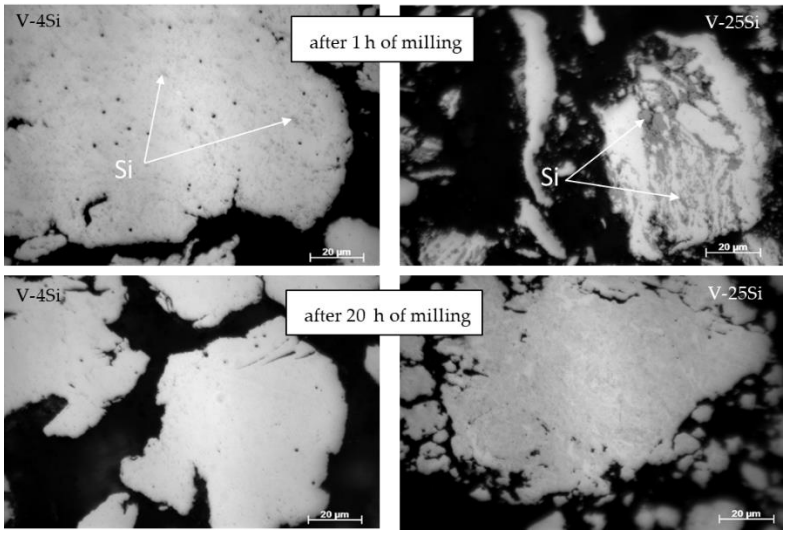

Figure 5.1: Microstructure of a V–4Si and V–25Si alloy after 1 h and 20 h of milling.

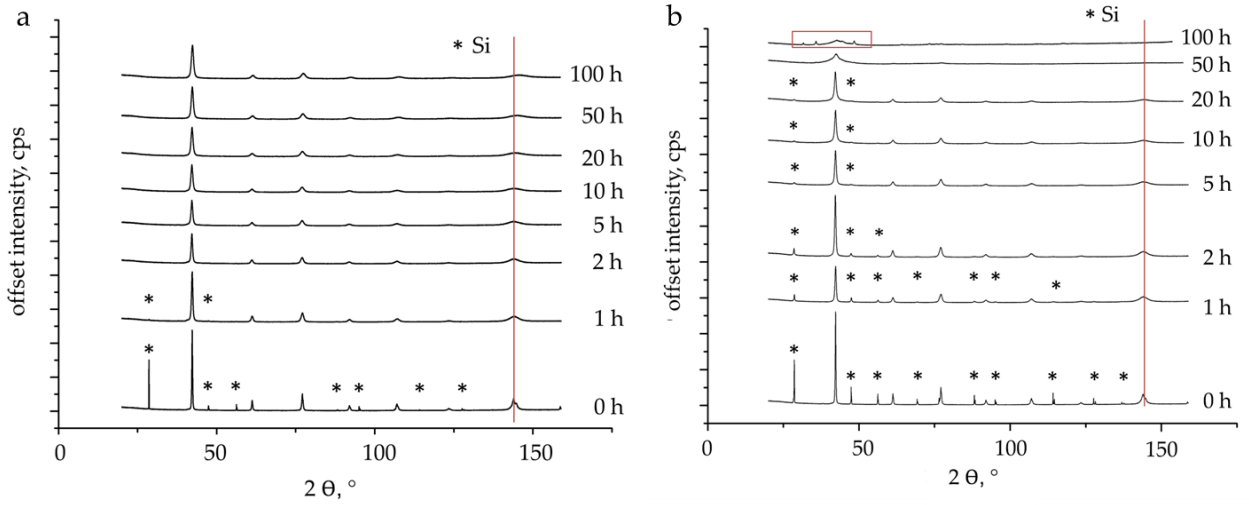

Figure 5.2: XRD analysis of V–Si alloys after milling for different time steps, a) V-4Si and b) V-25Si.

After 20 h of milling there is no elemental Si left in the V-4Si alloy. All Si is dissolved in the V lattice and no Si reflexes were detected in the XRD analysis of V-4Si after 20 h of

milling (Figure 5.2 a)). Furthermore, the microstructure consists of a single V(Si) solid solution phase. In comparison, the V-25Si alloy still offers elemental Si after 20 h of milling (Figure 5.2 b), 20 h) but the lamellar structure is now much finer and homogenization of the microstructure can be observed (Figure 5.1). This systematic investigation of the milling behavior with respect to the concentration of the alloying element confirms the need of an extended milling time with increasing Si concentration to achieve a single phase solid solution microstructure. Microstructural investigations revealed that a milling time of approximately 50 h is needed to achieve a complete supersaturated solid solution state for the V-25Si alloy (single phase V(Si) microstructure). Noteworthy is the mechanically induced formation of the V_3Si phase, which is the equilibrium phase for the alloy composition V-25Si [168], after a milling duration of 100 h (highlighted in the red box in Figure 5.2 b) respectively in Figure 5.3). The long milling time and the high impact energy evoke a thermal exposure of the powder material which leads to increased interdiffusion processes resulting in mechanically induced phase formation [97], [169].

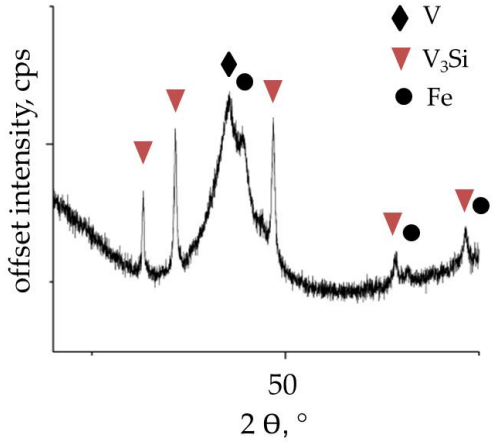

Figure 5.3: XRD data of V-25Si after 100 h of milling showing the mechanically induced formation of the V_3Si phase.

Furthermore, Figure 5.3 depicts the presence of iron peaks. Abrasion of the vial wall and balls (made of stainless steel) induced by long milling times and the associated high mechanical stresses has been identified as a significant source of contamination of powder materials in the MA process. Table 5.1 depicts the iron contamination for the various V-Si alloys with respect to the milling time. Notable amounts of iron contamination of the V-Si alloys could be detected from a milling time of approximately 20 h. In addition, a significant increase in iron contamination with increasing Si concentration can be observed for the milling time of 100 h. With increasing Si concentration there is an increase of the solid solution hardening effect of the MA powder material. Increased hardness of the powder material leads to increased abrasion of the grinding tools [170]. Since the effect of iron contamination on the V-Si system has not yet been sufficiently investigated, milling times exceeding 50 h should be avoided.

Table 5.1: Iron contamination of the various V-Si alloys with respect to the milling time.

	Fe concentration, at. %			
milling time, h	V-2Si	V-4Si	V-15Si	V-25Si
1, 2, 5, 10	<2	<2	<2	<2
20	2.2	2.3	<2	<2
50	3.0	4.1	3.2	3.8
100	4.8	8.0	10.5	29.8

Further impurities can be attributed to the grinding atmosphere. Typically, MA processes are carried out under exclusion of oxygen to protect the reactive new surfaces that are created during MA (fracturing) from oxidation. To this end, the handling of the powder material and the MA process is performed using a protective argon atmosphere. Energy losses from the occurring impact events lead, among others, to warming and thus, expanding of the milling atmosphere. For this reason, leaky grinding vials can lead to oxygen contamination during processing. Oxygen impurities result in the incorporation of oxygen in the V solid solution or formation of oxides, such as V_2O_5 or VO_2, which form at the grain boundaries and will affect further processing [170]. Accordingly, monitoring the oxygen content of the MA powder material is an important tool to achieve a satisfactory powder quality. In this work, commercially provided powder material with oxygen concentrations of 5100.5 ppm ± 429 ppm for pure V and 10783.9 ppm ± 350 ppm for pure Si powder were used. After MA of 20 h V-(2, 4, 15, 25)Si exhibit values ranging from of 5548 ppm - 6588 ppm. For MA of 50 h as well as 100 h no significant increase of the oxygen concentration was observed, which leads to the conclusion that the atmosphere in the vials is stable during the MA process.

5.1.2 Particle size distribution

The influence of MA on the powder particle size of the V-Si alloys is shown in Table 5.2. At the initial stage of the process (0 h MA) the median powder particle size of the V-Si composites ranges from 30 μm to 45 μm, depending on the Si concentration. For alloys with a low Si concentration (2 at. %, 4 at. %), which is the brittle component in the alloy composition, a significant increase of particle size after 2 h of milling was observed, as the high amount of the ductile V promotes welding processes. A balance between comminution and welding establishes after a short milling time, as the Si is already dissolved in the V lattice at this time, and results in a narrow range in particle size distribution (shown in Figure 5.4 b) and c)). The further MA process for both, the V-2Si and V-4Si alloy, is accompanied by a decrease in particle size as a result of the work hardening during milling. Alloys with a high concentration of Si (15 at. %, 25 at. %) show a different behavior. Starting from the initial particle size, there is only a slight increase in size at the beginning of the MA process (MA of 2 h). As the milling time progresses, the particle size decreases to a level below the initial particle size, which can be attributed to the high amount of the brittle component Si. Comparing the particle sizes after 2 h of MA, the V-2Si sample has a median particle size of 101.2 μm whereas the alloy V–25Si has an average particle size of 40.1 μm. A higher concentration of the brittle component Si thus leads to a dominance of comminution processes, resulting in faster reduction of the median particle size (Table 5.2). Another important

powder characteristic is sphericity Ψ (after Wadell [72]), which is a parameter for how uniformly round a particle is (Ψ = 1 -> fully spherical, Ψ < 1 -> not spherical) [171]. In addition to the influence of the particle size, the sphericity is a decisive characteristic for the flowability of the powders. The more uniform the particles, the better the flowability [72], [171].

Table 5.2: Sphericity Ψ and particle sizes and of the V–Si particles after different milling times.

	V-2Si		V-4Si		V-15Si		V-25Si	
milling time	Ψ, -	d_{50}, µm	Ψ, -	d_{50}, µm	Ψ, -	d_{50}, µm	Ψ, -	d_{50}, µm
0h	0.42	29.8	0.59	31.2	0.58	34.8	0.61	45.1
2 h	0.47	101.2	0.49	77	0.74	50.8	0.94	40.1
10 h	0.32	83.8	0.35	77.9	0.41	48.6	0.79	33.3
20 h	0.36	68.8	0.34	65.3	0.62	36.1	-	-
100 h	0.42	45.7	0.43	37.7	0.95	29.8	0.55	21.5

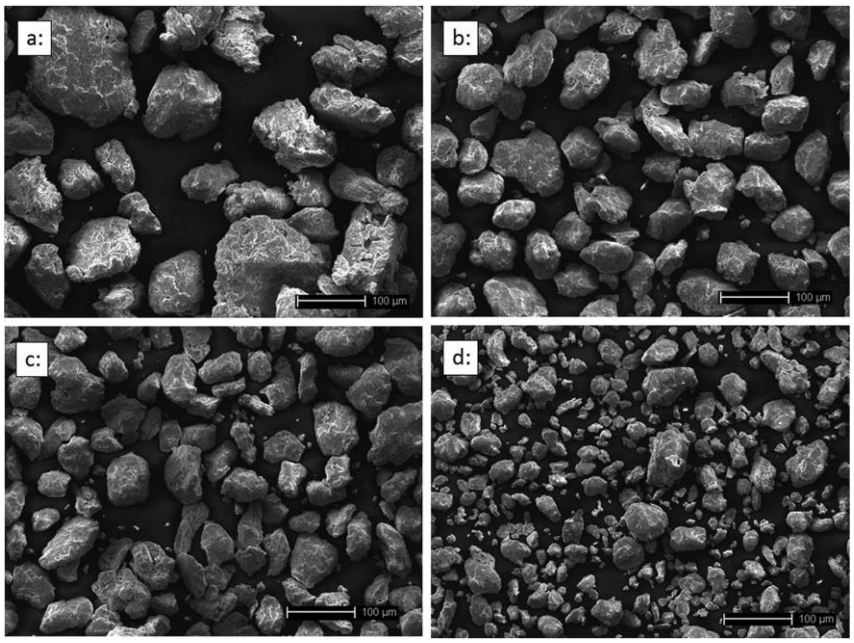

Figure 5.4: SEM micrographs of V–4Si powder particles after different milling durations, a) 2 h, b) 10 h, c) 20 h, and d) 100 h.

Figure 5.4 gives an impression of the true particle shape of the V-4Si alloy. The corresponding sphericity values (Table 5.2) are all below 0.5, which indicates a relatively high degree of irregularity. With increasing Si concentrations (15 at. % and 25 at. %), the sphericity of the particles approaches more to value Ψ = 1. While a high amount of V leads to pronounced welding and results in an obviously more irregular shape, the higher influence of the brittle Si promotes comminution with more regularly shaped particle morphologies. This behavior can be considered as valid trend for this class of material. For further processing via PM routes, such as FAST, however, the particle morphology is less important in comparison to the pre-stressing due to

impact events during MA. Induced lattice distortion or solid solution hardening can have a negative effect concerning the compressibility of the powder material [72], [80].

Fracturing and comminution as well as welding processes, which are essential for the progress of MA, are highly energy-consuming. In Chapter 4, a consideration on the energy input during milling in a planetary ball mill has already been given. The efficiency, which is the relationship between the effective work and the total work spent on the comminution process, is often below 1 %. Furthermore, the energy losses lead to warming of the balls and vials, the powder particles and the milling atmosphere [151], [172]. In the following, an evaluation of comminution and welding processes during MA as a function of the required work will be described by means of half empiric models, derived from the well-known and established Bond work index (method for characterizing the comminution behavior) [173]. The model was developed in collaboration with a student research project and has already been published in [45]. Comminution models, as described by Rittinger, Kick and Bond, relate the specific comminution work W_S to the process result, which is determined by the particle size d. The theory of Bond can be used to describe the comminution process for a collective of particles in particular for comminution processes in a planetary ball mill [173]–[175]. The general comminution law of Bond is given by:

$$W_{s,B} = 10W_i\left(\frac{1}{\sqrt{d_{F,80}}} - \frac{1}{\sqrt{d_{I,80}}}\right) \tag{5.1}$$

where $W_{s,B}$ is the specific comminution work, $d_{F,80}$ the 80%-particle size of the final product and $d_{I,80}$ the 80%-particle size of the initial particles. The work index W_i indicates the specific work spent on the comminution process, which is needed to grind the powder particles from an infinite size to a particle size of $d_{F,80}$ = 100 µm [176]. Since experimental studies have shown that the work index W_i from Equation (5.1) differed for ultrafine powders milled in a ball mill, Bond [173] suggests a correction factor A_i (Equation (5.2)) if the resulting particle size is expected to be below 70 µm. This correction factor is necessary to compensate the energy losses that occur during ultrafine size reduction since sticking particles on the milling tools lower the effectiveness of the impact processes:

$$A_i = \frac{d_{F,80}+10.3}{1.145 d_{F,80}}. \tag{5.2}$$

Bond [173] derives this empiric correction factor A_i from a milling process of cement clinker which can be transferred to other materials like quartz [156], talcum [156] and gold ore [177]. By transposing and multiplication of Equations (5.1) and (5.2) the modified work index W_{ic} in mJ for ultrafine size reduction according to Bond [173] arises as follows

$$W_{ic} = \frac{0.1145 d_{F,80} W_{s,B}}{(d_{F,80}+10.3)\left(\frac{1}{\sqrt{d_{F,80}}} - \frac{1}{\sqrt{d_{I,80}}}\right)} \tag{5.3}$$

Basically, this modified work index W_{ic} can be seen as a kind of grinding resistance representing the reciprocal value of the grindability [178]. As a result, the grindability k of the powder material,

which depends on the material properties and the initial particle size of the powder, can be expressed by the equation

$$k = \frac{1}{W_{ic}} \tag{5.4}$$

The amount of grindability k increases with decreasing resistant to grind [178]. Investigations by Kano et al. [156], [178] for planetary ball milling processes lead to the conclusion that the comminution work $W_{s,B}$ can be replaced by the impact energy E_{Kano}, which is defined by

$$E_{Kano} = \sum_{z=1}^{n_s} \frac{1}{2m_p} m_b {v_{r,z}}^2 \tag{5.5}$$

where m_p is the amount of powder, m_b the mass of the grinding balls, v_r the collision speed between two grinding balls or a grinding ball with the vial wall and n_s the number of collisions. Furthermore, Kano et al. [178], [179] present a relationship between the comminution rate K_P, the grindability k and the impact energy E_{Kano} as follows:

$$K_P = k\, E_{Kano} \tag{5.6}$$

Assuming that the number of hits is $n_s = 1$ and the amount of powder is negligible, the impact energy E_{Kano} corresponds to the kinetic energy E_{kin} calculated after Abdellaoui and Gaffet [159] (Chapter 4: Equation 4.16 and Table 4.1) resulting in

$$K_P = k\, E_{kin} \tag{5.7}$$

The comminution rate K_P describes the rate constant of the comminution process and gives a representative value for changes of the mechanisms during the milling process [156], [178]. Hence, the comminution rate K_P is used in this work to describe the dominating mechanisms during the MA process as a function of the impact energy.

Table 5.3 presents the determined grindability k and the comminution rate K_P for the alloys V-2Si, -4Si, -15Si, -25Si. For the steel grinding balls used at a rotational speed of 200 min^{-1}, the potential kinetic energy for one impact event was calculated with $E_{kin,\ Abdellaoui} = 20{,}6\ \frac{mJ}{hit}$ (Equation 4.16). The corresponding particles sizes $p_{F,80}$ used for the calculations are presented in Table A.1 in the appendix.

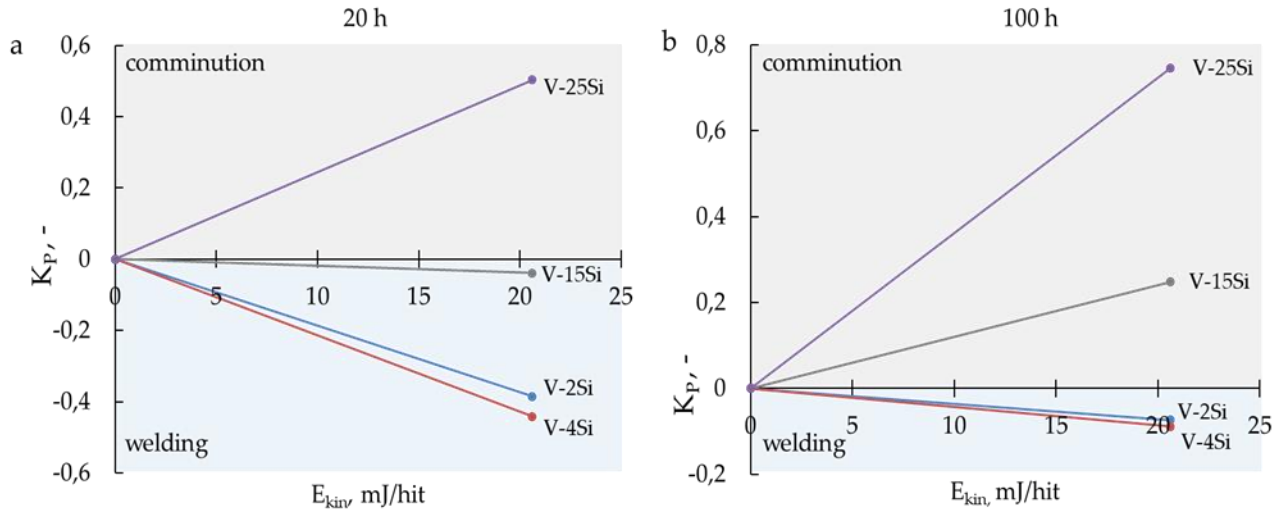

Figure 5.5: Comparison of the milling behavior of different V-Si alloys depending on the duration of milling.

Table 5.3: Grindability k and grinding rate K_P of V-Si powder material with different Si concentrations.

		V-2Si		V-4Si		V-15Si		V-25Si	
milling time, h	E_{kin}, mJ/hit	k, hit/mJ	K_P, -	k, hit/mJ	K_P, -	k, hit/mJ	K_P, -	k, hit/mJ	K_P, -
2	20.6	-0.0242	-0.4981	-0.0234	-0.4825	-0.0083	-0.1716	0.0127	0.2621
10	20.6	-0.0187	-0.3855	-0.0214	-0.4418	-0.0019	-0.0385	0.0178	0.3667
20	20.6	-0.0148	-0.3056	-0.0178	-0.3662	0.0058	0.1186	0.0244	0.5035
100	20.6	-0.0036	-0.0736	-0.0043	-0.0887	0.0120	0.2477	0.0362	0.7454

Based on these relations, Figure 5.5 illustrates the behavior of different V-Si alloys for a milling duration of 20 h and 100 h. The initial model of Kano [178], which provides the basis for the calculations shown here, solely bases on comminution processes of single-component powders. For the multi-component V-Si powder material studied here, an adjustment of the model was made as there is an influence of the opposite characteristics of the ductile alloying element V and the brittle alloying element Si. The comminution rate K_P may now have both negative and positive values. Positive values of K_P describe a fracturing behavior, which is equivalent to a reduction in particle size. On the contrary, negative values of K_P indicate an increase of the particle size due to cold welding or agglomeration processes occurring during MA. The alloy compositions and thus, the ratio between the brittle and ductile alloy components have a decisive influence on the grindability as it is depicted by the slopes of the graphs in Figure 5.5. While the low concentrated alloys (V-2Si, V-4Si) offer significant negative values of K_P (ductile V tend to welding), a reversal to positive values (≙ comminution) becomes apparent with increasing

Si concentrations. For the V-15Si alloy (20 h) K_P tends to values around 0, which means that the size reduction and particle growth processes are almost in an equilibrium state.

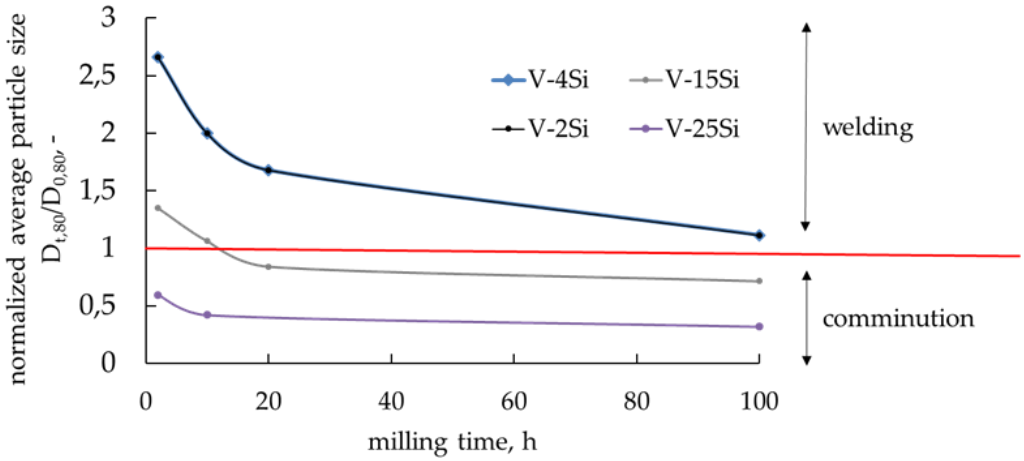

Figure 5.6: Normalized particle size $d_{F,80}/d_{I,80}$ for different V-Si powder as a function of grinding time.

The higher the quantity of the K_P value, the faster the respective process, comminution or welding, occurs. With increasing milling time, process equilibrium is reached and further material modification is characterized by comminution [140]. After 100 h of MA, alloys with low Si concentrations are still affected by the dominant ductile component V and the particle size is further increased compared to the initial particle size of the system (Figure 5.4 d), Table 5.2). Higher Si concentrations promote reduction of the powder particle size below the initial values ($K_P>0$). This behavior is also presented in Figure 5.6, where the normalized particle size $d_{F,80}/d_{I,80}$ (Table A.1) for different V-Si powder material is depicted as a function of milling time.

5.1.3 Hardening of V-Si powder during milling

Hardening mechanisms such as solid solution formation, grain refinement, and work hardening, which emerges during MA, lead to an increased strength as well as increased hardness of the powder particles. Figure 5.7 demonstrates the evolution of micro hardness during milling measured in the V(Si) powder particles.

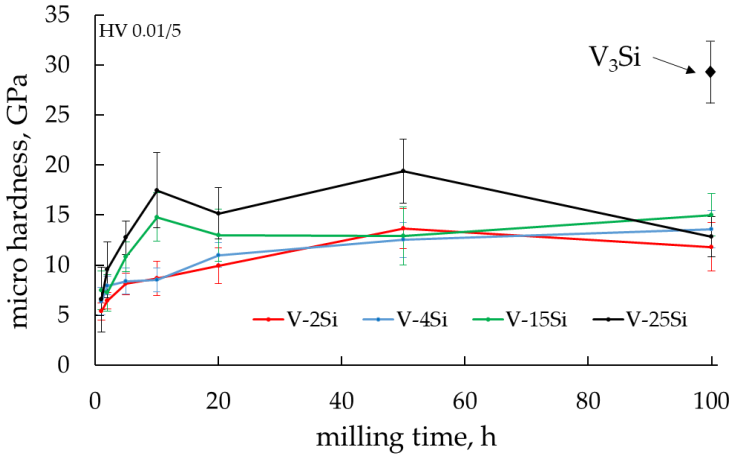

Figure 5.7: Evolution of micro hardness HV 0.01 of V(Si) solid solution powder particles during the mechanical alloying process. Mechanically induced formation of the V_3Si phase after 100 h of milling was observed for alloy V–25Si.

With increasing milling time all V–Si materials follow the trend of improved micro hardness (see Figure 5.7), which can be attributed to the presence of the hardening mechanisms mentioned above. The influence of solid solution strengthening, due to the distortion of the lattice structure by dissolved Si, was calculated using the approach of Labusch [146] (described in Chapter 4.1.1) for alloys in equilibrium conditions. The contribution of the solid solution hardening ranges between 0.015 GPa (2 at. % Si) and 0.02 GPa (4 at. % Si) and thus, provides hardening of the V-Si material in dependence on the Si concentration. In Figure 5.7 the steady improvement of micro hardness with increasing Si content is shown. This trend is also confirmed by a change in lattice parameters, where the lattice constant of the V-Si alloy increases with increasing amount of dissolved Si, since it has a larger atomic volume compared to V (see Table 5.6). During the initial milling process, the small and inhomogeneously distributed elementary Si particles (highlighted in Figure 5.1) may have an increasing effect on the measured hardness values [180]. For this reason, it was strictly attempted to indent the single solid solution phase only. Above the maximum solubility of Si in the solid state under equilibrium conditions (4 at. %) [26], the supersaturated solid solution powders show a significant increase of micro hardness for the V-15Si and V-25Si powder particles. The mechanism of formation of a supersaturated solid solution during MA for systems with positive enthalpy of mixing is described by Schwarz in [181] and bases on the parelastic interaction (lattice parameter effect) between the foreign atom and the elastic distortion field of a dislocation. Supersaturation of the matrix with alloying atoms near the phase boundary occurs and leads to an increased hardness of the powder particles. The large number of phase boundaries resulting from the formation of a lamellar structure during MA as well as the high dislocation density due to the strong plastic deformation of the powder particles accelerate this process. The formation of a nanocrystalline structure in the powder particle enables the formation of the supersaturated solid solution in the entire volume of the powder particles

[181]. Moreover, there is a significant effect on the hardness of the compound V–25Si after 100 h of milling caused by the mechanically induced formation of the silicide phase V_3Si resulting in two-phase powder particles. The respective black colored graph in Figure 5.7 depicts a constant decrease of the micro hardness of the solid solution phase in alloy V–25Si after 50 h of milling. During the mechanically induced formation of the V_3Si phase the Si concentration of the supersaturated solid solution decreases, which explains the drop to hardness values similar to those of the saturated solid solution powders of V–2Si and V–4Si. The determined micro hardness of the V_3Si phase is also marked in Figure 5.7 (black rhombus). It is approximately twice that of the solid solution phase and will contribute strongly to enhancing the hardness of the two-phase V(Si)–V_3Si powders which was produced after 100 h of high energy ball milling.

Furthermore, during MA and especially with increasing milling time, the dislocation density increases to a level where dislocation wall formation occurs [182]. As the energy impact progresses, grain boundaries are formed resulting in a nanocrystalline structure (Hall-Petch strengthening) [97], [148], [183]. By means of a Rietveld analysis of the reflex profile from the XRD data and the grain size as a function of grinding time was determined for the example V-4Si (see Table 5.4). The STEM micrograph of V-4Si after 2 h of milling in Figure 5.8 a) gives an idea of the true grain size and confirms the order of magnitude of the values shown in Table 5.4. Hall-Petch constant k, which is a measure of the local stress needed to initiate plastic flow at a grain boundary, was determined empirically from the Hall-Petch plot shown in Figure 5.8 b). The strengthening contribution σ due to grain refinement (Equation 4.9) can be found in Table 5.5.

Table 5.4: Grain size of V-4Si after different milling times determined by Rietveld analysis.

milling time, h	1	2	5	20	100
grain size, nm	13.5	11.3	9.3	8.4	8.5

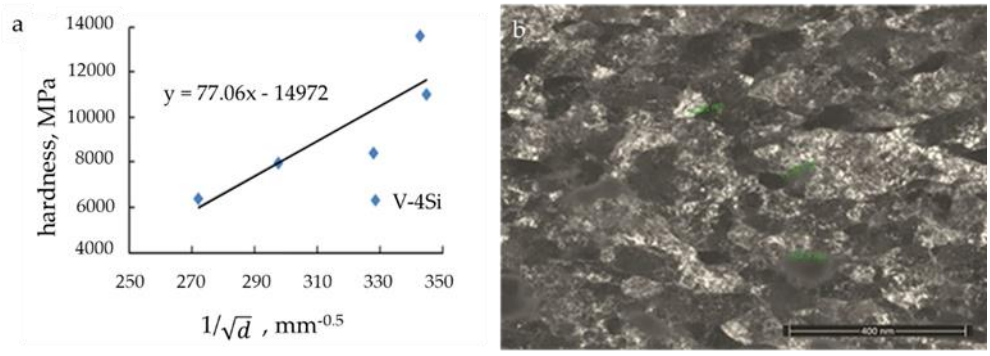

Figure 5.8: a) Vickers hardness of V-4Si as a function of grain size in a Hall–Petch plot and b) STEM micrograph of V–4Si after 2 h of milling [44].

Table 5.5: Hardening contributions (HV 0.01) of a V–4Si alloy after different milling times.

V-4Si milling time	microhardness V-Si alloy	microhardness elemental V	solid solution strengthening	grain refinement	work hardening
2 h	7.9 GPa	2.8 GPa	0.02 GPa	1.95 GPa	3.13 GPa
20 h	11.1 GPa	2.8 GPa	0.02 GPa	3.41 GPa	4.87 GPa

Additionally, plastic deformation due to ball-powder collisions during MA promote work hardening by increasing the dislocation density [85]. Table 5.5 provides an overview of the estimated contributions of the three superimposing hardening mechanisms using the example of V–4Si. Assuming that the total hardness value is a sum of the initial hardness of elemental vanadium powder material (2.8 GPa), the contributions of solid solution hardening, grain refinement and the work hardening effect, the contribution of the latter effect results from the others. The values in Table 5.5 allow the conclusion that work hardening is the dominating hardening effect during MA of this material. Followed by grain refinement, which is a competing mechanism, since too high dislocation densities (induced by constant deformation during MA) lead to a recovery due to grain boundary formation [184]. Both mechanisms and thus, the resulting grain size depends on the intrinsic properties (ductile or brittle behavior) of the components [182].

5.1.4 Heat treatment of V-Si powder material

As already mentioned, the powder material is faced with constant deformation during MA. The high concentration of lattice defects induced by MA leads to an increase of the free enthalpy of the material. Additionally, the high density of dislocations and vacancies as well as the large grain boundary surfaces cause a strong acceleration of the diffusion of the components. Both together promote the solid state reaction resulting in the formation of metastable or even amorphous and quasicrystalline phases during MA [185], [186]. Alloy V-2Si which has a negative enthalpy of mixing (located below solubility limit [26]) shows up as a saturated solid solution. V-Si alloys with a Si concentration > 4 at. % offer a positive enthalpy of mixing but MA can lead to formation of supersaturated V solid solution. This emphasizes that the powder material cannot be in a thermodynamic equilibrium, except from the V-2Si alloy as well as after mechanical induced V_3Si phase formation, as it was reported for 100 h of MA of the V-25Si alloy. Supersaturated solid solutions can be transformed into a thermodynamically stable state by heat treatment (HT). Precipitation of the silicide phase V_3Si for the V-rich V-Si system occurs. Figure 5.9 reveals the XRD analysis of the various V-Si alloys, showing precipitation behavior with respect to the annealing temperature (ramp 5 K/min, holding time 1 h).

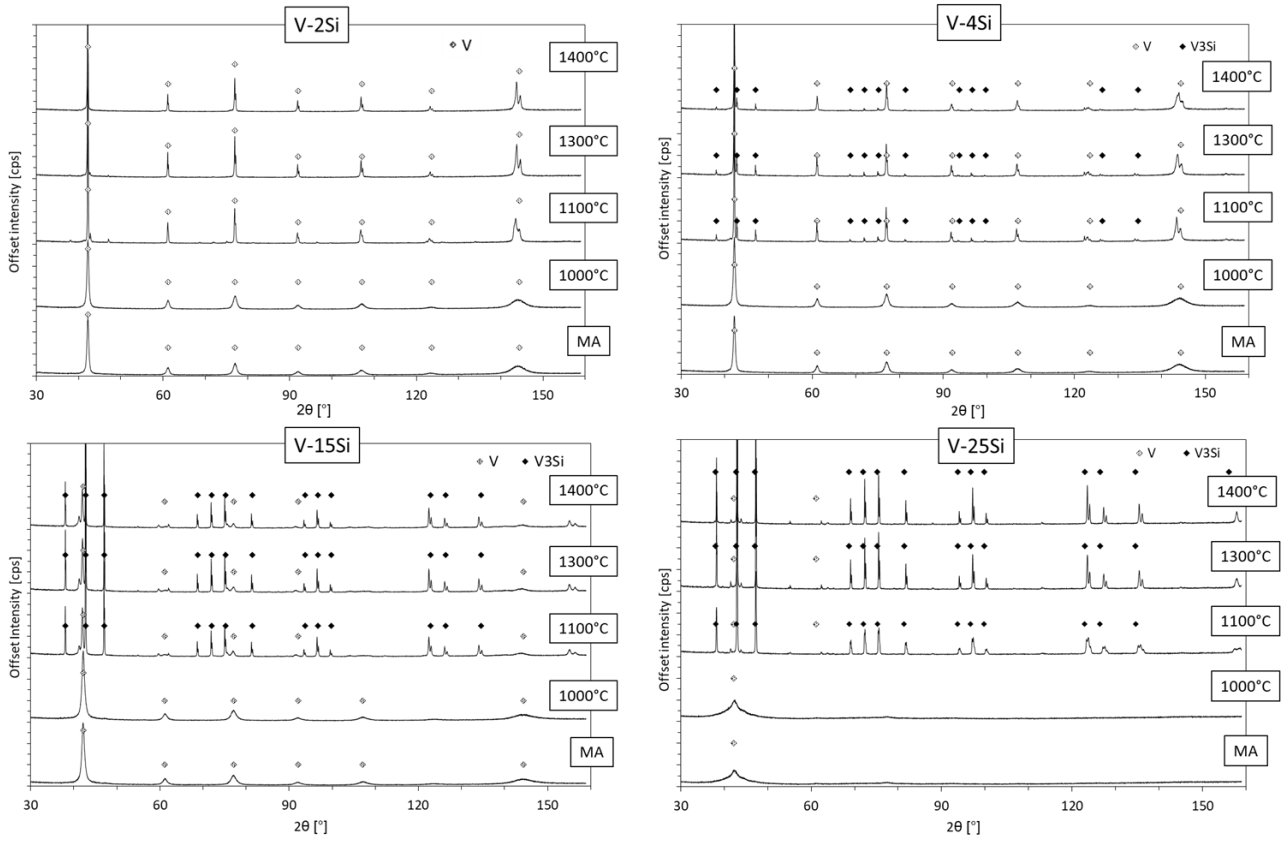

Figure 5.9: XRD analysis of MA V-Si powder material for different annealing temperatures.

For alloy V-2Si no obvious reflexes of a second phase after HT for the plotted XRD data was observed by Rietveld analysis (Table 5.6 and A.2), however, depicts a small amount of V_3Si phase ranging from 2 - 8 vol. % for the powder material annealed with 1100 °C and 1300 °C. For V-2Si heat treated at 1400 °C according to the phase diagram [26] no formation of the V_3Si phase was observed and alloy V-2Si remains as single phase V_{ss} powder material after HT. The small amounts of V_3Si phase can be attributed to an insufficient milling progress resulting in a local Si reservoir and are considered as a statistical deviation. With increasing annealing temperature, the detected V reflexes of the V-2Si alloy, i.e. at 2 θ = 145 °, sharpen and thus indicate recovery processes of the deformed MA material. From a Si concentration of 4 at. % (and higher) precipitation of the V_3Si phase can be confirmed by respective reflexes of the XRD analysis (see Figure 5.9, Table 5.6). Precipitation of second phases for MA materials consists only of nucleation, nuclei growth and ripening as the solid solution formation already took place during milling [72]. V-(4, 15, 25)Si show a beginning of precipitation processes from a temperature of 1100 °C onwards while V reflexes decrease with increasing Si concentration. Plotted XRD data in Figure 5.8 and corresponding SEM images of microstructural evolution of the powder material are shown in Figure 5.10 and visualize the precipitation of the V_3Si phase. There might be precipitations of the V_3Si phase at 1000 °C as well, but they are very likely below the detection limit of XRD analysis.

Rietveld analysis, shown in Table 5.6 (more detailed in Table A.2 in the appendix) give an overview of the determined volume fraction of the precipitated V_3Si phase. For V-4Si an amount of 19.41 vol. % at 1100 °C which decreases to 10.6 vol. % at 1400 °C was observed. The decrease of the amount of the precipitated V_3Si phase can be explained by the increased solubility of Si in V with increasing temperature. The binary V-Si phase diagram [187] depicts a solubility of 3 at. % Si at 1100 ° whereas the solubility of Si in V at 1400 °C increases to 4.2 at %. For V-15Si and V-25Si an amount ranging from 76.14 – 76.9 vol. % and 97.2 – 97.7 vol. %, respectively, was determined. The amount of 97.7 vol. % V_3Si phase for alloy V-25 Si, which is the equilibrium phase for the alloy composition, is in good agreement with the phase diagram shown in [187]. Figure 5.10 depicts the microstructural evolution of the HT V-Si powder material. Monitoring of the oxygen concentration, presented in Table 5.6, shows that HT leads to a significant increase of the oxygen concentration within the powder material. During the entire milling process attention is paid to the exclusion of oxygen, this can no longer be guaranteed to such a high standard for the heat treatment. In addition to the transport of the powders to the furnace, the treatment in the furnace also offers the possibility for contamination with atmospheric oxygen. However, the increase of the oxygen concentration determined does not show obvious effects on the powder material.

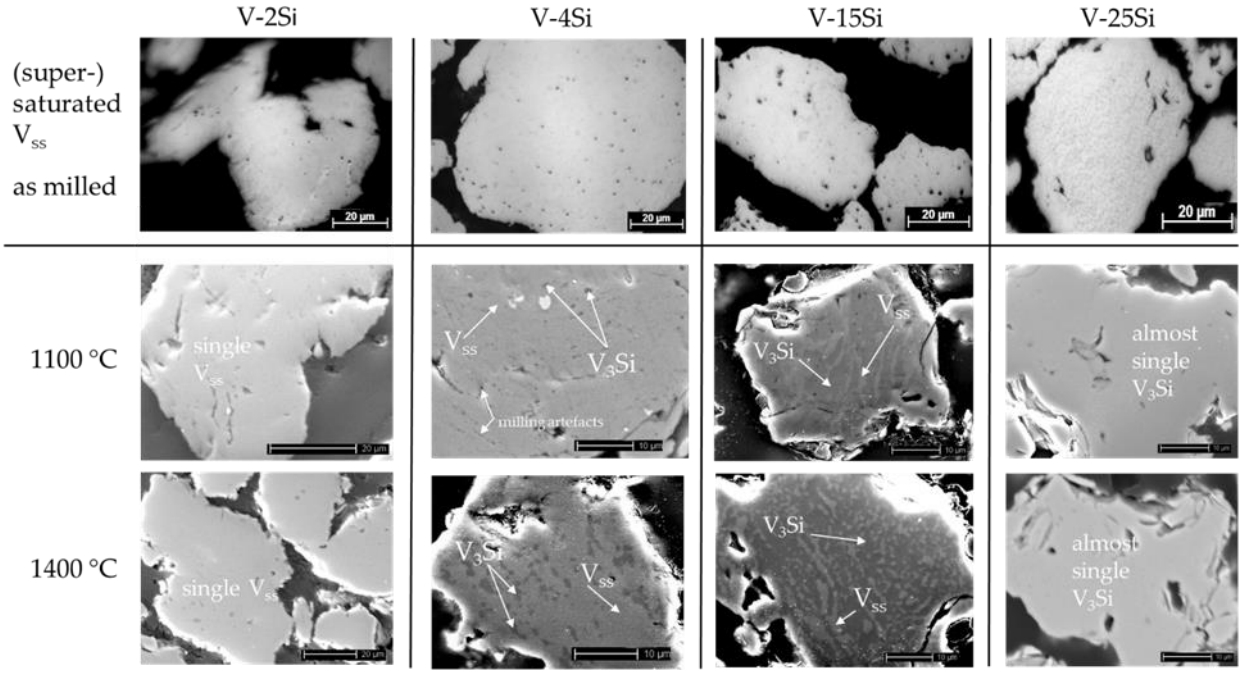

Figure 5.10: Microstructures of mechanically alloyed V-Si powder material after milling and after heat treatment of 1100 °C and 1400 °C.

Table 5.6: Properties and phase distribution of various V-Si alloys after heat treatment.

	lattice parameter V, Å	oxygen concentration, ppm	phase distribution, vol.%	
			V_{ss}	V_3Si
V-2Si				
as milled	3.033674	5943.2 ±234	100	-
1100 °C	3.036870	6338.8 ± 143	97.76	2.24
1400 °C	3.033898	11911.3 ± 1162	100	-
V-4Si				
as milled	3.03357	6143.7 ± 211	100	-
1100 °C	3.036396	9178.8± 437	80.59	19.41
1400 °C	3.033026	9718.09 ± 532	89.4	10.6
V-15Si				
as milled	3.030841	6001.1 ± 187	100	-
1100 °C	3.042284	9347.2 ± 773	23.86	76.14
1400 °C	3.043262	11174.1.±.1006	23.1	76.9
V-25Si				
as milled	3.041864	5548.1 ± 272	100	-
1100 °C	3.079467	7270.8.±.152	1.28	97.47
1400 °C	3.074448	11083.3 ± 1048	2.8	97.2

Micro hardness of the powder material increases with the beginning of precipitation of the V_3Si phase, as the hardness of the single V_3Si phase is significantly higher than that of the V_{ss} phase [11]. Figure 5.11 depicts the micro hardness of the powder particles and Table 5.6 the corresponding phase distribution. For alloy V-2Si no significant formation of a strengthening V_3Si phase was detected and the hardness remains constant within the range of standard deviation values. For alloy V-4Si no significant increase of micro hardness could be observed, though an amount of V_3Si phase with 10 – 19 vol. % was determined. This can be attributed to the small loads at HV 0.01 resulting in small very indents. It seems to be very likely that most of the indents were placed within the V_{ss} phase and thus, no representative increase of hardness could be determined. With increasing Si concentrations, the amount of V_3Si phase significantly increases and lead to a measurable increase in micro hardness for alloy V-15Si and V-25Si. As milled V-15Si provides a hardness of 14.69 ± 0.9 GPa due to solid solution hardening. The drop of hardness at 1000 °C is somewhat unexpected as the beginning precipitation of the V_3Si phase should result in in an increase of micro hardness of the material as it is shown for 1100 °C, 1300 °C and 1400 °C. The volume fraction of the V_3Si phase for alloy V-15Si was determined with 76 vol. % (1100 °C – 1400 °C) and leads to significant increase of hardness of the V-15Si powder material with a maximum hardness of 21.89 ± 3.1 GPa after heat treatment at 1400 °C. Alloy V-25Si, which offers the highest hardness of the supersaturated V_{ss} powder particles in this study, shows an increasing hardness with increasing heat treatment temperature up to 31.51 ±2.7 GPa (~ single

V_3Si phase). As the heat treatment was only conducted for 1 h, the driving force for precipitation of the V_3Si phase is subjected to the annealing temperature.

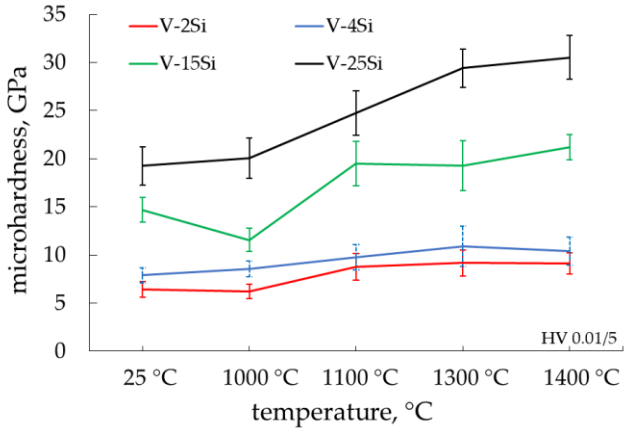

Figure 5.11: Micro hardness HV 0.01 of various V-Si alloys after heat treatment.

5.2 Milling and microstructural evolution of V-Si-B powder material

On basic investigations of powder material of the V-rich binary V-Si system, investigations of the ternary V-Si-B system follow. The addition of B leads to the precipitation of a second silicide phase, namely the V_5SiB_2 phase [48]. V-Si-B alloys out of the V-rich area of the ternary V-Si-B phase diagram offer great potential as structural material due to the presence of the ductile V_{ss} phase and the strength enhancing silicides V_3Si and V_5SiB_2 [15], [53]. The alloy system is still less investigated, especially in terms of powder metallurgy and accompanied phase formation. In the following studies, MA of this material as well as microstructural evolution of the powder particles is described.

5.2.1 Influence of different milling aggregates on milling progress and powder properties

The influence of milling parameters and grinding aggregate on the alloying process was investigated using a V-9Si-13B alloy. This alloy composition follows the well-known and structurally similar Mo-Si-B system and is said to have favorable properties due to the balanced phase distribution between V_{ss} phase and strengthening silicide phases [10], [188]. Investigations with stainless steel (SS) as well as tungsten carbide (WC) milling aggregates (milling vials and balls) and varying rotational speeds of the planetary ball mill were conducted. The parameter used for this purpose are listed in Table 5.7. For both grinding materials, stainless steel and tungsten carbide, MA with a rotational speed of 150 rpm and 200 rpm was conducted. An increased rotational speed of the ball mill leads to an increased input of kinetic energy (Table 5.7: E_{kin} collision) and promotes the milling progress in terms of homogenization of the microstructure as it is shown in Figure 5.12 using the example of milling for 2 h and 20 h.

Table 5.7: Milling conditions, process parameters and energy of collision in V-9Si-13B powders (SS - stainless steel, WC – tungsten carbide).

alloy composition (at. %)	V-9Si-13B			
grinding material	SS		WC	
rotational speed ball mill (rpm)	150	200	150	200
E_{kin} collision (mJ/hit)	11.6	20.6	11.9	21.1
milling time to achieve homogenization (h)	20-30	10-20	20-30	10
Fe impurities in the homogenized particles (at. %)	<2	<2		
WC particles in the homogenized particles (%)			0.2	0.45
Fe impurities after 50 h of milling (at. %)	<2	<2		
WC particles after 50 h of milling (%)			0.75	1.75

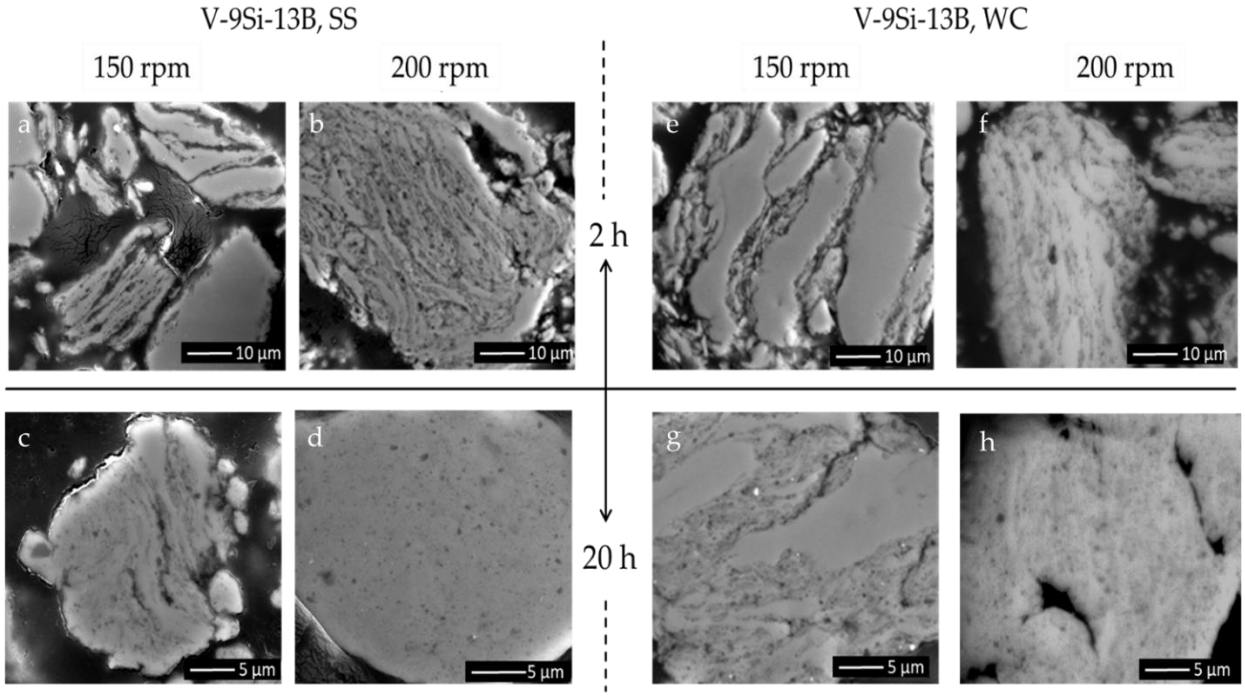

Figure 5.12: Microstructural evolution of V-9Si-13B powders using different grinding aggregates (a) – d): SS – stainless steel, e) – h): WC – tungsten carbide).

With an increase of the rotational speed from 150 rpm to 200 rpm the impact energy almost doubles from 11.6 mJ/hit to 20.6 mJ/hit for SS tools and from 11.9 mJ/hit to 21.9 mJ/hit for WC tools and lead to a clearly visible effect in terms of homogenization. After 2 h of milling all micrographs (Figure 5.12) of the powders milled with a rotational speed of 200 rpm show the formation of a lamellar microstructure consisting of individual layers of elemental V (light grey phases) and fragmented elemental Si and B (dark grey), which are embedded in between the ductile V layers.

In contrast, larger layers of elemental V, which is typical in an early state of MA, can still be found after a similar duration of milling using a rotational speed of 150 rpm. After 20 h of milling the microstructures of the powders make it obvious that a lower energy transfer into the powder material will reduce the progress of MA significantly and leads to an extended duration of the milling process to achieve homogeneous (supersaturated) solid solution powder material (Figure 5.12). Comparing the different grinding materials concerning their influence on milling progress one can state that there is no significant influence, as there is only a small difference between the collision energies of 0.6 mJ/hit. The milling progress for both grinding materials correlates proportionally with the increasing impact energy that is strongly influenced by an increased rotational speed. However, powder texture shows dependencies on the grinding material and milling duration. With ongoing milling progress, WC grinding tools cause an increased viscosity of the powder material and evoke strong consolidation of the particles earlier in comparison to powders milled with SS tools. The powder texture after different milling durations is described in Table 5.8.

Table 5.8: Powder textures of MA V-9Si-13B alloys using different rotational speeds (rpm) and grinding aggregates (SS, WC).

	V-9Si-13B powder texture after MA			
milling duration	SS, 150 rpm	SS, 200 rpm	WC, 150 rpm	WC, 200 rpm
1 h	fine and loose powder	fine and loose powder	fine and loose powder	fine and loose powder
2 h	fine and loose powder	fine and loose powder	fine and loose powder	fine and loose powder
5 h	fine and loose powder	fine and loose powder	loose powder with increased viscosity	sticky powder, increased viscosity
10 h	loose powder, increased viscosity	sticky powder, increased viscosity	mainly consolidated powder	mainly consolidated powder
20 h	consolidation of powder material	consolidation of powder material	strong consolidation of the powder	strong consolidation of the powder
50 h	strong consolidation	strong consolidation	-	strong consolidation

Milling behavior in the initial state is in good agreement with the previous experiment on MA of V-Si powder material as well as with the related Mo-Si and Mo-Si-B with concentrations in the range between 9 at. % and 15 at. % [66]. The XRD plots of the initial MA process are shown in Figure A.1 in the Appendix. After 20 h of milling the XRD analysis for all samples depict a supersaturated V_{ss} where the elemental Si and B are dissolved completely (Figure 5.13). While Si is dissolved in the V lattice only a small amount of Boron is dissolved in the solid solution. Boron has a small solubility [189] and a less pronounced effect on the lattice due to the comparatively

small atomic radius. It is assumed that Si substitutes the V sites and B occupies the interstitial sites as it is shown for the related Mo-Si-B system in [190]. Due to the high energies that arise during milling impurities in the form of grinding tool abrasions can arise. For SS tools no significant amounts of Fe (< 2 at. %) were measured by means of EDS analysis. Though tungsten carbide is a very hard and brittle material, contamination of the mechanically alloyed powders with flaked particles of tungsten carbide (visible by the WC reflexes in Figure 5.13 and white spots in Figure 5.16 b) were detected. The quantity of tungsten carbide impurities was evaluated on the basis of high contrast SEM micrographs using the software Image J software. A concentration of 0.2 % for the low energy milling process (150 rpm) and 0.45 % for the higher rotational speed of 200 rpm were measured after 20 h of milling. After 50 h of milling the concentration of WC impurities increases to 0.75 % for 150 rpm and 1.75 % for 200 rpm. The presence of WC impurities can lead to undesirable effects, such as crack initiation due to notch effect which then leads to deterioration of the mechanical properties [191]. This fact reduces the attractiveness of the WC grinding material substantially as the process needs to run at lower rotational speed to avoid high concentrations of WC impurities. This lowers the cost-effectiveness of the process, as a reduction in speed is accompanied by an increase in process time. For SS grinding tools even after 50 h of milling the impurity concentration of Fe is below 0.2 at. % and according to the phase diagram provided by [189], low concentrations of Fe, as observed in the MA V-9Si-13B powder material, are solved in the V lattice resulting in a contribution to the solid solution hardening of the material. No further effects of Fe impurities on the V-Si-B system are known from the literature.

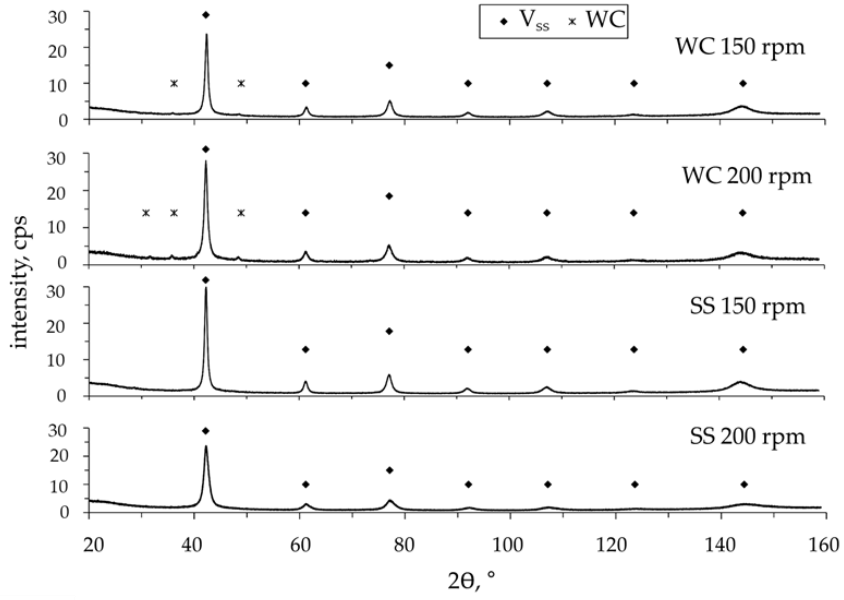

Figure 5.13: XRD data of V-9Si-13B after 20 h of milling with different rotational speed and various grinding aggregates (SS- stainless steel, WC – tungsten carbide).

Next to impurities resulting from the grinding material, oxygen contamination is an important aspect. For all samples no significantly increased oxygen contamination (< 12000 ppm) was observed. The respective values are shown in Table A.3. A significantly increased oxygen

concentration is known to cause hardening and even embrittlement, resulting in pronounced trans granular failure of the material [192]. The effect of an increased oxygen concentration of 24307 ppm ± 1022 ppm on the milling behavior of a V-9Si-13B alloy (WC grinding tools) is shown in Figure 5.14. The milling process is dominated by fracturing and only little cold welding. The increased embrittlement of the material, which results from softening of the grain boundaries occupied by the impurities, leads to a drastic particle size reduction. At the same time, the very fine particles collide and stick together by forming agglomerates due to the increased effect of the van-der-Waals forces. After 20 h off milling the material provide a particle/agglomerate size of d_{50} = 11.5 µm and a sphericity of Ψ = 0.24, which indicates very irregular shaped material. Due to the above mentioned points the material was discarded.

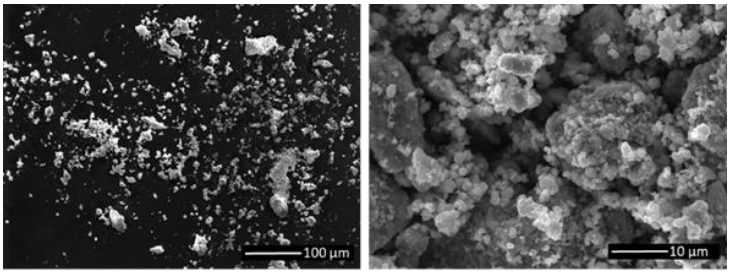

Figure 5.14: Agglomerated V-9Si-13B powder material after 20 h of MA with a high amount of oxygen contamination (24307 ± 1022 ppm).

Table 5.9: Particle size d_{50} and oxygen concentration of V-9Si-13B depending on the milling time.

milling duration V-9Si-13B, h	particle size d_{50}, µm			
	SS		WC	
	150 rpm	200 rpm	150 rpm	200 rpm
1	26.4	36.8	26.35	35.6
2	38.15	37.75	28.25	30.1
5	36.4	39.5	28.61	49.5
10	37.6	36.0	39.9	33.4
20	40.3	27.4	31.7	22.1
50	27.6	29.1	-	15.23

Particle sizes (d_{50}) with respect to the rotational speed as well as the grinding tools are presented in Table 5.9. The particle size (d_{50}) of the powder mixture before MA was determined with 29.7 µm. Growth of the particles is observed during the initial state of the MA process (up to 2 h - 5 h) for all V-9Si-13B alloys investigated here, which is in good agreement with the previously studied V-Si alloys. Similar behavior was reported for the structural related Mo-Si-B powders [66]. The increase of particle size in the initial state can be explained by a significant deformation of the particles, accompanied by the formation of fresh surfaces and subsequent cold welding processes, specifically of the ductile V particles [71]. A lower kinetic energy, as it arises with a rotational speed of 150 rpm, extends the duration of welding processes (correlation with particle size) up to a maximum of 20 h for MA of a V-9Si-13B powder alloy using SS grinding tools. WC grinding

tools operating at a rotational speed of 150 rpm lead to welding processes up to 10 h of milling. After the initial state cold working and strain hardening processes occur until an equilibrium state of fracturing and subsequent welding is reached and homogenization of the particle size emerges. Brittle behavior of the powder particles, i.e. due to a higher amount of Si, is accompanied by a further reduction of the particle size below the initial powder particle size as it can be seen for the investigated alloys shown in Table 5.9. The same trend was observed for milling of a Mo-Si-B alloy with a Si concentration of 8 at. % [45]. Figure 5.15 shows the powder morphology using the example of the V-9Si-13B powders after 20 h of milling with SS or WC aggregates at a rotational speed of 200 rpm.

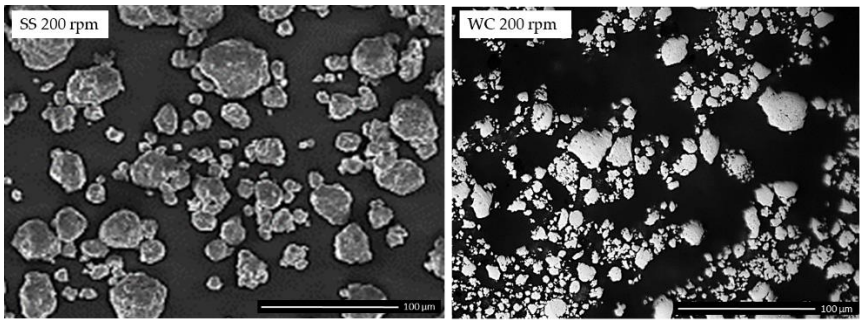

Figure 5.15: V-9Si-13B powder particles after 20 h of MA with a rotational speed of 200 rpm and different grinding aggregates (SS – stainless steel, WC – tungsten carbide).

In comparison to more globular particles (sphericity Ψ: 0.89) arising from milling with SS balls the powders milled with WC tools are more irregularly shaped (sphericity Ψ = 0.6). Furthermore, the particles milled with SS tools offer a narrower particle size distribution. V-9Si-13B SS powder after 20 h of milling offer a FWHM (Full Width at Half Maximum of frequency particle size distribution) of 45 µm (range: ~ 5 µm – 50 µm) while the V-9Si-13B WC powder particles provide a FWHM of 80 µm (range: ~ 10 µm – 90 µm) and thus, indicates a larger variation in particle size distribution next to the above mentioned lower sphericity.

To evaluate the grinding behavior of the V-9Si-13B alloy with respect to the different grinding tools and operating parameters the semi-empiric model introduced in Chapter 5.1.2 was applied. Based on these relations, Figure 5.16 illustrates the behavior of V-9Si-13B powders depending on the grinding tools and energy transfer applied for the respective milling time. Figure 5.16 demonstrates the dominance of cold welding processes indicated by negative K_P values after 1 h of milling in the experiments performed at 200 rpm for SS and WC MA powders as well as for the trial using a rotational speed of 150 rpm with WC grinding tools. SS tool process at 150 rpm reveals a tendency for comminution after 1 h of milling, which can be attributed to the initial state of MA process, where fracturing and welding processes are still in high competition as the properties of the individual powder material is still dominating. The relatively high amount of elemental Si at this state promotes comminution but at the same time many reactive surfaces compete for welding. With ongoing MA process and formation of the typical lamellar structure the material behavior becomes more consistent. The slope of the graphs is determined by the grindability k (Table 5.10), characterizing the powder behavior in analogy to the particle size. At the initial

process state, k did not vary significantly between the individual trials, which can be seen by the shallow slope of the graphs. After 10 h of milling, where the state of homogenization is further advanced, K_P tends to values around 0, which means that the size reduction and particle growth processes are almost in an equilibrium state (Table 5.10). This trend still continues up to 20 h of process time for all V-9Si-13B powders, but alloys milled with 200 rpm exhibit a slight trend for comminution evoked by the higher energy input. With ongoing process time from 20 h up to 50 h the individual process development for the trials conducted with SS tools remains in a similar trend. However, for V-9Si-13B (150 rpm) milled with WC tools a strong consolidation of the material was observed after 50 h of milling while the V-9Si-13B alloy milled with WC tools (200 rpm) established a bimodal particle size distribution. Due to the large variance of particle size, the grindabilty k (respectively the comminution rate K_P) determined in Table 5.10 for alloy V-9Si-13B (WC 200 rpm 50 h) is not representative. A light microscopy image, provided in Figure A.5 in the appendix, shows the large variance of particle sizes in the bimodal V-9Si-13B system.

Table 5.10: Grindability k and comminution rate K_P of V-9Si-13B powders on the milling time and the impact energy influenced by the rotational speed of the planetary ball mill and grinding aggregates (SS - stainless steel, WC – tungsten carbide).

duration of milling time	V-9Si-13B							
	SS, 150 rpm		SS, 200 rpm		WC, 150 rpm		WC, 200 rpm	
	k, hit/mJ	K_P, -	k, hit/mJ	K_P, -	k, hit/mJ	K_P, -	k, hit/mJ	K_P, -
1	-0.009	-0.107	-0.007	-0.136	0.007	0.084	-0.015	-0.312
10	-0.011	-0.131	-0.001	-0.006	-0.010	-0.115	-0.007	-0.138
20	-0.006	-0.070	0.009	0.194	-0.002	-0.025	0.008	0.179
50	-0.004	-0.050	0.013	0.262	-	-	(-0.009	-0.193)

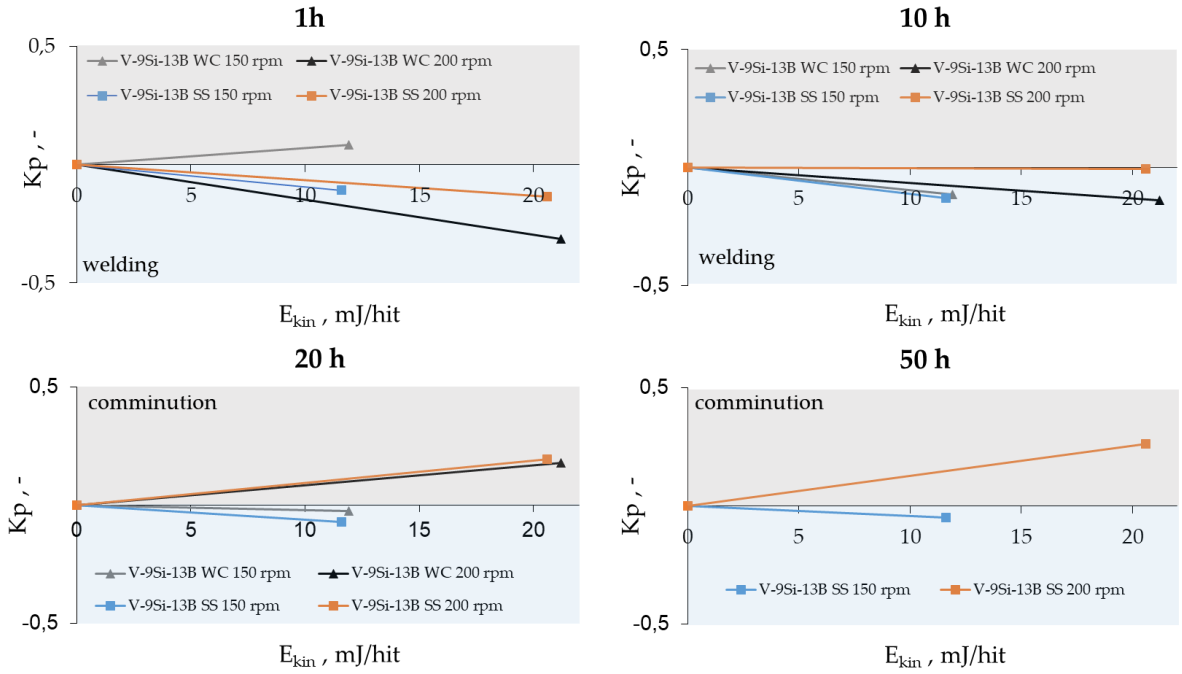

Figure 5.16: Comparison of the comminution/welding behavior of V-9Si-13B depending on the duration of milling and the impact energy.

Hardness

The evolution of the micro hardness with respect to the milling progress is presented in Figure 5.17. In all case studies the hardness seems to increase mainly during the first 20 h of MA and then the values remain nearly constant up to 50 h of milling. In general, the hardening mechanisms that may occur during the MA process are work hardening, grain refinement (Hall-Petch hardening), dispersion hardening and solid solution hardening as observed also in other powder materials [193]. The hardening by dispersed second phase particles, more precise silicide V_3Si and V_5SiB_2 particles, will be revealed in the next chapter.

All these effects show a dependency on the milling duration as well as on the variation of the kinetic energy that is transferred from the milling balls to the powder particles (Table 5.7). Figure 5.17 a) clearly shows the effect of the used rotational speed concerning micro hardness evolution. The data of the powders treated at 150 rpm (blue and grey curves) show a significantly lower hardness in comparison to 200 rpm trials (orange and black curves). However, even if the difference in the kinetic energy using SS or WC balls seems to be quite small, i.e. 0.3 mJ/hit at 150 rpm and 0.6 mJ/hit at 200 rpm, the increased kinetic energy transferred by the WC balls results in higher hardness values (Figure 5.17 a)). The values are also in good agreement with the values obtained in earlier milling studies on binary V-Si material (Chapter 5.1.3). The consistency of the hardness values beyond milling times of 20 h can be explained by the homogenized state of the MA powders (Figures 5.12 and 5.13).

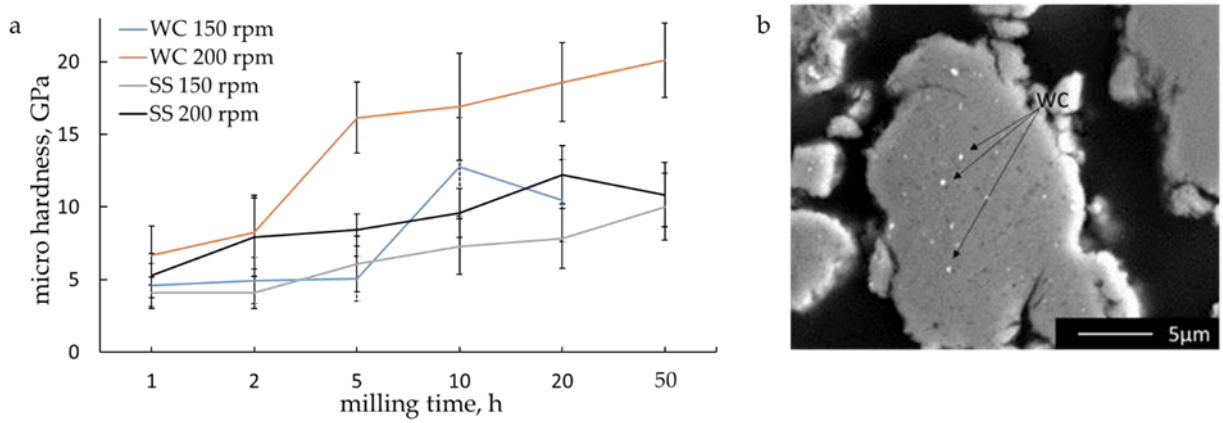

Figure 5.17: a) Micro hardness evolution (HV 0.01) of V-9Si-13B during the mechanical alloying process using different milling parameters (SS—stainless steel; WC—tungsten) and b) WC impurities in V-9Si-13B particles after MA of 20 h at 200 rpm.

This study leads to the conclusion that using grinding tools made of stainless steel is more beneficial for the investigated system. A basic criterion for this is powder texture. During the MA process, the powder material should be freely movable in the grinding vial, to promote homogenous distribution of the alloying elements [72], [193]. Powder material milled with tungsten carbide aggregates tends to consolidate earlier than the powders milled with stainless steel tools. Moreover, the relatively large and clearly visible WC impurities (white spots in Figure 5.17 b) may influence the material properties and their heterogeneous distribution within the powder material has a counterproductive effect on the reproducibility. The formation of Fe impurities when using SS tools is also not desired, but the atoms are finely distributed within the V_{ss}. Taking the concentrations and type of impurities into account, the product quality using SS tools seems to be higher. However, studies on minor Fe impurities in Mo-Si-B alloys proposed an enhanced oxidations performance due to an enhanced fluidity of the borosilica [194]. The effect of Fe in the V lattice is still unknown but the above mentioned approach might be useable for V-based alloys too.

Furthermore, to reach the target of homogenous pre-alloyed powder particles, the process also runs more economically using a rotational speed of 200 rpm since this leads to the reduction of process time. Based on this parameter study, a rotational speed of 200 rpm and SS grinding tools will be used for all further experiments.

5.2.2 Different V-Si-B powder materials manufactured via MA – milling behavior

V-12.5Si-25B (V_5SiB_2 phase)

To complete the investigation series, the ternary V_5SiB_2 phase was also manufactured by MA in addition to the single phases V_{ss} (nominal composition V-2Si) and V_3Si (nominal composition V-25Si) (shown in Chapter 5.1). For this purpose, grinding parameters defined in Chapter 5.2.1 were used (MA with 200 rpm, stainless steel grinding tools). Figure 5.18 a) – c) depicts the typical

microstructural evolution during MA, as it was observed to be in accordance to V-Si and V-9Si-13B powders. Starting from elemental V, Si and B powder (alloy composition V-12.5Si-25B), a solid solution is produced via MA due to the formation of increasingly finer lamellar structures up to microstructural homogenization (after 20 h of milling, Figure 5.18 b)). HT of the supersaturated V_{ss} phase (showing no remarkable reflexes for Si or B) at 1400 °C leads to nucleation and precipitation of silicide phases due to solid-solid-state reactions triggered by diffusion. XRD analysis data in Figure 5.18 d) exhibit the formation from single phase V_{ss} powder particles to multi-phase powder particles. After HT phases of the alloy V-12.5Si-25B are allocated to 92.3 vol. % V_5SiB_2 phase, 7.9 vol. % V_3Si phase and 4.2 vol. % V_{ss} (determined by means of Rietveld analysis, respective reflexes are highlighted in Figure 5.18 d).

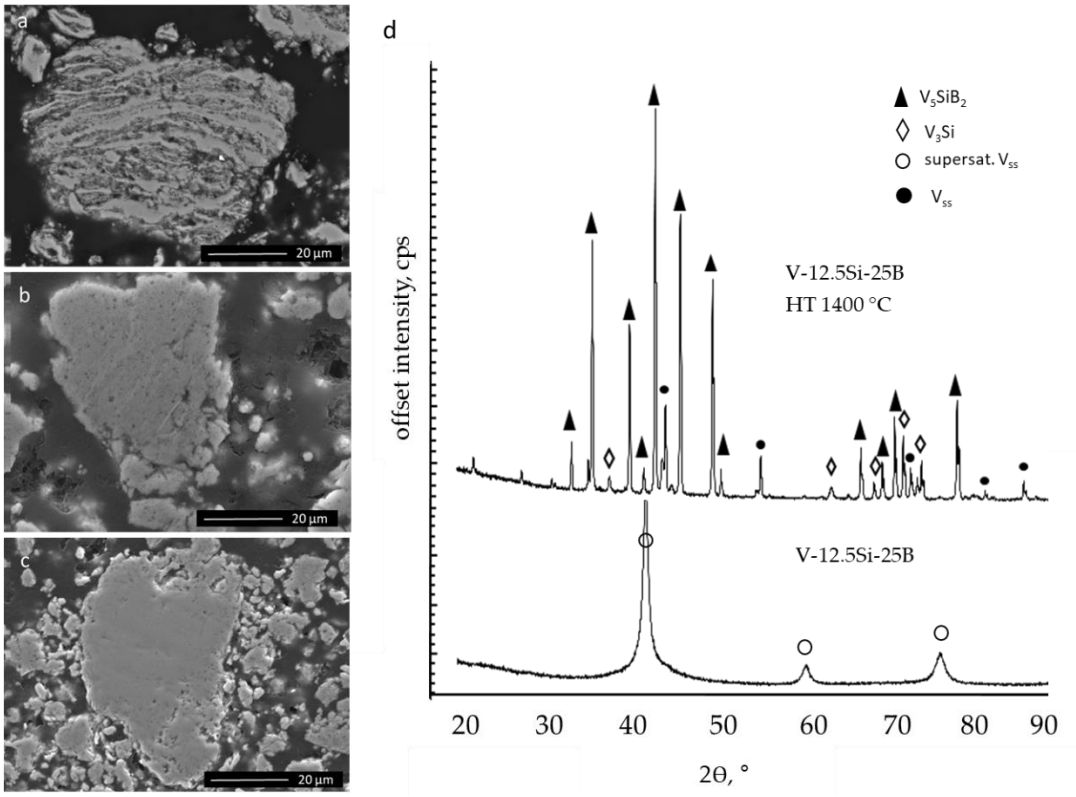

Figure 5.18: Microstructural evolution of V-12.5Si-25B powder particles during MA after a) 5 h, b) 20 h, c) after 20 h MA and HT of 1400 °C and d) XRD pattern of a 20 h MA V-12.5Si-25B before and after heat treatment of 1400 °C for 1 h.

Figure 5.18 c depicts the corresponding microstructure which exhibits with 92.3 vol. % of the V_5SiB_2 phase an almost single phase material, similar results are shown in [15] for a PM consolidated V-12.5Si.25B alloy. Particle size distribution increases with increasing milling time from d_{50} of 32.76 µm (20 h MA) to 84.3 µm for 20 h of MA. The reason for such significant particle growth must be given by the high amount of B as in contrary an increased amount of the brittle component Si suppresses particle growth as already demonstrated for the V-15Si and V-25Si alloys. The oxygen concentration shows values of maximum 14063 ppm before and 20326 ppm after heat treatment, which has been shown in previous studies to be uncritical with regard to an

influence on the milling behavior. The hardness of the powder particles increases from values of 6.53 ± 1.8 GPa (5 h MA) due to solid solution formation, as well as grain refinement and work hardening to 8.87 ± 2.8 GPa after 20 h of milling and results in a significant increase of hardness after HT at 1400 °C for the nearly single phase V_5SiB_2 powder particles (92.3 vol. % V_5SiB_2 phase). The hardness of the heat treated V-12.5Si-25B powder particles was determined with 25.32 ± 4.9 GPa which is in good agreement with micro hardness values of ~ 20 GPa measured in the V_5SiB_2 phase of a consolidated V-9Si-13B alloy [11].

Table 5.11: Properties of V-12.5Si-25B (V_5SiB_2 phase) powders.

	V-12.5Si-25B (V_5SiB_2, T2)		
MA	5 h	20 h	20 h + HT 1400 °C
d_{50}, µm	32.76	84.27	83.43
oxygen concentration, ppm	14063.1 ± 328	11657.7 ± 876	20326 ± 926
hardness HV 0.01, GPa	6.53 ± 1.8	8.87 ± 2.8	25.32 ± 4.9

V-9Si-5B and V-9Si-13B

Hasemann et al. [53] published results on microstructural investigations of ternary eutectic refractory Me-Si-B (Me = Mo, V) alloys. While Mo-Si-B alloys are well-investigated, only little is known about the neighboring V-Si-B system especially with regard to phase formation and phase equilibria. First results on investigations of a ternary V-Si-B eutectic were discussed in [53] and alloy V-9Si-5B was found to form a microstructure that offers next to small fields of a primary solidified V_{ss} phase and a binary V_{ss}-V_5SiB_2 eutectic large areas of ternary V_{ss}-V_3Si-V_5SiB_2 eutectic. It could be shown that the ternary eutectic involves phases with the same crystal structures as its Mo-Si-B neighbor system, more precisely the A2 structured V_{ss} phase and the two silicide phases having a A15 structure (V_3Si) and the $D8_1$ structure (V_5SiB_2) [53]. According to Hasemann the ternary eutectic provides the highest potential for excellent high temperature strength combined with good oxidation properties [195]. Following this approach, the MA and subsequent heat treatment of a V-9Si-5B alloy was investigated in this work as a ground state investigation for subsequent consolidation.

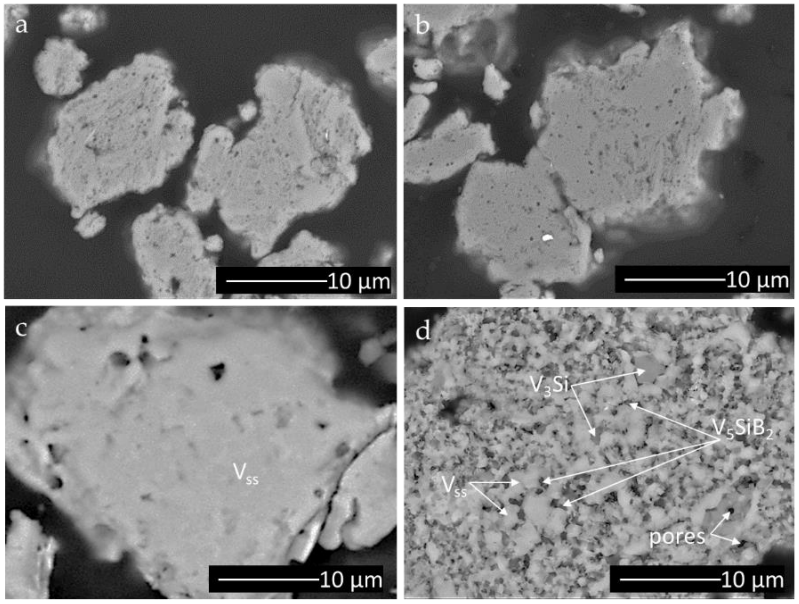

Figure 5.19: Milling progress of V-9Si-5B after a) 2 h of MA, b) 10 h of MA, c) 20 h of MA and d) 20 h MA and heat treatment at 1400 °C (1h).

Figure 5.19 shows the microstructural evolution during MA of the V-9Si-5B powder composition following the previously described trend for V-Si and V-Si-B material by forming the typical lamellar structure in the initial state of MA. After 20 h of milling a homogenized single phase microstructure arises (Figure 5.19 c and 5.20).

The powder material was proven to be free flowing up to a milling duration of 30 h. Viscosity of the powder increases with increasing milling time but powder caking (also called powder clumping) of the material was not observed up to 50 h of milling. The respective oxygen concentration and particle size are in good agreement with the powder material from previous studies of this chapter and can be found in Table A.4 and Table A.5 in the Appendix. Figure 5.18 d) depicts a SEM image of an annealed V-9Si-5B powder particle. The resulting microstructure (highlighted in Figure 5.19 d), phases determined by EDS and XRD analysis) consists of a larger amount of the V_{ss} phase which surrounds the homogenously distributed V_3Si and V_5SiB_2 phases. The XRD plot of the powder sample offers next to the above mentioned phases still unknown reflexes which cannot be clearly assigned (Figure 5.20). This can be the result of contamination during milling or annealing, i.e. with oxygen, which promotes the formation of complex oxides [11], [89]. In general, one of the predominant problems for powder metallurgy manufactured materials is contamination of the material due to a significantly larger surface area of the powders compared to the surface area of bulk material [196]. Contamination can arise from a variety of sources, such as process control agents (PCA), oxygen from the ambient environment or abrasion of the grinding tools. As it is an inherent characteristic of the PM process, controlling of the contamination during milling or subsequent consolidation is difficult but can be limited by controlling and optimizing the parameters of its possible sources [196].

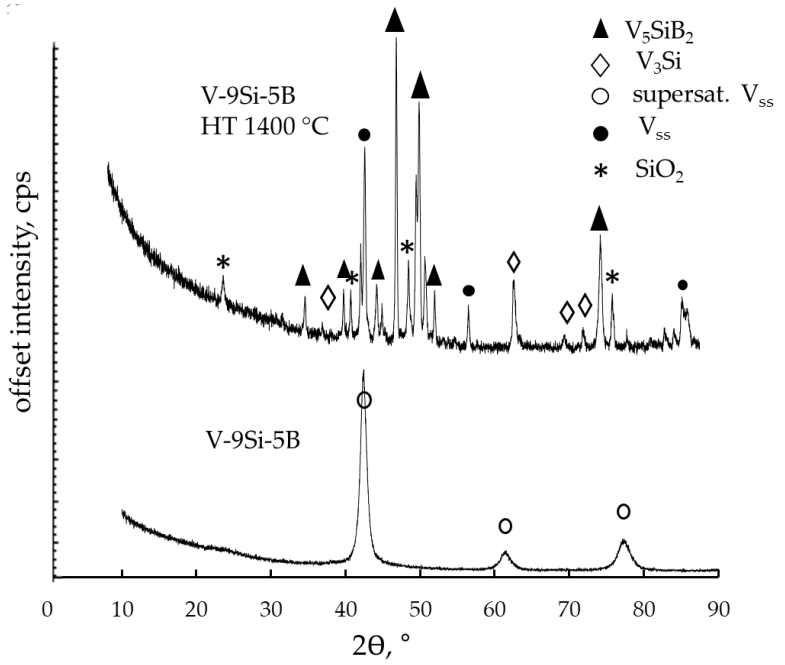

Figure 5.20: XRD analysis of a V-9Si-5B alloy in the as-milled state and after HT showing reflexes of V_{ss}, V_3Si and V_5SiB_2 phase [11].

The milling progress of V-9Si-13B powders as well of powder in the heat treated state are depicted in Figure 5.21. The V-9Si-13B powder material after heat treatment, shown in Figure 5.21 d), was provided by the author of [33]. Results of investigations on the heat treated V-9Si-13B powder material were taken from the appropriate paper. As the MA process of the V-9Si-13B alloy (SS tools, 200 rpm) was in detail described in the previous section, only a description of the heat-treated sample is given here. After annealing at 1400 °C the powder reveals a three-phase V-V_3Si-V_5SiB_2 microstructure. The annealed powder particles show fine and homogenously distributed silicide particles (the dark grey phases in Figure 5.21 d) embedded in a V_{ss} matrix (light grey phase). The black spots are SiO_2 particles, which indicate a non-optimized deoxidation during sintering in Ar [11].

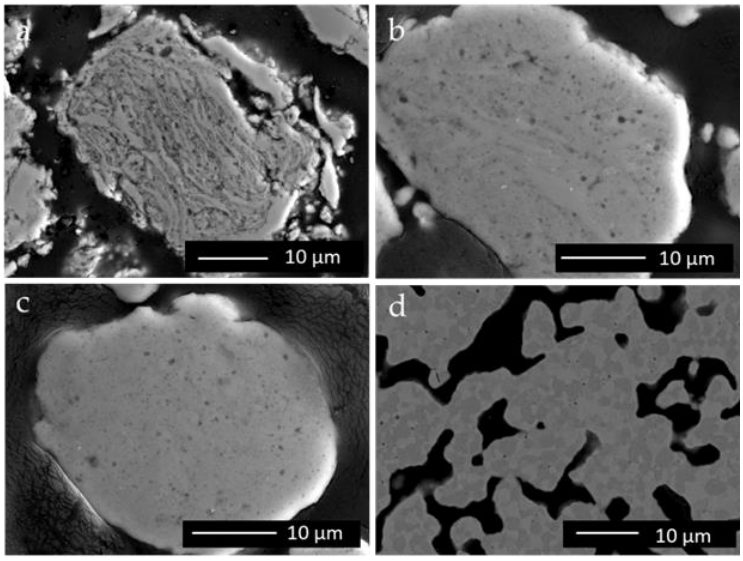

Fig 5.21: Milling progress of V-9Si-13B after a) 2 h of MaA, b) 10 h of MA, c) 20 h of MA and d) 20 h MA and heat treatment at 1500 °C (1 h).

Furthermore, powder material with the alloy composition of V-9Si-19B was investigated. After 15 h of milling strong consolidation of the powder material occurs and prevented the possibility of further investigations of the powder material. As such strong solidification limits the homogenization during grinding process the powder material of alloy V-9Si-19B was not further investigated in this work. However, some results are presented in the appendix (Figure A.2, Table A.4 – A.6).

The hardness (after 20 h of MA) of the V-9Si-5B powder material in comparison to the hardness of V-9Si-13B powders in the as-milled state (light grey columns) as well as after annealing (dark grey columns) is illustrated in Figure 5.21. Hardness for remaining milling durations can be found in Table A.6. Both, V-9Si-5B and V-9Si-13B, as-milled supersaturated powder materials offer an increased hardness in comparison to the saturated V_{ss}. V-9Si-5B has a hardness of 8.29 ± 1.5 GPa while the higher amount of B in the alloy composition V-9Si-13B leads to an increased hardness of 12.21 ± 2.5. This may be attributed to the larger amount of B atoms dissolved in the host lattice resulting in increased solid solution hardening. After heat treatment the V-9Si-5B powder material depicts a remarkable increase of hardness due to the significant influence of the precipitated silicide phases. For alloy V-9Si-13B no significant change in hardness was observed due to the heat treatment. According to the alloy composition a higher amount of precipitated V_5SiB_2 phase in comparison to V-9Si-5B should emerge. As a result, however, an increased hardness is expected, as the phase fractions in the powders were determined with ~ 55 – 60 vol. % silicides (optical measurement by separation of the grey values). This should exceed the hardness values determined for previous solid solution hardening and result in a hardness increasing effect as the individual hardness of the respective silicide phases V_3Si and V_5SiB_2 is significantly higher than the hardness of the V_{ss} phase, shown in Figure 5.22.

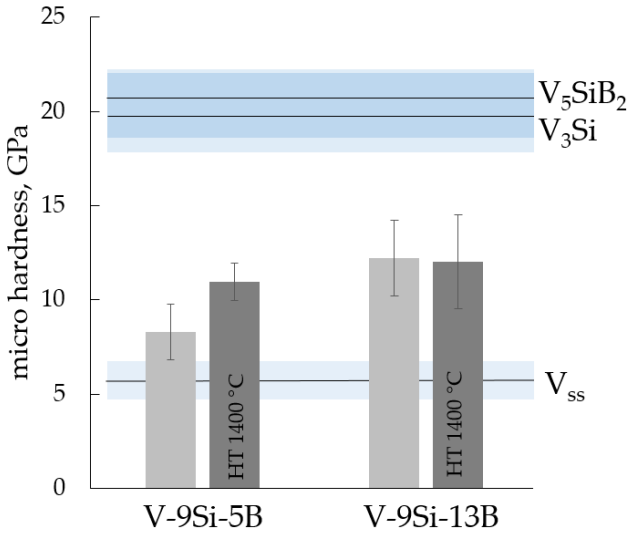

Figure 5.22: Micro hardness HV 0.01 of V-9Si-5B and V-9Si-13B supersaturated powder particles after 20 h of MA and heat treatment of 1400 °C in comparison to MA and HT (1400 °C) powder material as well as hardness values of the single V_{ss}, V_3Si and V_5SiB_2 phase from [11].

For consolidation, as discussed in the next chapter, alloy V-9Si-5B was chosen. Both alloys, V-9Si-5B as well as V-9Si-13B, offered a good grinding performance which is important for successful MA and homogenously alloyed powder particles and finally for the properties of the targeted compacts. The decision is mainly based on the fact that V-9Si-5B was found to be a near-eutectic alloy composition as in the following gas atomization of this alloy as well as additive manufacturing will be conducted.

6 Results and discussion: Consolidated V-Si(-B) material

Content of this chapter is the evaluation of two innovative approaches for consolidation of pre-alloyed V-9Si-5B powder material. The microstructural development from the respective processes as well as the resulting mechanical properties are discussed in order to derive microstructure-property relationships for this class of material.

6.1 Microstructure of sintered pre-alloyed V-Si(-B) powder material

Sintering of the pre-alloyed V-15Si and V-9Si-5B powder material was conducted by means of field assisted sintering technology (FAST). The powder material was pre-alloyed by MA in a previous process step which was already described in Chapter 5.

6.1.1 V-15Si

The microstructure of the PM V-15Si alloy produced by PM process is shown in Figure 6.1 a). A clear separation between the light grey V_{ss} phase and the darker colored V_3Si phase could be observed by SEM (BSE mode) in combination with EDS measurement. XRD analysis, shown in Figure 6.1 b), confirms the allocation of the two observed phases. The phase distribution, identified via SEM images, appears with a fraction of 49 vol. % V_{ss} phase and 51 vol. % V_3Si phase and thus provides a balanced distribution, as it is expected from this composition according to binary V-Si phase diagram [187]. As typical for materials consolidated via FAST, microstructure components are very fine and both, V_{ss} and V_3Si phase, are homogenously distributed due to the uniform distribution of the alloying elements within the individual powder particles. The V_3Si phase assumes a matrix-like character and the V_{ss} fractions appear as imbedded islands. A similar microstructural evolution was already shown in Figure 5.9 (Chapter 5.1.4) for the annealed V-15Si powder material.

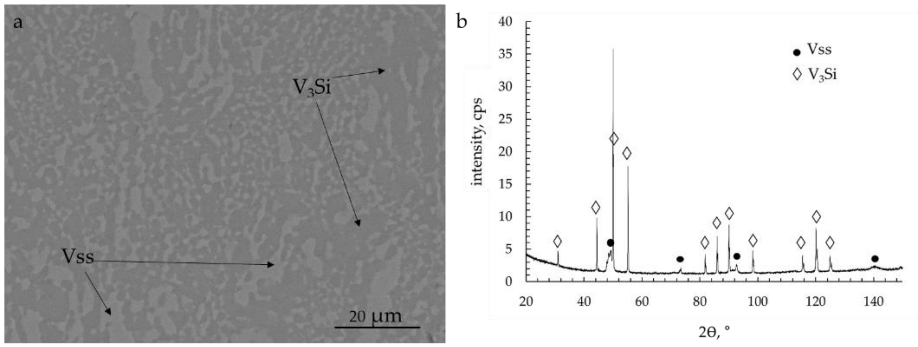

Figure 6.1: a) SEM microstructure of FAST V-15Si and b) XRD analysis of FAST V-15Si.

Properties such as density, chemical composition and oxygen concentration etc. can be found in Table 6.1. The oxygen concentration of PM alloys strongly depends on the purity of the elemental components and the parameters used during sintering process [66], [197]. In analogy to [198], no significant change of the oxygen concentration during the PM consolidation process compared to the powder state (oxygen concentration V-15Si powder after MA: 6143.7 ppm ± 211 ppm) could be achieved, although the handling and sintering were strictly performed under inert gas atmosphere.

Table 6.1: Properties of V-15Si manufactured via FAST.

properties V-15Si	values	
density	5.83 g/cm3	
porosity	0.2 – 0.4 %	
chemical composition	V: 85.29 at. %	Si: 14.13 at. %
impurities	< 1 at. %	
phase distribution	V_{ss}: 49 vol. %	V_3Si: 51 vol. %
Si in V_{ss}	5.75 at. % ± 0.4 at. %	
oxygen concentration	5867 ppm ± 572 ppm	

6.1.2 V-9Si-5B

Figure 6.2 a) shows that sintering of the mechanically alloyed powder particles via FAST led to a three-phase V_{ss}-V_3Si-V_5SiB_2 microstructure as expected from the previous investigations of the annealed powder materials in Chapter 5. The presence of the respective phases was proven by X-ray diffraction analysis (Figure 6.2 b)) as well as EBSD analysis, which is depicted in Figure 6.3 a). The alloy exhibits a volume fraction of 51.8 vol. % V_{ss} phase, 25.4 vol. % V_3Si phase and 22.7 vol. % V_5SiB_2 phase. The resulting microstructure shows a V_{ss} network which coexists with an interwoven microstructure of the silicide phases according to [11], [15].

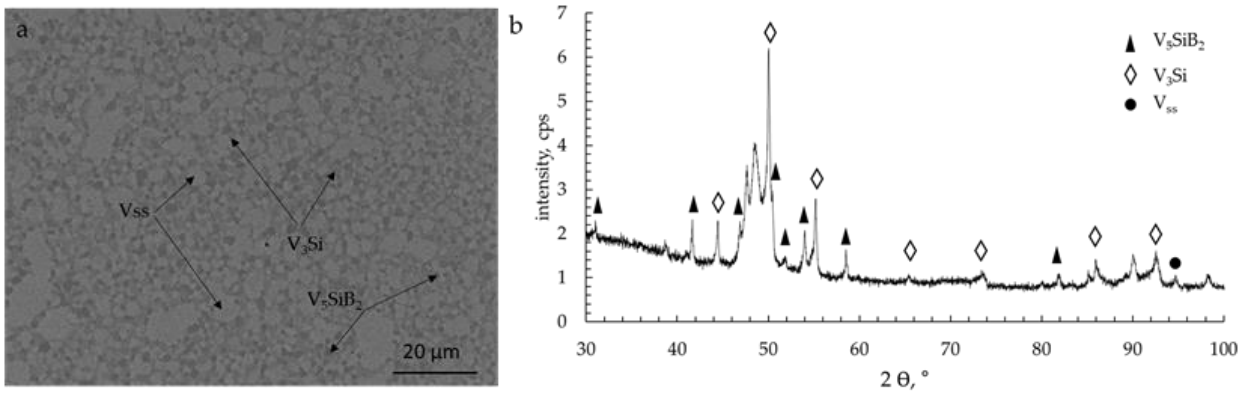

Figure 6.2: a) SEM microstructure of FAST V-9Si-5B and b) XRD analysis of FAST V9Si-15B.

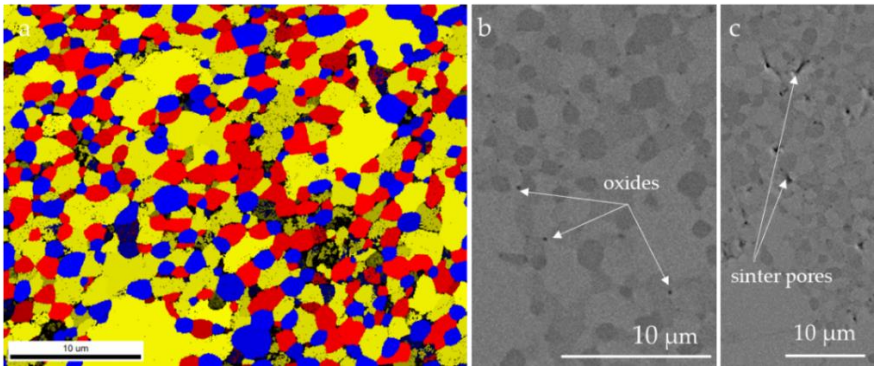

Figure 6.3: a) EBSD analysis of FAST V-9Si-5B with color coded phases (V_{ss}: yellow, V_3Si: red, V_5SiB_2: blue, b) formed oxides after consolidation via FAST and c) residual pores within the material after sintering.

The microstructural comparison with the FAST V-9Si-13B alloy from [11] reveals similarities in the morphology as well as in the length of the scale of the silicides which are measured with diameters of 1.5 µm ± 0.5 µm for both alloys, respectively. Due to similar crystal structures of the occurring phases this type of microstructure is also well-known for the related Mo_{ss}-Mo_3Si-Mo_5SiB_2 alloys [47], [199], [200].

Additional material properties of the FAST V-9Si-5B alloy are provided in Table 6.2. Some unidentified reflexes still emerge from the X-ray diffraction data which are shown in Figure 6.2 b). Consistently, the EBDS analysis also shows some black areas where phase indexing according to the Kikuchi pattern was not possible. It must therefore be assumed that there is at least one additional phase that cannot be assigned at this time. This may be attributed to the inherently high oxygen concentration of the V-based material promoting the formation of complex oxides during consolidation. Next to unidentified oxides the formation of finely distributed nearly equiaxed SiO_2 particles were observed (shown in Figure 6.3 b)), which mainly decorate the grain and phase boundaries. Similar observations were reported for sintered structural similar Mo-Si-B alloys [66], [201] and V-9Si-13B powder material [11]. In addition to an improvement of strength by oxide particles, as it is known from the ODS effect, an undesirable oxide formation can also lead to a deterioration of the mechanical properties due to the induced occurrence of grain boundary sliding a homologous temperature above ~ 0.5 T_m [202]. In contrast to oxides, residual porosity after sintering is shown in Figure 6.3 c) and is present at a level of 0.3 – 0.5 vol. %.

Table 6.2: Properties of a V-9Si-5B alloy manufactured via FAST (chemical composition evaluated by wet chemical analysis).

properties V-9Si-5B	values		
density	5.83 g/cm^3		
porosity	0.3 – 0.5 %		
chemical composition	V: 85.78 at. %	Si: 9.14 at. %	B: 5.07 at. %
impurities	< 1 at. %		
phase distribution	V_{ss}: 51.8 vol. %	V_3Si: 25.4 vol. %	V_5SiB_2: 22.7 vol. %
Si in V_{ss} phase	5.13 at. % ± 0.6 at. %		
oxygen concentration	6583 ppm ± 476 ppm		

6.2 Microstructure of additive manufactured pre-alloyed V-Si(-B) powder material

6.2.1 Processability of mechanically alloyed V-Si(-B) powder material

The demands on the powder material used for additive manufacturing (AM) are considerably higher than the requirements placed on powders for consolidation via FAST. While next to a homogenously distribution of the elements and good compressibility is important for sintering, the particle size and flowability of the powder material are particularly important for AM, in addition to the homogenous distribution of the elements [203]. Processing of the powders was conducted at Fraunhofer Institute for Laser Technology ILT, Aachen, Germany using Laser-Direct Energy Depostion (L-DED) as a method for AM. The parameters used for the L-DED process are provided in Chapter 3.2.2. The particle size requirements of 45 - 120 µm for AM processing could be well adjusted by sieving. The maximum size of the particles is defined by the laser beam diameter as well as the influence on the flowability of the material which varies in dependency on the particle size and typically decreases with increasing particle size [203], [204]. Figure 6.4 gives an overview of the resulting AM builds using mechanically alloyed powder material for AM processing (L-DED). For both alloys, V-15 Si (Figure 6.4 a) - c)) and V-9Si-5B (Figure 6.4 d), e)) cracked and delaminated or highly roughened surfaces were observed. A conducted height profile measurement of the V-9Si-5B specimen (Figure 6.4 d)) reveals a highly irregular surface structure with peaks and valleys of a maximum of 614.7 nm in topographical height.

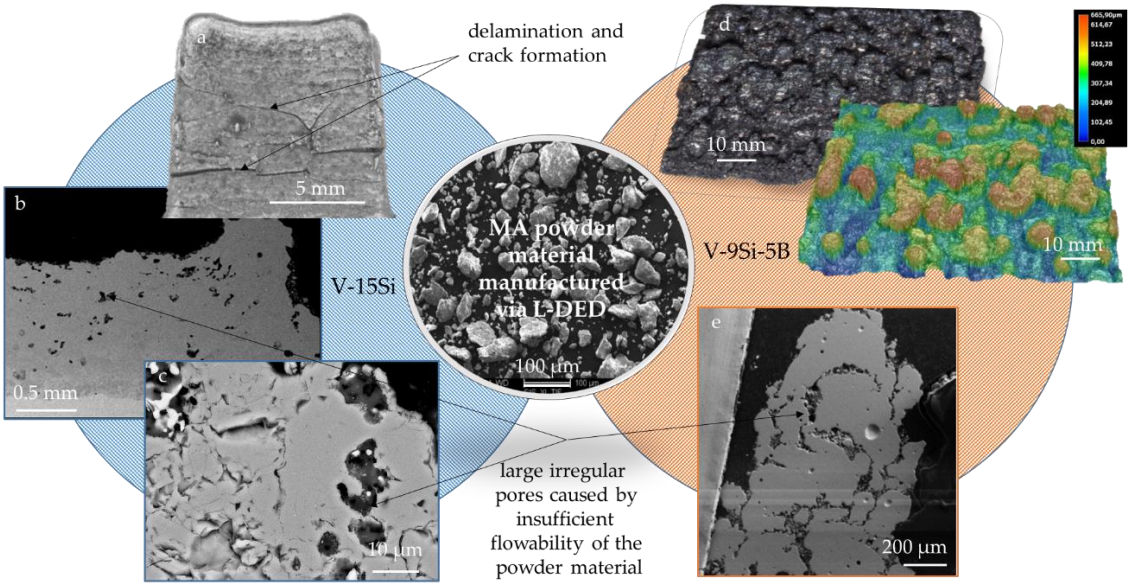

Figure 6.4: Overview of additively manufactured compacts from MA powder material: imperfections and pore formation lead to an insufficient quality of the consolidated a-c) V-15Si and d, e) V-9Si-5B alloy.

The corresponding cross-section of the consolidated material provides a discontinuous, porous, and fragile structure (Figure 6.4 e)). The reason can be assigned to insufficient powder flow properties due to the irregular powder morphology and impurities from the mechanical alloying process. This results in a rupture of the material flow and powder separation as well as composition deviations [204]. To overcome this problem, gas-atomized powder material was chosen for additive manufacturing as it typically provides a highly spherical morphology resulting in improved flow properties.

6.2.2 Processability of gas atomized V-9Si-5B powder material

As previously shown, the initial material is an important part of AM processing to accomplish dense and crack free builds. The flowability of the powder particles, which typically increases with increasing sphericity of the particles, plays an important role here [72]. To this end, powder atomization is the most widespread technology for the mass production of metal powders for AM and yields a spherical shape, high cleanliness, and a fine and homogeneous microstructure [205]. Atomization of vanadium silicides is hardly common at this time, the high melting point and the reactive nature of vanadium are limiting factors. The atomization process was conducted by Nanoval GmbH & Co. KG, Berlin, Germany, described in more detail in Chapter 3.1.2. Compared to mechanical alloying, where impurities are added by milling media abrasion or oxygen contamination, during gas atomization (GA) process the material is faced different process steps where elemental losses, by evaporation of the individual alloy components, can occur. During processing detection of possible losses is difficult so that the residual feedstock, i.e. the solidified melt, and the powder material was analyzed concerning their chemical composition (see Table 6.3). The melting point of V-9Si-5B was measured during processing in the melt using a platinum-

rhodium thermocouple and is about 1630 °C – 1650 °C (information provided by Nanoval GmbH & Co. KG).

Table 6.3: Chemical composition of the solidified residual melt from the gas atomization process, the powder material after GA and the AM compact specimen.

	chemical composition [at.%]			
element	nom. composition	residual melt	GA powder	L-DED build
V	86	85.5 ± 0.78	86.2 ± 1.0	85.6 ± 0.96
Si	9	9.2 ± 0.23	8.9 ± 0.05	9.3 ± 0.07
B	5	5.3 ± 0.14	4.9 ± 0.03	5.1 ± 0.02

The residual solidified melt shows no significant deviations from the nominal composition (V–9Si–5B) and remains with 9.2 ± 0.23 at. % Si and 5.3 ± 0.14 at. % B. The GA powder material does not undergo significant elemental losses, which means that the element concentration remains nearly constant with 8.9 ± 0.05 at. % Si and 4.9 ± 0.03 at. % B. Figure 6.5 a) shows the microstructure of the feedstock after processing, solidified in the crucible at ambient temperature. It is formed by primarily solidified V_{ss} dendrites surrounded by fine ternary eutectic structures consisting of V_{ss} (bright phase), V_3Si (medium grey) and the needle-shaped V_5SiB_2 phase (dark grey). A more detailed view on the microstructure is shown in Figure 6.5 d), where the V_{ss} phase can be identified as the matrix phase of the ternary eutectic structure. An equivalent microstructural evolution with respect to both the formation and the size of the solidified phases of an as-cast V–9Si–5B alloy was reported by Hasemann in [16]. The white spots were identified (by EDS analysis) as zirconium oxide particles, which are a contamination from the crucible material. Contaminations like these are critical, as the particles are relatively large and may have an influence on the resulting material properties, e.g. due to crack initiation from notch tips [191]. The trend for atomization of V-Si-B material may therefore be developed towards crucible-free atomization using Electrode Induction Melting Inert Gas Atomization (EIGA), which is the state-of-the-art process for the high-quality spherical powder production for AM, especially tailored for production of high-purity, reactive and refractory metal powders [206]. Currently, the challenge is still to produce the pre-alloyed electrode for this kind of material.

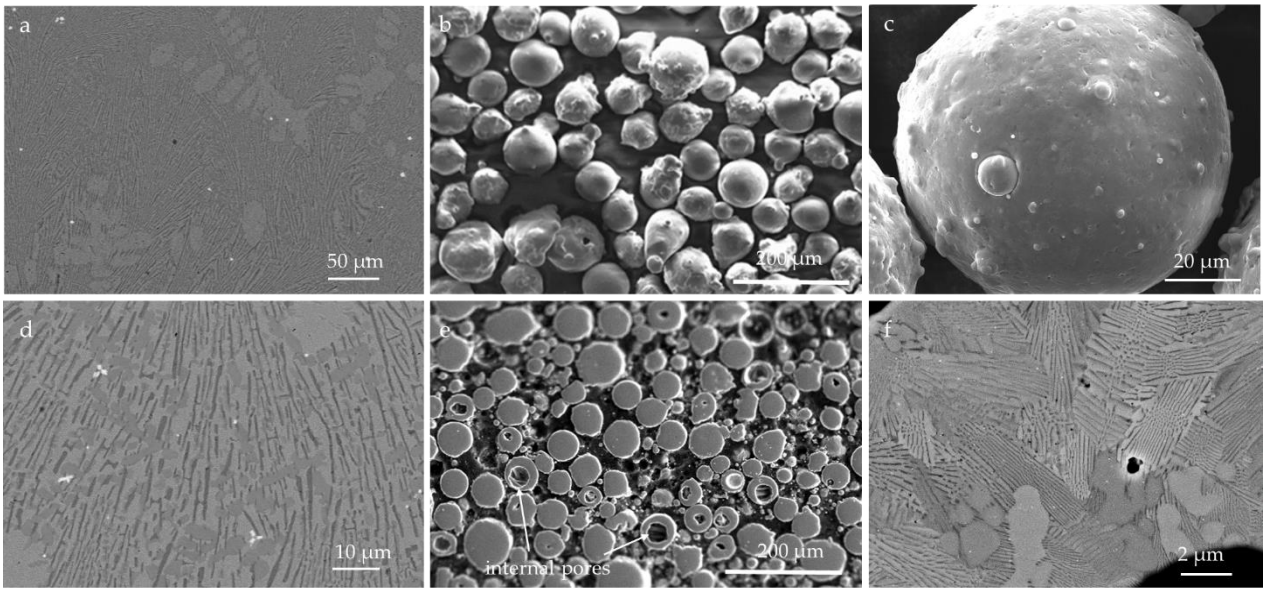

Figure 6.5: a) and d): Microstructure of the solidified feedstock with primarily solidified V_{ss} dendrites and ternary eutectic V_{ss}–V_3Si–V_5SiB_2 regions, b) and c): morphology of the V–9Si–5B powder material after GA, e) and f): cross-section and microstructure of mounted V–9Si–5B powder material.

Table 6.4: Powder properties of gas atomized V-9Si-5B powder material.

properties	values		
phase distribution	V_{ss}: 65.7 vol.%	V_3Si: 17.4 vol. %	V_5SiB_2: 16.9 vol. %
oxygen content	640 ppm ± 57 ppm		
particle size	d_{10}: 39.3 µm	d_{50}: 71.6 µm	d_{90}: 103.7 µm
sphericity ψ	0.94		
flowability ffc	10.4 (free flowing)		
hardness HV 0.01	6.98 GPa ± 0.37 GPa		

The powder particles emerging from the GA process are depicted in Figure 6.5 b), c) and e). In comparison to MA powder particles they show a smooth surface, a predominant spherical shape ($\psi = 0.94$) and a low tendency for agglomeration or formation of satellites. Typical sphericity values determined for V-Si alloys (presented in Chapter 5, Table 5.2) are between $\psi = 0.36$ – $\psi = 0.62$ after 20 h of milling. The argon gas flow during processing protects the pre-alloyed material from oxidation reactions and benefits the solidification rate, whereby the increased solidification rate lowers the time window for possible evaporation and leads to particles that do not become too large and reveal a narrow size distribution [207]. The average particle size was measured with $d_{50} = 71.6$ µm, the d_{10} and the d_{90} were determined with 39.3 µm and 103.7 µm, respectively. Spherical powder material provides better flow properties than irregularly formed powders as they are less prone to cling each other [205]. The flowability coefficient ffc for the GA powder particles, measured by means of shear cell testing [114], was determined with a value of ffc = 10.4 which indicates a free flowing behavior [72], [113], [171].

The solidified V-9Si-5B powder particles (out of the GA process) show a microstructure that consists of primarily solidified V_{ss} phases next to fine ternary eutectic V_{ss}–V_3Si–V_5SiB_2 structures (Figure 6.5 f)). Considering that both the residual feedstock and the GA powder material have the same chemical composition, the microstructural differences must arise due to different cooling conditions. With regard to the ternary V–Si–B phase diagram it turns out, that the solidification of the residual melt in the crucible under ambient conditions seems to be closer to the equilibrium state while the fast cooling during GA process results in much finer microstructural constituents.

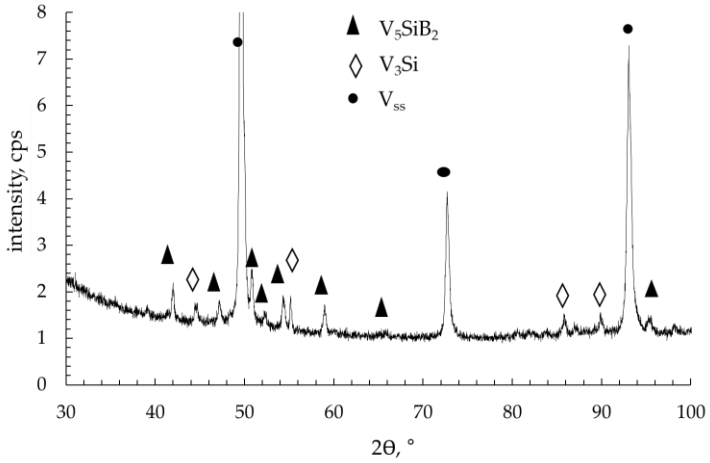

Figure 6.6: XRD analysis of GA V-9S--5B powder material.

X-ray diffraction measurements (Figure 6.6) and subsequent Rietveld refinement confirm the presence of the phases V_{ss}, V_3Si and V_5SiB_2. The volume fraction of the respective phases is presented in Table 6.4. All reflexes of the XRD analysis were allocated to the V_{ss}, V_3Si and V_5SiB_2 phase, which indicates a very pure powder material without remarkable impurities (compare also with Table 6.3). The large Zr particles found in the residual melt can be also found in the GA powder material, but in a smaller volume fraction. Hardness HV 0.1 of the GA V-9Si-5B powder reaches a value of 6.98 GPa ± 0.37 GPa and is thus approx. 15 % lower than that of MA powders and even 35 % lower as compared to the MA powder material after heat treatment (see also Table A.6). The relatively large difference can be attributed to the combination of the individual hardening mechanisms that occur during mechanical alloying (see Chapter 4.1.1). The oxygen concentration of the powders was measured with a value of 640 ppm ± 57 ppm (see Table 6.4) and shows significantly lower values compared to the MA powder material (~ 5000 ppm – 8000 ppm). As oxygen contamination is an inherent characteristic of the PM process, powder production via gas atomization process offers the tremendous advantage of low oxygen concentrations [196].

6.2.3 Microstructure of gas atomized V-9Si-5B powder material consolidated via L-DED

V-9Si-5B compacts manufactured via L-DED are shown in Figure 6.7. The chemical composition after AM with 9.3 ± 0.07 at. % Si and 5.1 ± 0.02 at. % B still fits the nominal composition of the initial alloy and is provided next to other properties of the consolidated material in Table 6.5. Using the GA powder material leads to an almost even and uniform surface of the AM build.

Some irregularities can be observed due to the adherence of sprinkles during processing. Despite this defects the specimen shows a uniform and plain topography and reveals the typical layered structure emerging due to the layer-wise cladding of the material [203], [208]. The cross section reveals a crack-free specimen with a density of approx. 95.7 %. Irregularly distributed pores in the size of up to approx. 100 µm are visible. As the porosity is still quite high, a possible origin of this problem is discussed in the following.

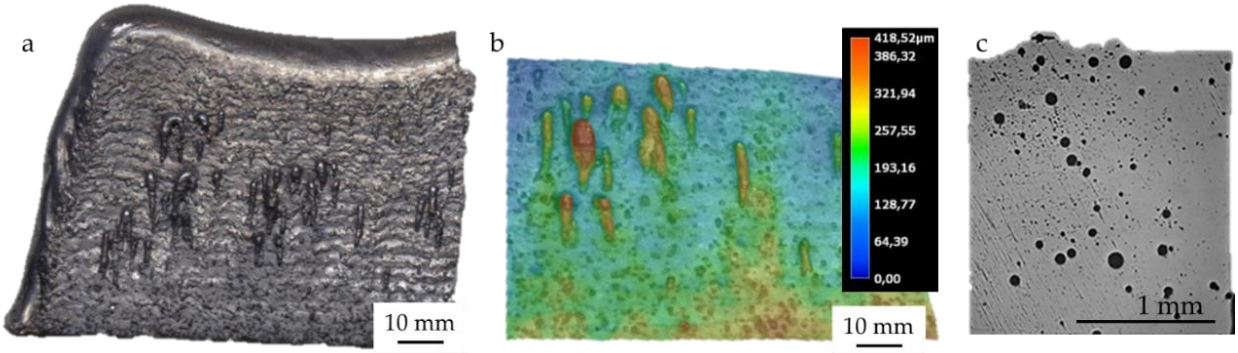

Figure 6.7: Morphology after consolidation of gas atomized pre-alloyed V-9Si-5B powder material via L-DED showing a) a macroscopic image, b) AFM surface profile and c) a cross section with residual porosity from AM processing.

Table 6.5: Properties of L-DED V-9Si-5B compacts

properties V-9Si-5B	values
density	5.94 g/cm^3 (archimedian principle)
porosity	5 – 8 %
chemical composition	V: 85.78 at. % Si: 9.14 at. % B: 5.07 at. %
impurities	< 1 at. %
phase distribution	V_{ss}: 66.6 vol. % V_3Si: 16.4 vol. % V_5SiB_2: 17.0 vol. %
oxygen concentration	756 ppm ± 73 ppm

Figure 6.7 c) and 6.8 a) show that the pores are regularly shaped. This indicates an origin from gas porosity and less from a lack of fusion which typically evolves with irregularly shaped pores between the layer boundaries [19], as it was shown for the builds emerging from the MA powder in Figure 6.4. The residual porosity inside the powder particles (Figure 6.5 e)) will affect the porosity in the AM build. According to [209], the porosity level of powder material is usually much lower than the porosity level of the deposited samples. Furthermore, the deposit often shows larger sized pores in comparison to the powder material. Agglomerated gas bubbles and coalescence in the melt pool can be possible reasons. However, the porosity inside the powder material cannot fully account for the gas porosity found in the deposited samples [209]. It was also found that the porosity is related to the powder feed rate and shielding gas flow. The powder stream can trap the delivered shielding gas, which becomes entrained into the melt pool. A reduction of porosity can therefore be achieved by using powder that is free of porosity, together with a process that does not require a high shielding gas flow rate. Regardless of the settings, a convective effect, known as Marangoni flow, will contribute to the formation of pores by retaining entrapped gas bubbles in the melt pool [209]. Studies focusing on these aspects have to be done in more detail in the future for this novel processing route of V–Si–B materials.

By means of X-ray diffraction analysis the phases of the L-DED V-9Si-5B alloy can be assigned to 66.6 vol. % V_{ss} phase, 16.4 vol. % V_3Si phase and 17.0 vol. % V_5SiB_2 phase. The corresponding plot is provided in Figure A.3 in the Appendix and exhibits in agreement with Figure 6.6 (GA V-9Si-5B powder) a clear assignment of all reflexes to the phases V_{ss}, V_3Si and V_5SiB_2. The oxygen concentration after AM was determined with 756 ppm ± 73 ppm and exhibits only a slight increase of 18 % compared to the atomized powder particles. A strong increase of the oxygen concentration due to processing was also not determined for the comparative FAST process, but the oxygen values are inherently higher as a result of the PM process route. This is also reflected by the respective XRD analyses, shown in Figure 6.2 b). While the AM V-9Si-5B alloy led to a high purity material with clearly assignable phases, the XRD analysis for the sintered V-9Si-5B material revealed some reflexes that could not be clearly assigned. This phenomenon occurred mainly for the V_{ss} phase, while the silicides V_3Si and V_5SiB_2 could be clearly identified. The reason for this can be seen in the high reactivity of pure vanadium, respectively, the V_{ss} phase with interstitial oxygen induced by the mechanical alloying process, which promotes the formation of complex oxides [210]. This assumption can be confirmed by means of density-functional theory (DFT) calculations, provided by Dr. Rachid Stefan Touzani from Otto-von-Guericke-University, Magdeburg, Germany. It was shown that the reactivity of V for forming oxides, such as V_2O_5 is thermodynamically more favorable than the oxidation of V_5SiB_2 and V_3Si (see Figure 6.8 a)). Similar results were reported in [211]. Another effect can be seen in the processing via FAST. The high pressure and temperature loading during manufacturing lead to stresses and dislocation pile-up within the solid solution phase, causing the indexing of the phases to become difficult. In addition, due to solid solution formation lattice distortion occurs and leads to a shift of the respective reflexes.

A direct comparison visualizing the deviation of XRD data of both alloys is shown in Figure 6.8 b) and depicts unidentified reflexes for the sintered (FAST V-9Si-5B) alloy at a scanning range of 47° - 50° as well low and broadened reflexes for the V_{ss} phase due to deformation of the crystallographic structure by processing via FAST. Furthermore, due to the smaller atomic size of Si which is dissolved within the V lattice a shift towards higher 2θ angles emerges. In comparison to the L-DED V-9Si-5B alloy which shows a reflex that can be clearly assigned to the V_{ss} phase.

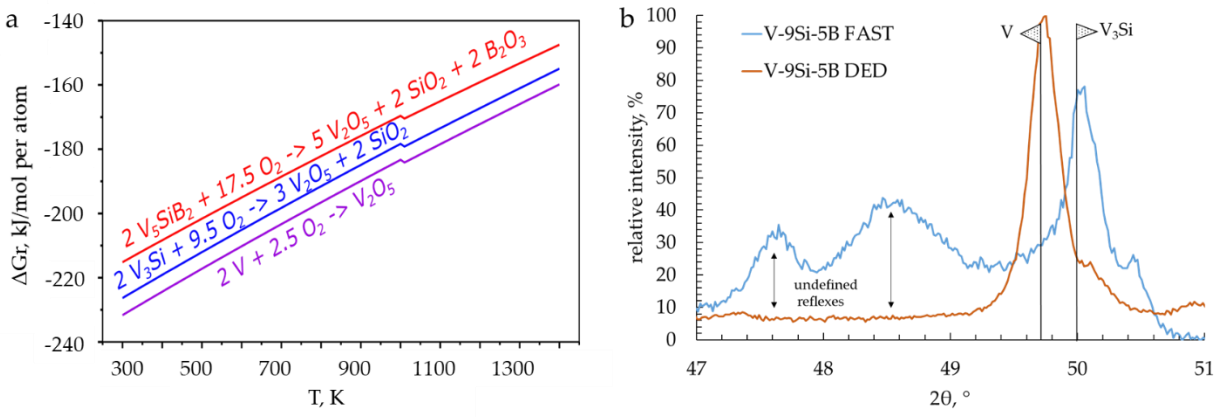

Figure 6.8: a) DFT calculations showing that the reactivity V, V_3Si and V_5SiB_2 using the example of V_2O_5 formation and b) comparison of XRD data from FAST and L-DED V-9S-5B visualizing process induced microstructural differences.

Microstructural evolution of the L-DED build with its typical layering structure is shown in Figure 6.9, showing the deposition layers bonded by distinct fusion lines (red dotted line). One section of the interface is presented in Figure 6.9 b), which occurs as a coarser grained film of the primary V_{ss} in connection to V_5SiB_2 and V_3Si phases (in the center of Figure 6.9 b), red dotted line) in comparison to the surrounding extreme fine and homogenous eutectic V_{ss}-V_3Si-V_5SiB_2 microstructures. This effect arises due to the sequential reheating induced by the layer-wise build-up which causes the samples to pass an in-situ heat treatment during the process [208]. This in-situ heat treatment is further enhanced by a high pre-heating temperature of the base plate, as this reduces the temperature gradient and leads to a more extended heat influence. The microstructure after heat treatment, shown in Figure 6.11, confirms this claim, as a coarser microstructure was observed due to annealing.

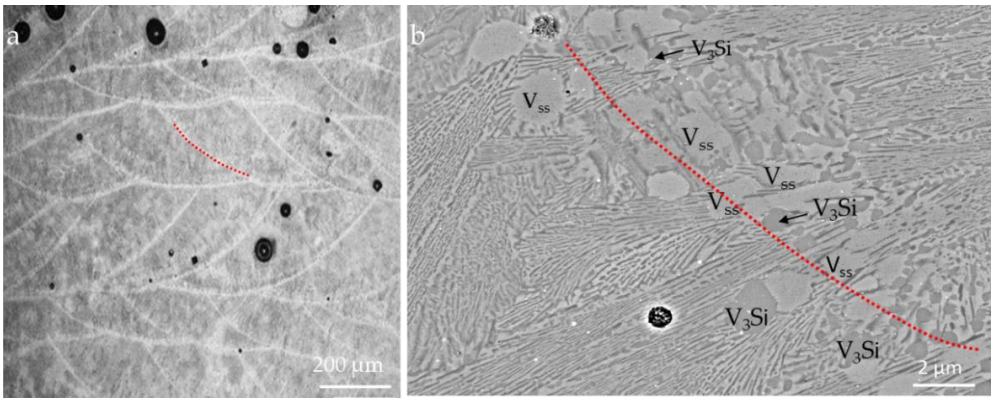

Figure 6.9: V-9Si-5B L-DED build with a) distinct zones from the layer-wise laser cladding process and regular formed pores, b) a section of the solid–liquid interface (red dotted line) and its surrounding primary V_{ss} phases, followed by fine eutectic areas.

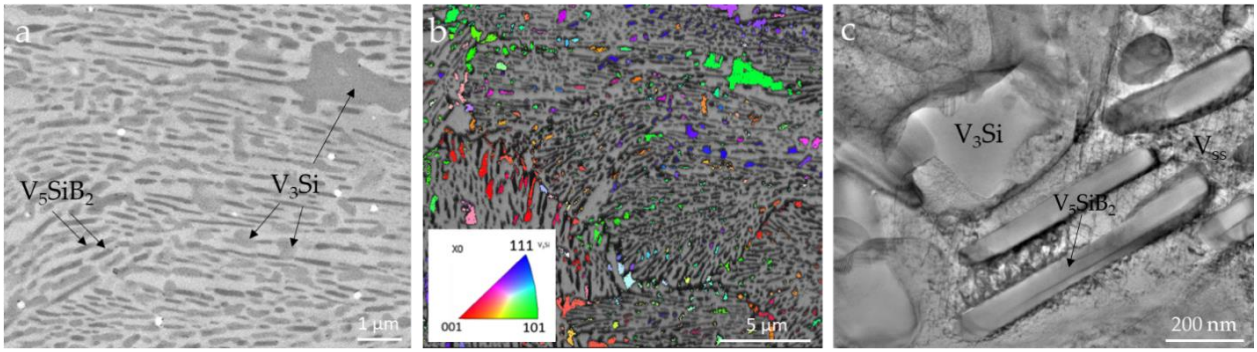

Figure 6.10: a) V-9Si-5B microstructure of the fine grained binary V_{ss}-V_5SiB_2 and ternary V_{ss}-V_3Si-V_5SiB_2 eutectic regions, b) EBSD orientation map showing the color coded orientation of V_3Si phase and c) STEM bright field image of the eutectic microstructure showing V_{ss} matrix phase with visible dislocations as well as V_3Si and V_5SiB_2 phases.

A higher magnification of the ternary eutectic structure besides the melt pool interface can be found in Figure 6.10 a). All three phases (V_{ss}, V_5SiB_2 and V_3Si) can be clearly identified. For a better differentiation of the two intermetallic phases within the fine eutectic structure, Figure 6.10 b)

shows the randomly orientated V_3Si phase in an EBSD orientation map. While the V_5SiB_2 phase typically shows a needle-like morphology that of the V_3Si phase is rather irregularly, which can be seen more clearly in the STEM BF image in Figure 6.10 c). The V_{ss} phase appears as matrix phase of the ternary eutectic structure, which is beneficial concerning the low temperature mechanical properties i.e. room temperature plasticity. Similar findings regarding microstructural evolution for the ternary V_{ss}-V_3Si-V_5SiB_2 eutectic section of an IM V-9Si-5B alloy were reported in [16], [56]. In contrast to the solid–liquid interface of each track, where the re-melting of the surface affects the cooling conditions by forming a coarser grained microstructure in these areas (Figure 6.9 b)), the microstructure within the individual layers shows no primarily solidified V_{ss} phase. This suggests a significant microstructural imbalance. To proof the stability of the microstructure, a heat treatment of the AM specimen at 1400 °C for 10 h was conducted under argon atmosphere. After heat treatment the distinct zones (coarser grained composite bond, fine eutectics) homogenize and turn into a microstructure consisting of a V_{ss} matrix with equally and homogenously distributed V_5SiB_2 and V_3Si phases, which are mainly connected to each other (Figure 6.11 a)). Phases are allocated to approximately 54 % of the V_{ss} phase (colored in green in Figure 6.11 b), 30 % of the V_3Si phase (red) as well as 16 % of the V_5SiB_2 phase (yellow). Compared to the as-built state the amount of the V_3Si phase is increased by 45 % at the expense of a reduction of the V_{ss} phase by 19 %. Because of high cooling rates during manufacturing via AM, a significantly supersaturated V_{ss} phase will form. The decreased solubility of silicon in the V_{ss} phase at lower temperatures, which is known from the binary V-Si phase diagram [1], will lead to a reduced concentration of Si in the V_{ss} during heat treatment resulting in the shift of phase fractions. No significant change of the volume fraction was observed for the V_5SiB_2 phase.

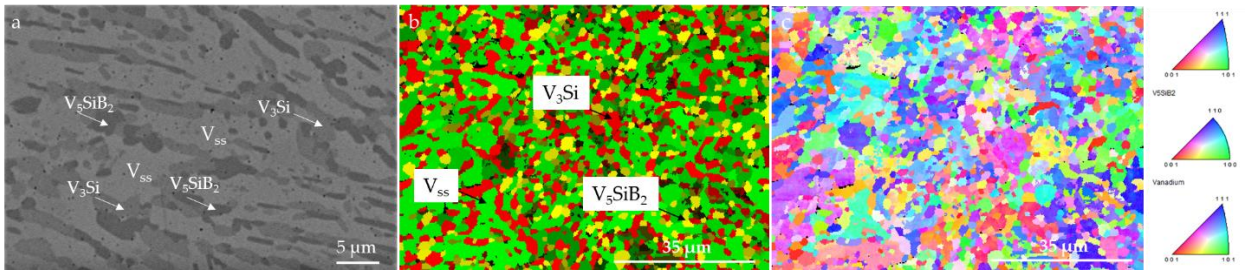

Figure 6.11: a) L-DED V–9Si–5B build with V_{ss} matrix with equally distributed V_3Si and V_5SiB_2 phases after heat treatment of 1400 °C for 10 h, b) EBSD image showing the color-coded V_{ss} (green), V_3Si (red) and V_5SiB_2 (yellow) phases and c) EBSD orientation map showing the grain structure of the material.

6.3 Mechanical properties of V-9Si-5B compacts

6.3.1 Hardness, compressive strength and plastic deformability of V-9Si-5B alloys

Determining hardness by means of a pyramidal indenter represents a simple method to obtain significant process-depending microstructural differences. Compared to the vanadium solid solution which primarily provides metallic bonds, the silicides reveal significantly higher hardness values evoked by a predominance of covalent and ionic bonds [85]. Thus, size,

distribution, and volume fraction of the individual phases will affect the hardness of the V-Si-B bulk material. For the present alloys, FAST V-9Si-5B and L-DED V-9Si-5B, hardness values of 12.9 GPa ± 2.8 GPa and 13.9 GPa ± 1.3 GPa were determined, which are in good agreement with the hardness values of the annealed V-9Si-5B powder particles presented in Chapter 5.2.2 (see also Table A.6: HV 0.1 = 10.97 GPa ± 0.99GPa). The determined hardness values match with the averaged values arising from the hardness of the respective phases (presented in Figure 5.16 in Chapter 5), as the microstructures consist approximately half of the solid solution phase and half of the silicide phases V_3Si and V_5SiB_2. In the as-built state, compared to the sintered V-9Si-5B specimen, the AM V-9Si-5B build shows a 12 % higher volume fraction of the V_{ss} phase, which exhibits the lowest hardness of the occurring phases (HV 0.1 V_{ss} ~ 7 GPa). However, as a result from processing the fine and homogenous eutectic microstructure of the DED build leads to an increased hardness and a minor standard deviation compared to the sintered specimens where the individual hardness of the coarser grained structure, especially the larger V_{ss} phases, has a higher influence on the hardness values of the alloy. Heat treatment of the AM specimen compensates for this effect and offers a slightly decreased hardness with a value of HV 0.1 = 13.1 GPa ± 1.9 GPa due to grain coarsening by factor 5 (shown in Figure 6.11). In comparison, data from literature of competing materials such as TiAl provide hardness values for Ti-43.5Al-4Nb-1Mo-0.1B of 3.8 GPa for a cast and 3.4 GPa for an AM alloy [212] as well as a hardness of 4.2 GPa for commercial CMSX-4 [213]. This results demonstrate the enormous strengthening effect by means of the silicide phases, which show at a minimum twice the hardness of the V_{ss} phase. Similar results on hardness of PM V-9Si-13B bulk material were reported in [11].

Table 6.6: Hardness values, compressive yield strength and plastic strain of a V-9Si-5B alloy manufactured via FAST and L-DED process

	HV 0.1, GPa	compressive $\sigma_{0.2}$, MPa			plastic strain under compression, %		
V-9Si-5B		RT	600 °C	900 °C	RT	600 °C	900 °C
FAST	12.9 ± 2.8	1521	1150	150	0	5.9	6.7
L-DED	13.9 ± 1.3	1948	1259	107	0.4	7.7	17.5

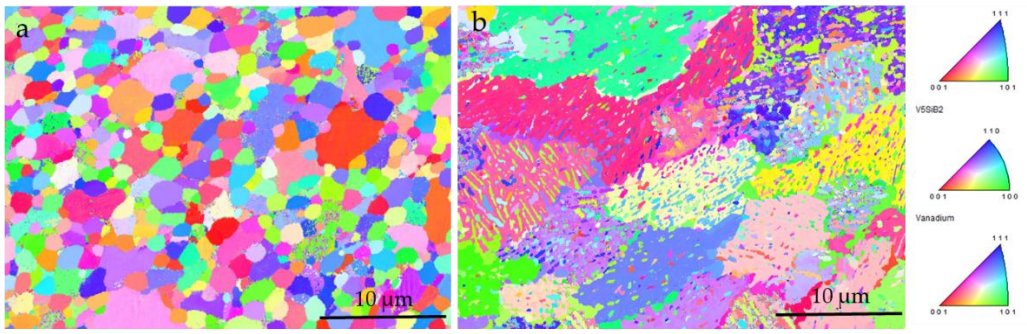

Figure 6.12: EBSD orientation map of the V-9Si-5B alloys showing the difference of grain size resulting from processing via a): FAST and b): L-DED.

Compressive strength at room temperature (RT) and elevated temperatures (600 °C and 900 °C) was determined by constant displacement tests at a nominal strain rate of 1 10^{-4} s^{-1} with uniaxial load. The results are presented in Table 6.6 and visualized in Figure 6.13 a) in terms of temperature-dependent stress. A visualization of the stress-strain curves can be found in the Appendix in Figure A.4.

Both materials, alloy FAST V-9Si-5B as well as L-DED V-9Si-5B, show the typical decrease of stress with increasing temperatures (Figure 6.13 a)) and fail in a brittle manner at RT and 600 °C while ductile behavior was observed at 900 °C, respectively. However, comparing both materials the L-DED V-9Si-5B alloy exhibits an improved strength under compressive load at RT. As shown in Figure 6.12, both alloys exhibit a fine grained microstructure whereas the FAST V-9Si-5B alloy reveals grain sizes below 10 µm (grains can be associated with the individual phases V_{ss}, V_3Si and V_5SiB_2), while the L-DED V-9Si-5B alloy has coarser eutectic cells providing a very fine V_{ss}-V_3Si-V_5SiB_2 structure. Accordingly, the FAST V-9Si-5B alloy benefits from solid solution hardening, as a Si concentration of 5.13 at. % was determined for the V_{ss} phase, in addition to strengthening by the Hall-Petch effect [148]. Solid solution hardening can be assumed for the L-DED material as well but due to its ultra-fine structure the Si concentration within the V_{ss} could not be determined exactly by EDS. The improved strength at RT for the L-DED V-9Si-5B probably can be attributed to the fine eutectic cells (phase size ≤ 1 µm), where the high density of phase boundaries, as an analogy to the grain boundaries, leads to an improved strength. Furthermore, the fine eutectic can be assumed as a V_3Si and V_5SiB_2 particle strengthened V_{ss} phase where the V_{ss} phase is the matrix phase and surrounds the individual sections of the silicides. As a result, due to particle hardening (Kelly-Fine / Orowan mechanism), a strengthening effect emerges in addition.

The impact of these strengthening mechanisms decreases with rising temperatures as described by Sun et al. in [214], where contribution from the Hall-Petch relationship was confirmed up to 600 °C. Contributions of particle strengthening are as well temperature dependent. Dislocation climbing starts from temperatures > 0.4 T_m [87], which is reached at about 660 °C for the V-9Si-5B alloy. These assumptions confirm the present experimental observations. At 600 °C the strength of the L-DED V-9Si-5B alloy is still slightly superior to the FAST V-9Si-5B material, but the strength for both alloys significantly drops with increasing temperatures as a result of the temperature dependence of the hardening mechanisms. At 900 °C, which represents a homologous temperature of the V-9Si-5B alloy of approximately 0.6 T_m, compressive behavior of both materials yields in drastically reduced strength due to increased grain boundary sliding [215] and activation of dislocation climb. A significantly enhanced plastic strain at 900 °C was observed for the L-DED V-9Si-5B alloy in comparison to the sintered material (see Table 6.6), which can be attributed to the higher amount of the weak V_{ss} phase providing an increased deformability at this temperature. At 600 °C both materials show a nearly similar behavior in terms of plasticity before failure with values of 5.9 % (FAST) and 7.7 % (L-DED), as the influence of dislocation climbing is low or no longer present at 600 °C and strengthening mechanisms as discussed in Chapter 4.1.1 operating instead [87]. However, notable room temperature plasticity as reported for cast V-Si-B alloys in [16] and [63] was not observed for the materials processed by FAST and L-DED.

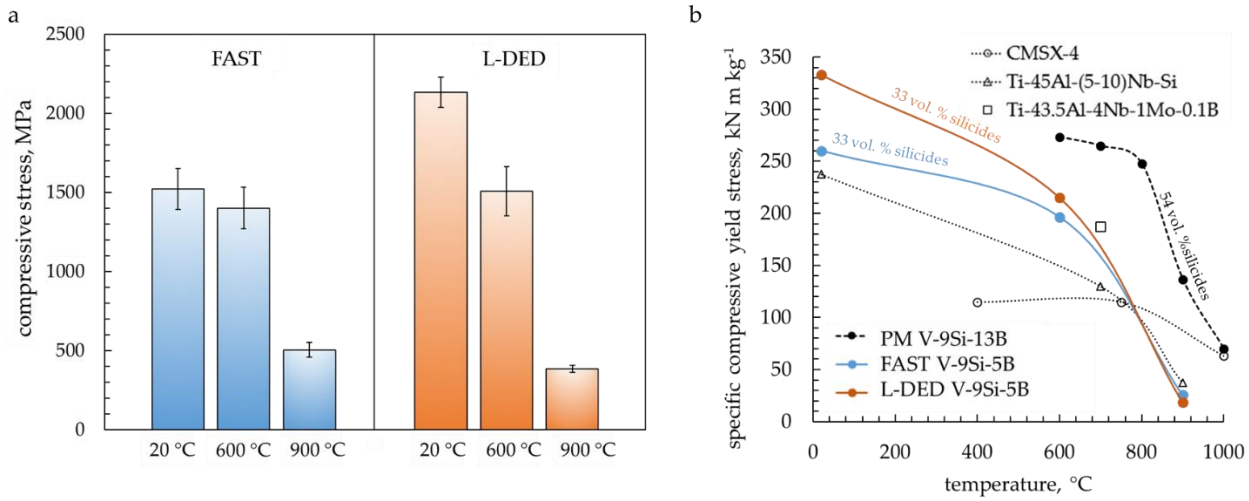

Figure 6.13: a) Temperature-dependent compressive stress at RT for alloy V-9Si-5B manufactured via FAST and L-DED process and b) specific yield stress of the alloys FAST/L-DED V-9Si-5B compared to data from literature: PM V-9Si-13B [11], CMSX-4 [216] and Ti-45Al-(5-10)Nb-Si [217] and measured values: Ti-43.5Al-4Nb-1Mo-0.1B.

The temperature-dependent specific compressive yield stresses of the present alloys compared to data available from literature are depicted in Figure 6.13 b). The PM manufactured V-9Si-13B alloy reveals a significant higher capability of sustaining compressive stress in comparison to the V-9Si-5B alloys which can be attributed to differences in phase distribution as a result of an increased B concentration of the V-9Si-13B alloy. This leads to a total increase in silicide phases by 21 vol %, whereby the amount of the very high strength V_5SiB_2 phase was even doubled [11], [15]. Except for the shift towards higher sustainable stresses, the curves of temperature-dependent specific yield stress of the PM V-9Si-13B and FAST V-9Si-5B alloy shown in Figure 6.13 b) follow the same trend as both alloys were processed via FAST and hence exhibit a comparable fine and homogenous microstructure. The strengthening effect of silicide phases is thus confirmed once again and can be considered for future microstructural design.

The material classes TiAl and CMSX-4 used for comparison show a decreased compressive strength from RT up to approximately 800 °C. While the flow stress of Ti-45Al-(5-10)Nb-Si at 900 °C aligns with those of the alloys investigated, the CMSX-4 material exhibits higher strength values in the range of 800 °C – 1000 °C as the absence of grain boundaries and the $\gamma/\gamma`$ microstructure are beneficial regarding the high temperature mechanical properties [218], [219]. It should be noted that the specific compressive yield strength of CMSX-4 at 1000 °C is also equal to that of alloy PM V-9Si-13B. For possible structural applications, however, the significant density difference of both materials (density V-9S-5B: 5.85 g/cm³ and density CMSX-4: 8.7 g/cm³) should be taken into account. Furthermore, it should be noted that for future alloy design the volume fraction of the silicide phases within the microstructure of the V-Si-B material act as a key parameter with regard to the expected mechanical properties.

6.3.2 Particle strengthening of L-DED V-9Si-5B

An additional option for improving the strength of V-Si-B materials is to use the approach of oxide dispersion strengthening (ODS), which is known to increase the strength in a wide temperature range and creep response of metallic materials [45], [220], [221]. Significant strengthening of structurally similar Mo-Si alloys by ZrO_2 and Y_2O_3 was presented in [220]. The oxide particles act as obstacles and the dislocations are pinned in form of particle-surrounding dislocation loops (Orowan mechanism), [80], [221].

To this end, the gas atomized V-9Si-5B powder material was used as base material. In a subsequent ball milling process Y_2O_3 particles (d_{50} = 45 nm) with an amount of 5.5 vol. % were added. The application of the ODS concept on AM alloys, like Fe- and Ti-Al-based alloys was already shown in [222], [223]. Y_2O_3-reinforced γ-TiAl is already demonstrated to provide improved hardness. The feasibility of printing Y_2O_3-reinforced V-Si-B material was carried out within the framework of this thesis with the support of the Fraunhofer ILT Aachen, Germany. It was shown that the modified powder could be processed into crack-free builds by means of additive manufacturing (L-DED). Figure 6.14 a) shows a homogenous distribution of the Y_2O_3 particles within the microstructure, whose identification was confirmed by EDS point measurement. The Y_2O_3 particles (bright white spots) were found within the ternary eutectic structure as well as incorporated in larger primarily solidified phases, such as the V_3Si phase which typically can be found in the melt pool boundary region (fusion line) of L-DED builds as described in Paragraph 6.2.3.

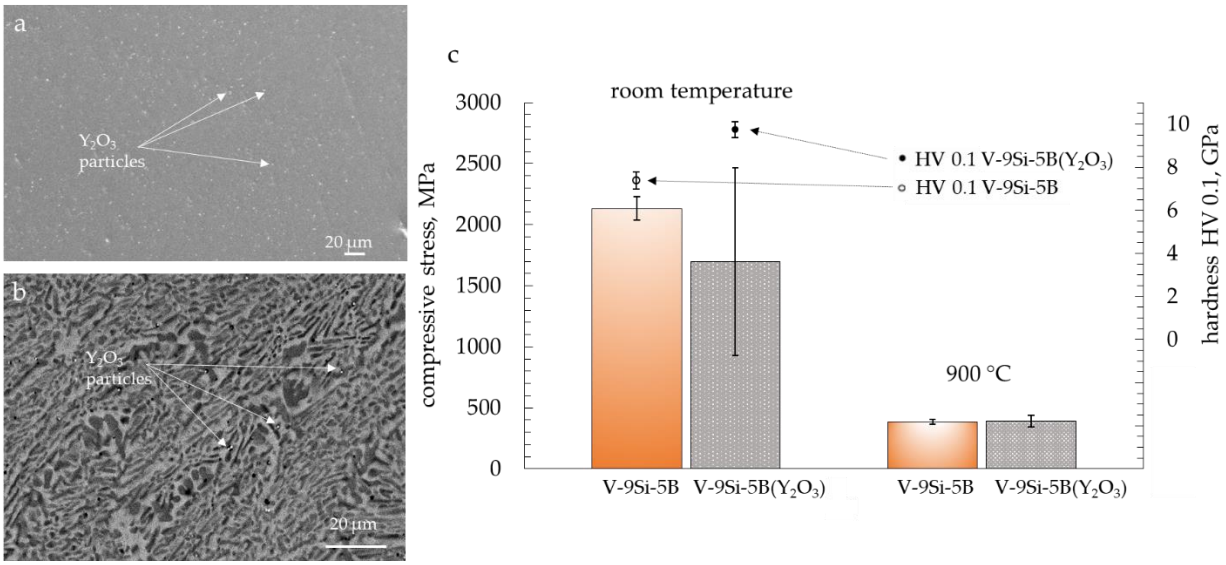

Figure 6.14: AM V-9Si-5B(Y_2O_3) build showing a) homogenously distributed Y_2O_3 particles (white spots) and b) site of the Y_2O_3 particles within the ternary eutectic regions of the V-9Si-5B microstructure, c) comparison of unmodified AM V-9Si-5B material with Y_2O_3 strengthened V-9Si-5B material concerning compressive strength and hardness.

An investigation on the amount of Y_2O_3 particles after AM reveals a loss of the dispersoids during processing. The amount of Y_2O_3 particles after L-DED was determined with 1.8 vol. % (optical

measurement of the SEM images as shown in Figure 6.14 a)). The reasons for such high losses up to 67.3 % Y_2O_3 in for V-9Si-5B(Y_2O_3) builds needs to be clarified, as no regions of enrichment could be found within the specimens.

Preliminary results on the mechanical properties of the L-DED V-9Si-5B(Y_2O_3) material compared to the unmodified material are shown in Figure 6.14 c). As the ternary eutectic of the V-9Si-5B(Y_2O_3) is dominated by the weak V_{ss} phase the enrichment with Y_2O_3 particles has a noteworthy hardening effect and results in an increase of hardness values from 7.39 ± 0.39 GPa for the base alloy to 9.75 ± 0.36 GPa for the modified alloy. The results of the uniaxial compression tests are depicted in Figure 6.14 c). Due to a limited number of specimens, the values presented can only be understood as a trend and do not yet reflect validated values. No clear trend of increasing strength could be determined with regard to the RT compression tests as the average compressive stress before failure drops from 2132 ± 94 MPa to 1697 ± 770 MPa for the reinforced alloy. The large deviations of the values can be attributed to the currently still pronounced porosity of the material which will be optimized in the future by adapting the process parameters of L-DED. For investigations at 900 °C a preliminary positive trend towards an enhanced strength due to the ODS approach was determined. Further research on this topic is necessary and will follow beyond the scope of this thesis.

6.3.3 Creep performance of V-9Si-5B alloy

An important issue for the aimed high temperature application of V-Si-B alloys is a good creep performance in order to provide a slow deformation rate, e.g. for the example of turbine blades, emerging from the centrifugal forces [224]. The creep behavior of the V-9Si-5B alloy manufactured via FAST and L-DED was determined by compressive creep tests with applied true stresses ranging between 50 MPa and 200 MPa. With regard to the potential operating temperatures of the V-based alloys as structural material (e. g. in low pressure turbines), the creep tests have been performed at a temperature of 900 °C. The results are presented in Figure 6.15 a), where the double logarithmic plots of the applied constant creep stress and the minimum or secondary creep rate (Norton plot) for the alloys is shown.

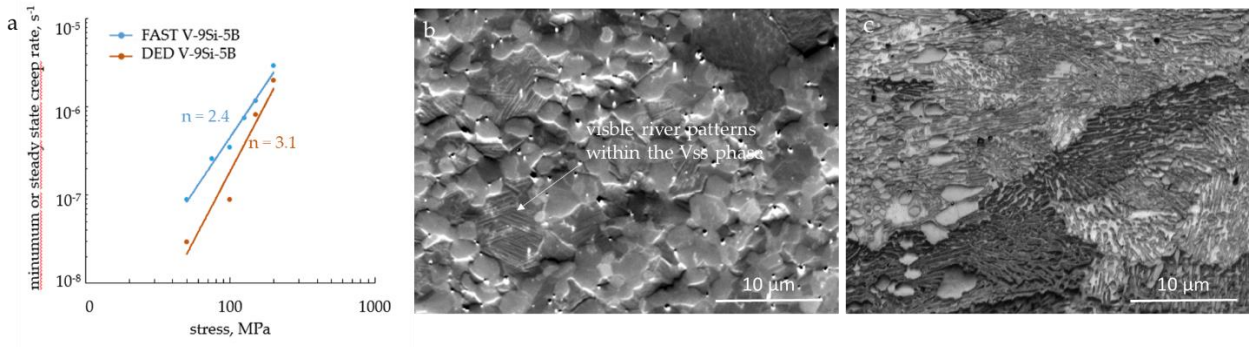

Figure 6.15: a) Creep rate versus stress (Norton plot) of the FAST and L-DED V-9Si-5B alloy with the calculation of stress exponent and SEM-SE images showing the microstructure after creep tests (50 MPa, 900 °C) for b) FAST V-9Si-5B with visible plastic deformation within the V_{ss} phase and c) eutectic cells of L-DED V-9Si-5B.

The creep behavior of both alloys is affected by their fine microstructure as well as their high volume fraction of the V_{ss} phase (> 50 vol. %), which is compared to the silicide phases the weakest phase in the V_{ss}-V_3Si-V_5SiB_2 system [22].

In general, the minimum creep rate of the alloys investigated in this thesis, was found to be in the similar order of magnitude, namely at a creep rate of about 10^{-7} s^{-1}. On a more detailed observation, it can be found that the L-DED V-9Si-5B alloy provides a slightly improved creep resistance in comparison to the FAST V-9Si-5B alloy. One reason for this can be seen in the different grain sizes already shown in Figure 6.12. As the L-DED alloy provides a 5 – 15 times larger grain size (in the form of eutectic cells) in comparison to the FAST V-9Si-5B alloy, the potential contribution of grain boundary sliding is significantly reduced. This assumption is supported by the number of the stress exponents n, which are provided in Figure 6.15 a). The stress exponent of the FAST V-9Si-5B alloy was determined with n = 2.4 and thus indicates a creep behavior predominantly controlled by grain boundary sliding. For the L-DED V-9Si-5B alloy a stress exponent of n = 3.1 was determined and indicates next to grain boundary sliding a predominantly dislocation controlled creep behavior.

Furthermore, besides the grain size, the microstructural constituents of the eutectic cells of the AM material should also be included to interpret the creep response of the material. In comparison to the FAST V-9Si-5B alloy, the L-DED V-9Si-5B alloy reveals a 12 vol. % higher fraction of the weak V_{ss} phase, but the creep rate the of the L-DED material is shown to be lower. After creep tests at 50 MPa and 900 °C the formation of river patterns within the V_{ss} phase was observed for the FAST V-9Si-5B alloy (see Figure 6.15 b)). Similar observations are known from the solid solution phase of the Mo-Si-B system [225] as well as investigations of a cast V-9Si-5B alloy [16] and may indicate microductility due to the observed local plastic deformation. This phenomenon could be observed particularly within the larger V_{ss} regions as found in the V-9Si-5B FAST material and demonstrates next to the well-known low creep resistance of the V_{ss} phase the dependence on the size of the solid solution regions. In comparison, the extreme fine distribution of the V_{ss} phase within the eutectic cells of the L-DED V-9Si-5B alloy seems to be more favorable in terms of creep resistance. The eutectic cells provide a V_{ss}-V_3Si-V_5SiB_2 microstructure where the V_{ss} phase forms the matrix phase in an ultra-fine scale while the silicide phases seems to act as reinforcing phases (particle strengthening mechanism [226]), which leads to increased dislocation climb to overcome these obstacles. This assumption would confirm the stress exponent of n = 3.1 (dislocation controlled creep) and the slightly enhanced creep performance in comparison to the FAST alloy, as dislocation climb is known to lower the creep rate. Besides the dominance of dislocation climb, sliding at the phase boundaries (in analogy to grain boundary sliding) within the very fine eutectic microstructure should to be taken into account as competing mechanism.

In Figure 6.16 the stress on the individual phases after creep (900 °C, 150 MPa) determined by Kernel Average Misorientation (KAM) analysis, is visualized. KAM indicates the local misorientation derived from the EBSD data and provides a qualitative analysis of the dislocation density, respectively, a qualitative localization of the plastic deformation of the material [227]. A comparison of both materials (FAST V-9Si-5B and L-DED V-9Si-5B) after creep tests (900 °C, 150 MPa) revealed that dislocation movement, resulting in plastic deformation of the material, was mostly governed by the V_{ss} phase. The higher plasticity of V_{ss} compared to the silicide phases was also reported by Krüger in [15]. In comparison, plastic deformability of the silicide phases is assumed at temperatures above 1200 °C while brittle behavior and the formation of micro-cracks

under compressive load is observed at temperatures below 1200 °C [15], [22], [228]. As shown in Figure 6.16 both the V_3Si and V_5SiB_2 phases show no significant increase of local misorientation in both alloys and thus strongly contribute to the improvement of strength and creep resistance of the materials.

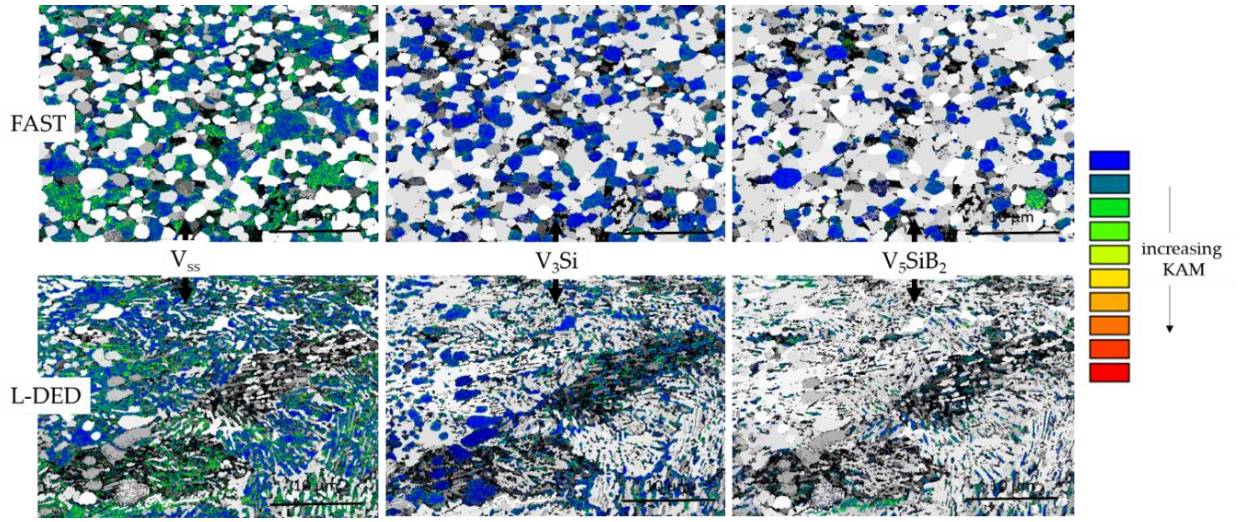

Figure 6.16: KAM analysis of FAST V-9Si-5B and L-DED V-9Si-5V showing qualitatively the plastic deformation after creep tests performed at 900 °C and 150 MPa.

The silicide phases (V_3Si and V_5SiB_2) of both the FAST and the L-DED V-9Si-5B alloy seems to be nearly unaffected under creep load, indicated by KAM analysis (Figure 6.16). It should be noted that both alloys exhibit a qualitatively similar deformation behavior of the V_{ss} phase but the L-DED V-9Si-B alloy has a slightly reduced creep rate. This clearly confirms the significant influence of the microstructural differences arising due to different manufacturing processes. As a conclusion, the weak creep performance of the V_{ss} matrix phase can be significantly improved by the very fine eutectic microstructure resulting from processing via AM, where a notable strengthening effect occurs due to the short distances of recurring silicide phases within the V_{ss} matrix.

A comparison of the creep response of different high temperature materials, i. e. PM/IM V-9Si-13B [15], Al-40Ti [7], Co-Ni super alloy [8] and CMSX-4 [216], is given in Figure 6.17. Since no further data are currently available in literature for the alloy composition V-9Si-5B, the material was compared to similar ternary V-9Si-13B alloys manufactured via powder and ingot metallurgy. The V-9Si-5B alloys present have proven to be competitive in terms of creep resistance, as their creep response can be found in a similar order of magnitude to the materials presented for comparison in Figure 6.17. The V-9Si-13B alloys show lower creep rates. It must be taken into account that they provide a higher proportion of the creep-resistant silicide phases [15]. However, compared to PM V-9Si-13B the difference in creep behavior is relatively small. This is associated with the nearly continuous V_{ss} phase of the reference V-9Si-5B alloys and PM V-9Si-13B alloy as well as a typical process-related fine grained microstructure in the lower micrometer range which leads to an increased tendency for grain boundary sliding. A noticeable improvement of the creep resistance for alloy PM V-9Si-13B by nearly one order of magnitude due to grain

coarsening as a result of heat treatment was reported in [15]. This observation is a well-known phenomenon, as the larger grain size reduces the tendency for grain boundary sliding. It can be assumed that this effect can also be demonstrated for the FAST V-9Si-5B. As heat treatment of the L-DED V-9Si-5B alloy (shown in Figure 6.11) results in a transformation of the eutectic cells into a V_{ss} matrix phases with homogenously distributed V_3Si and V_5SiB_2 phases with nearly the same grain scale like the as-received FAST V-9Si-5B alloy, the effect cannot be predicted at the present time for the L-DED V-9Si-5B alloy.

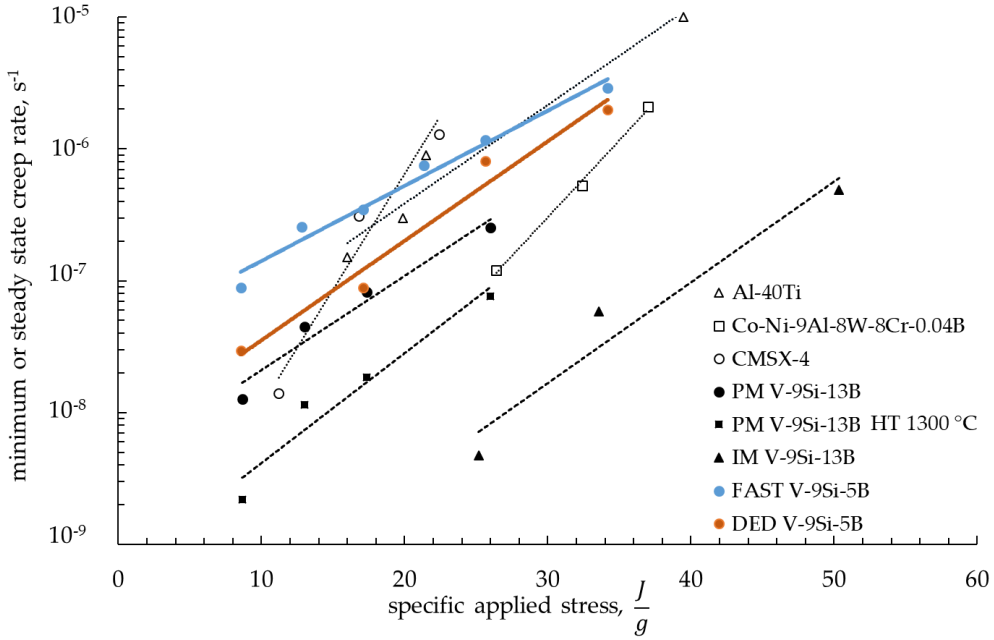

Figure 6.17: Comparison of creep performance (Norton plot) of FAST V-9Si-5B and L-DED V-9Si-5B material with data available from literature for PM/IM V-9Si-13B [15], Al-40Ti [7], Co-Ni super alloy [8] and CMSX-4 [216] at 900 °C.

However, in comparison to an IM V-9Si-13B alloy the alloys investigated in this thesis provide significantly lower creep resistance due to the following reasons: The IM V-9Si-5B alloy is firstly characterized by a significantly coarser microstructure than the FAST/AM alloys and secondly provides a V_3Si-V_5SiB_2 matrix, which tremendously improves the creep resistance and once again confirms the high impact of silicides on the creep strength of V_{ss}-V_3Si-V_5SiB_2 alloys [15]. However, an intermetallic matrix also leads to a significant reduction of the room temperature toughness, which is important for appropriate low temperature properties, as already demonstrated for the structurally similar Mo-Si-B materials in [229].

Compared to other high temperature materials considered for applications in the same temperature regime, such as Al-40Ti, the creep performance of the V-Si-B alloys investigated is in good agreement. The conventionally used Ni-base superalloy CMSX-4 as well as a recently developed model Co-Ni superalloy [8], where the addition of Co was found to increase the creep strength, provide a decreased creep rate in comparison to the V-9Si-5B alloys.

6.4 Cyclic oxidation of V-9Si-5B compacts

In addition to mechanical properties at ambient and elevated temperatures, the oxidation resistance of potential high temperature structural materials is a decisive criterion for application. Cyclic oxidation tests provide an excellent imitation of real conditions including heating and cooling comparable to start and shut-down processes in high temperature turbines [230]. Thus, cyclic oxidation behavior of the FAST and L-DED V-9Si-5B alloys at elevated temperatures was investigated according to the test methods described in Chapter 3.5. The oxidation tests were carried out by the Institut für Korrosions- und Schadensanalyse, Magdeburg, Germany.
Comparatively few studies on the oxidation kinetics of vanadium, especially vanadium silicides, have been published to date [11], [211], [231]. However, comparative studies on pure vanadium or various alloyed V-Al alloys predict an inherently poor oxidation resistance, as the predominantly occurring oxide V_2O_5 melts at 670 °C and evaporates due to a high vapor pressure at almost 800 °C [231], [232]. Accordingly, the temperatures chosen for testing were set at a subcritical temperature of 600 °C as well as the potential application temperature of 900 °C, to achieve a first impression on the oxidation behavior of this innovative silicide material. In Figure 6.18 the tested material after 140 h of cyclic oxidation at 600 °C is shown. Both specimens provide a continuous and tenacious typically yellow colored V_2O_5 oxide scale. This corresponds to results reported in [11], [89], [211]. Compared to the structurally similar Mo-Si-B alloys, where the so-called "pesting" phenomenon occurs at moderate temperatures (600 °C - 800 °C) [211], [233], V-Si-B alloys show no disintegration of the material and provide a continuous solid scale of the competing oxides V_2O_5, VO_2 and SiO_2 up to 670 °C.

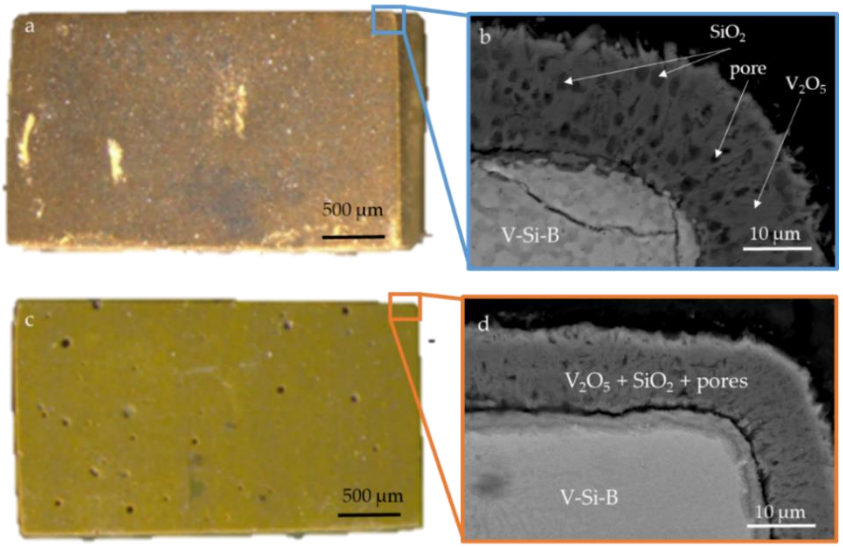

Figure 6.18: Optical microscopy and SEM image of a cross section of V-9Si-5B compacts after cyclic oxidation at 600 °C after 140 h with oxide scale formation on the specimen surface for a) and b): FAST V-9Si-5B and c) and d): L-DED V-9Si-5B.

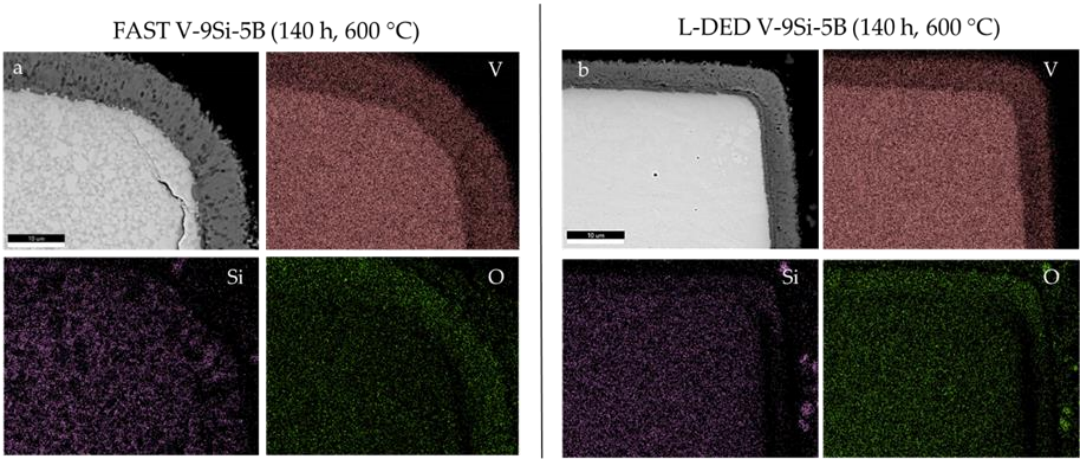

Figure 6.19: SEM-SE micrograph of the a) FAST and b) L-DED V-9Si-5B alloys oxidized at 600 °C for 140 h combined with EDS element mapping for V, Si and O.

SEM micrographs of the oxidized alloys after total exposure of 140 h are depicted in Figure 6.18 b) and d). The formed scales predominantly consist of V_2O_5 as well as smaller regions of SiO_2 and pores (determined by EDS analysis). An EDS element mapping of both oxidized specimens is provided in Figure 6.19. The scale thickness was determined with 16.1 µm ± 1.3 µm for the FAST V-9Si-5B alloy and 11.18 µm ± 1.1 µm for the L-DED V-9Si5B alloy.

The corresponding mass change curves determined for FAST and L-DED V-9Si-5B at 600 °C are depicted in Figure 6.20, where they are compared to a PM V-9Si-13B alloy [11] as well as the pure silicide phase V_5Si_3 [211], a low alloyed V-5Cr-5Ti alloy [89], and the single crystal nickel-base superalloy CMSX-4 alloy [11]. At 600 °C both alloys provide a mass gain as a result of the formation of a continuous V_2O_5 scale. Due to an immediate mass loss at the beginning of the exposure time, the data seems to start below zero. The curves show extrapolated values. A total mass gain for the FAST and L-DED alloy was determined with 0.031 mg/mm² ± 0.003 mg/mm² and 0.0156 mg/mm² ± 0.001 mg/mm², respectively, which is consistent with the slightly different oxidation layer thicknesses measured, see Figure 6.18 and 6.19. While the FAST alloy depicts an almost linear behavior ending in a mass gain comparable to the PM V-9Si-13B alloy, the oxidation of the L-DED material follows a parabolic rate law and provides a significant lower mass gain after 140 h of cyclic oxidation. The ultra-fine microstructure of the eutectic cells of the L-DED V-9Si-5B alloy seems to be favorable in terms of oxidation resistance. Both alloys depict a mass loss at the initial stage. Mass gain and the associated formation of a protective scale starts after 40 h of oxidation for the coarser grained FAST specimen. In comparison, as a result of the ultra-fine microstructure of the L-DED specimen the diffusion paths for the reaction of O_2 with either V_{ss}, V_3Si or V_5SiB_2 are much smaller and the formation of a protective V_2O_5 layer was observed from 17 h of exposure up to 60 h where a plateau-like behavior and a constant scale thickness is reached. An improvement of the oxidation behavior of a structurally similar AM Mo-Si-B alloy compared to a directionally grown counterpart as a result of the microstructure scale effect was also described in [230]. It is somehow surprising that both alloys investigated provide a slightly better oxidation resistance compared to the PM V-9Si-13B showing a higher amount of silicide phases, which are known to provide a protective and oxidation resistant glassy phase, as it was observed in a similar way for Mo-Si-B alloys in [200].

Compared to the alloy V-5Cr-5Ti studied by Natesan and Uz [89], a lower mass gain over the entire oxidation regime of investigation was found. CMSX-4 and V_5Si_3 provide a minor mass gain compared to the alloys studied as the inherent oxidation resistance of both materials is increased in comparison to pure V or the V_{SS} phase. Interestingly, though the amount of the solid solution phase is > 50 vol. %, the L-DED V-9Si-5B material is the only V-Si-B material from Figure 6.20 that, like the strong oxidation resistant V_5Si_3 phases and the Ni-based superalloy CMSX-4, shows a plateau formation accompanied by a constant oxide layer thickness, which prevents the substrate material from further diffusion processes as well as changes of the materials geometry. A possible reason can be seen in the extreme fine distribution of the oxidation resistant silicides V_3Si and V_5SiB_2 within the L-DED V-9Si-5B alloy.

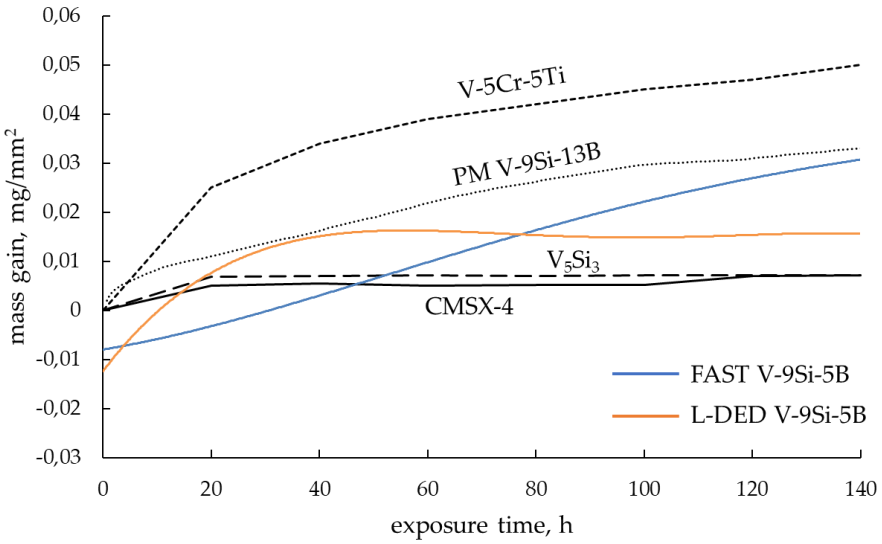

Figure 6.20: Specific mass change of FAST and L-DED V-9Si-5B at 600 °C compared to mass change of PM V-9Si-13B [11], V_5Si_3 [211], V-5Cr-5Ti [89] and CMSX-4 [11].

A significant mass change as well as a change in sample geometry was observed for oxidation tests in air performed at 900 °C. After exceeding the melting point of V_2O_5, the liquid V_2O_5 starts to drip off the V-9Si-5B samples into the crucible below, as it can be seen in Figure 6.21 a) and b) for both the FAST and L-DED samples. Furthermore, the high vapor pressure of V_2O_5 above 800 °C resulted in porosity in the liquid oxide scales and evaporation of the oxide and impedes the formation of a protective SiO_2/SiO_2-B_2O_3 scale [232]. The SEM image in Figure 6.21 c) shows the dripped of V_2O_5 phase with a peripheral zone of exposed and rinsed out silicide phases in the vicinity of the substrate material. The mass losses after 5 minutes of exposure were determined with 0.12 mg/mm² for the FAST specimen and 0.09 mg/mm² for the L-DED specimen. Corresponding images are shown in Figure 6.21 a) and b). In correlation to the slightly smaller mass loss, the L-DED sample still shows clearly defined contours after an exposure time of 5 minutes, suggesting that the microstructural evolution of the L-DED sample leads to a slightly improved oxidation resistance due to the fine distribution of the oxidation resistant silicide phases. However, the high amount of the oxidation-sensitive V_{ss} phase finally leads to massive mass losses up to a catastrophic oxidation behavior of the material and confirm the poor oxidation

behavior of V-based alloys as consensually reported in literature in [89], [211], [231], [232]. It can be stated that the V_{ss} phase occurring in the V-Si-B material suffers from a catastrophic oxidation behavior above temperatures of 670 °C due to the formation of a liquid oxide phase which precluded the formation of a continuous, protective layer. For temperatures below 670 °C a protective V_2O_5 scale forms on the specimen's surface. For the V-Si-B material it is known that the silicide phases provide an excellent oxidation resistance compared to the V_{ss} phase [11], [211], but the formation of a protective SiO_2-B_2O_3 glass layer, as it is reported for the structural similar Mo-Si-B alloys, was not observed for FAST and L-DED V-9Si-5B. Smaller SiO_2 regions forms next to the predominant V_2O_5 at 600 °C. At a testing temperature of 900 °C, scale formation is prevented by the dripping off and evaporation of the liquid V_2O_5 which finally results in a catastrophic oxidation behavior.

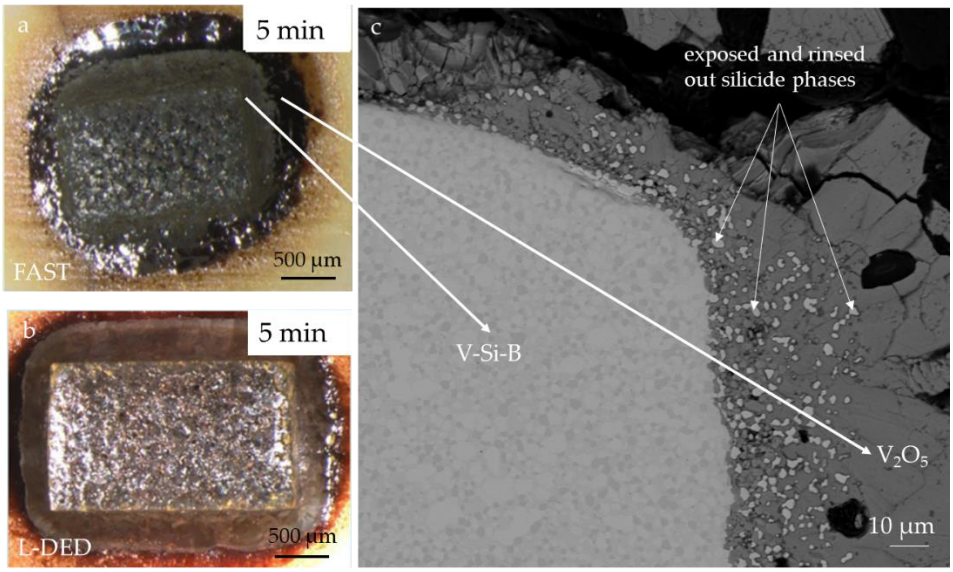

Figure 6.21: Oxidation test of alloy V-9Si-5 with a) FAST V-9Si-5B after oxidation test at 900 °C, b) L-DED V-9Si-5B after 5 min of oxidation at 900 °C and c) SEM image of FAST V-9Si-5B showing the dripped off V_2O_5 scale.

Various approaches to improve the oxidation resistance of V by alloying addition of Al, Ti, Cr or Zr as well as Si and B have been discussed in [11], [89], [231], [232]. Though a reduction of oxidation rate of V-30Al, V-30Al-10Ti, and V-30Al-10Cr with 43 %, 34 %, and 28 % compared to pure vanadium, respectively, was reported [232]. Chromium additions were found to be most effective in terms of vanadium oxidation improvement due to a lowering of the oxidation rate [89], [232]. Furthermore, additions of Si and B benefit due to the formation of oxidation resistant silicide phases which at the same time serve as Si and B reservoir for a possible formation of an oxidation protective borosilicate glass layer [11], [233]. However, for all materials the problematic formation of liquid V_2O_5 could not be suppressed completely. A suppression of the formation of V_2O_5 seems to be essential for a successful implementation of vanadium-base alloys intended for high temperature application at ambient oxygen pressure. A possibility to overcome this problem can be found in the application of coatings. Promising coating strategies for protection of refractory metal-based alloys are given by polymer derived ceramics (e. g. SiO_2/SiNO

layers + boron-containing fillers) [234], [235], PVD techniques like magnetron sputtering [236] or pack cementation by co-deposition of Si and B resulting in improved environmental resistance and lifetime of the material [237], [238].
While polymer derived ceramic coatings, which leads to the formation of a protective SiO_2 or better SiO_2-B_2O_3 layer, for V-Si-B materials are still unexplored, Hasemann et al. [96] reported on first results of coating reactions on vanadium and V-Si-B alloys during powder pack cementation. The coating application has demonstrated excellent coverage and oxidation resistance and thus seems to be promising to enable a high temperature application for this new class of V-Si-B alloys.

7 Summary and conclusion

The doctoral thesis can be summarized with the following main findings and conclusions:

1. For basic understanding, the mechanical alloying (MA) process was investigated with respect to the mechanisms and kinematics of the planetary ball milling process. The assumed local energy dependency of the ball motion pattern considered for numerical calculation of the kinetic energy input was visualized by means of DEM simulation. The maximum energies of the milling balls do not represent the effective dissipated energies, as they additionally depend on the relative velocity as well as the mass of the respective impact partners. By means of DEM simulation the dissipated energy was determined to be significantly lower than the energy that could have been transferred in ideal collision events.

2. Mechanical alloying (MA) of V-Si powder compositions up to 25 at. % Si was investigated concerning microstructural evolution, phase formation and powder morphology. Mechanically induced dissolution of up to 25 at. % Si in the vanadium lattice leads to the formation of homogenous and supersaturated solid solution powder particles as well as the formation of the V_3Si phase (due to high energy collisions), which is the equilibrium phase for the alloy composition V-25Si. Due to the forces acting during MA, hardening of the powder particles was observed. An increase of the solid solution hardening was determined with increasing Si concentration as well as hardening by means of grain size reduction due to mechanically induced formation of dislocation networks. The strongest hardening effect can be attributed to the work hardening which is assumed to contribute by 58.5 % for the example of V-4Si (20 h of milling).

3. Subsequent heat treatment of the supersaturated V-(2…25)Si pre-alloyed powder material resulted, according to phase diagram, in the precipitation of the silicide phase V_3Si. A decrease of the V_3Si second phase fraction due to increased solubility of Si in the vanadium lattice with increasing temperature was confirmed for the powder material as well. The hardness of the powder alloy was found to increase with the beginning of precipitation of the V_3Si phase, as the hardness of the single V_3Si phase is significantly higher than that of the V_{ss} phase.

4. MA of V-Si-B powder material was found to follow the previous results of the binary V-Si system and provide high similarities compared to the similar and well investigated Mo-Si-B system. A comparison of the impact energy by means of different milling tools, namely stainless steel (SS) and tungsten carbide (WC), was described by a semi empirical model and revealed an acceleration of the milling progress for WC tools, as they offer a higher density which leads to a higher energy impact. However, higher impact forces result in increased flaking of small particles from the WC tools which contaminates the powders.

5. Pre-alloyed MA V-9Si-5B material was consolidated by means of field assisted sintering technology (FAST) and a fine and homogenous microstructure in the lower µm-range was observed, which is comparable to other sintered three-phase V-Si-B alloys as well as the crystallographically similar Mo-Si-B alloys. Furthermore, qualification of V-Si-B material for additive manufacturing (AM) by means of L-DED was successfully shown. For this purpose, gas atomized, pre-alloyed powder particles were used, as the MA powder particles could not provide a constantly powder flow rate during build-up which finally resulted in intolerable porosity in the compacts. Significantly lower oxygen contaminations were measured for the powders from the gas atomization process. Similar findings apply to the compacts that were additively manufactured from the GA powder material.

6. In comparison to FAST V-9Si-5B compacts the AM V-9Si-5B builds provide an even finer and almost ternary V_{ss}-V_3Si-V_5SiB_2 eutectic microstructure. The layer-wise build-up is characterized by an alternation of the deposition layers and the coarser grained fusion lines connecting the individual layers. While the FAST alloy provides a phase fraction of 51.8 vol. % V_{ss} phase, the fast cooling conditions during AM processing led to a V_{ss} volume fraction of 66.6 vol. %. Subsequent annealing revealed a non-equilibrium state of the as-built AM alloys as the volume fraction of the V_{ss} phase decreases after heat treatment to 54 vol. %.

7. The mechanical properties of both materials were investigated in the as-built state. Despite the increased V_{ss} volume fraction of the AM V-9Si-5B compact, which is known to be the weakest phase in the ternary V_{ss}-V_3Si-V_5SiB_2 system, the very fine ternary eutectic structure of the AM build exceeds the properties of the sintered alloy in terms of hardness and temperature dependent strength (RT – 900 °C) under compressive load. However, the creep response of both alloys at 900 °C was found to be in the similar order of magnitude. However, the ultra-fine eutectic microstructure of the L-DED V-9Si-5B material was found to be slightly more creep resistant as the silicides act as strengthening phases within the V_{ss} matrix. This can be considered in analogy to a particle hardening mechanism due to the necessary dislocation climb to overcome the silicides.

8. As another important property for potential high temperature applications of V-Si-B materials, the oxidation behavior at 600 °C and 900 °C has been investigated. After exposure at 600 °C both alloys show a mass gain as a result of the formation of a protective V_2O_5 scale, which forms as a continuous layer on the specimen's surface. At 900 °C the V-9Si-5B material suffers from catastrophic oxidation. After exceeding the melting point of V_2O_5 (T_m = 670 °C), which was found the prevailing oxide to be forming, the liquid V_2O_5 started to drip off of the V-9Si-5B samples into the crucible resulting in significant mass losses and change of the specimen contour. At a testing temperature of 900 °C scale formation is prevented by the dripping off and evaporation of the liquid V_2O_5.

Future prospects

Additive manufacturing seems to be a promising manufacturing route for V-Si-B material (exemplarily shown by alloy V-9Si-5B) as less impurities, significantly lower oxygen contamination as compared to FAST V-9Si-5B as well as a convincing microstructure-property relationship was determined. However, additive manufacturing up to now is only carried out on a laboratory scale and residual porosity of the material is still too high. Since the stress-strain behavior of the alloys was only determined in a compressive mode, an optimization and scale-up of the process accompanied by the possibility of manufacturing larger sized specimens for testing in tensile mode is recommended, as tensile tests represent application-related strains and damage mechanisms, e.g. formation of micro pores.

Temperature and time-dependent stability of the material for application-related conditions at 900 °C and beyond are essential for investigations in the future. First experiments at 1400 °C revealed significant coarsening of the alloy as well as a change of the phase distribution. First investigations gave insights in the materials behavior of this new type of alloys but for deeper understanding of the time and temperature-dependent deformation mechanisms a more detailed analysis is necessary.

Further strengthening of the material by ODS particles can provide a decisive contribution for improving the ambient and high temperature properties of V-Si-B material especially in terms of strengthening the weak V_{ss} phase.

However, a fundamental point to work on is the poor oxidation resistance of V-rich V-Si-B materials. Next to alloying with e.g. Al, Ti, Zr or Cr, which were found to be the most effective elements for improving the oxidation resistance of V-based alloys, a coating of the material seems to be essential if this material is considered for high temperature structural application in ambient conditions. Potential approaches are pre-ceramic polymers or the pack cementation method to provide a dense and protective coating for the V-Si-B alloys.

Appendix

Table A.1: Particle size d_{80} of V(Si) powder particles after different milling times.

	V-2Si		V-4Si		V-15Si		V-25Si	
$d_{I,80}$, µm	53.5		47.6		63.3		126.2	
milling time, h	$d_{F,80}$, µm	W_{ic}, mJ	$d_{F,80}$, µm	W_{ic}, mJ	$d_{F,80}$, µm	W_{ic}, mJ	$d_{F,80}$, µm	W_{ic}, mJ
2	141.1	-41.36	110.1	-42.69	84.9	-120.06	75.5	78.61
10	105.9	-53.44	100.7	-46.62	66.8	-535.37	53.3	40.91
20	89.2	-67.41	85.3	-56.25	53.1	173.66	-	-
100	59.4	-280.01	53.1	-232.22	45.2	83.15	40.5	27.63

Table A.2: Properties of various V-Si alloys.

	lattice parameter V, Å	oxygen content, ppm	Fe impurities, vol. %	phase distribution, vol.%	
				V_{ss}	V_3Si
V-2Si					
as milled	3.033674	5943.2 ±234	-	100	-
1000 °C	3.033539	8470.5 ± 530	-	100	-
1100 °C	3.036870	6338.8 ± 143	-	91.38	8.62
1300 °C	3.033764	11716.2 ± 123	-	97.76	2.24
1400 °C	3.033898	11911.3 ± 1162	-	100	-
V-4Si					
as milled	3.033570	6143.7 ± 211	-	100	-
1000 °C	3.033498	8209.3± 55	-	100	-
1100 °C	3.036396	9178.8± 437	-	80.59	19.41
1300 °C	3.034788	9026.6 ± 43	-	86.22	13.78
1400 °C	3.033026	9718.09 ± 532	-	89.38	10.62
V-15Si					
as milled	3.030841	6001.1 ± 187	-	100	-
1000 °C	3.031030	8061.9.±.701	-	100	-
1100 °C	3.042284	9347.2 ± 773	-	23.86	76.14
1300 °C	3.043014	8955.9 ± 167	-	23.16	76.84
1400 °C	3.043262	11174.1.±.1006	-	23.11	76.89
V-25Si					
as milled	3.041864	5548.1 ± 272	-	100	-

1000 °C	3.049087	7270.8.±.152	-	100	-
1100 °C	3.079467	8521.6 ± 370	1.26	1.28	97.46
1300 °C	3.079945	8395.2 ± 138	1.25	1.05	97.70
1400 °C	-	11083.3 ± 1048	1.70	-	97.20

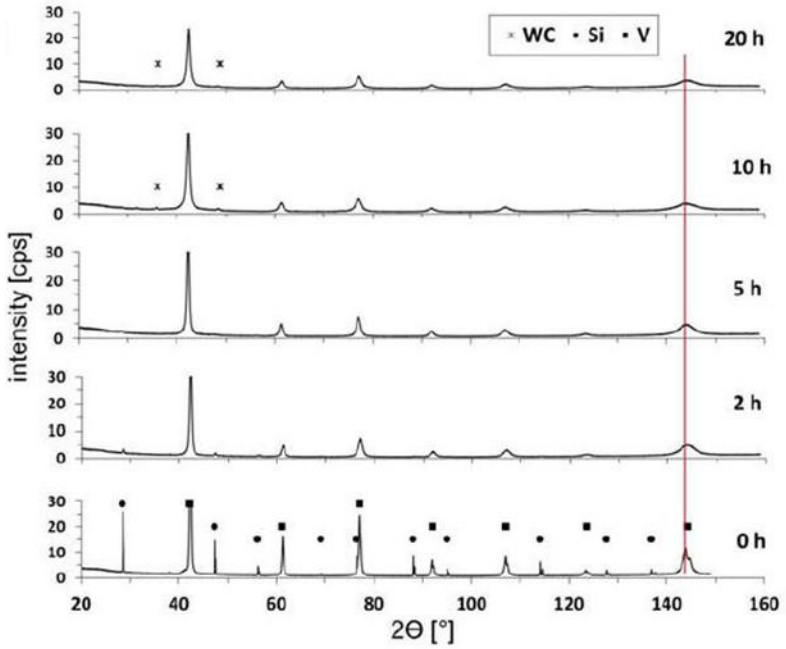

Figure A.1: X-ray diffractograms of MA V-9Si-13B WC powder (150 rpm).

Table A:3: Oxygen concentration of MA V-9Si-13B powders after different milling times with respect to the grinding tool and rotational speed of the planetary ball mill.

grinding tool	SS		WC	
milling duration, h	150 rpm	200 rpm	150 rpm	200 rpm
1	8345 ± 345	11088 ± 521	7268 ± 825	6349 ± 678
10	7932 ± 450	6471 ± 566	7233 ± 257	9653 ± 451
20	7841 ± 268	6588 ± 1027	9368 ± 1021	7341 ± 231
50	8032 ± 542	7546 ± 490	8347 ± 753	7544 ± 567

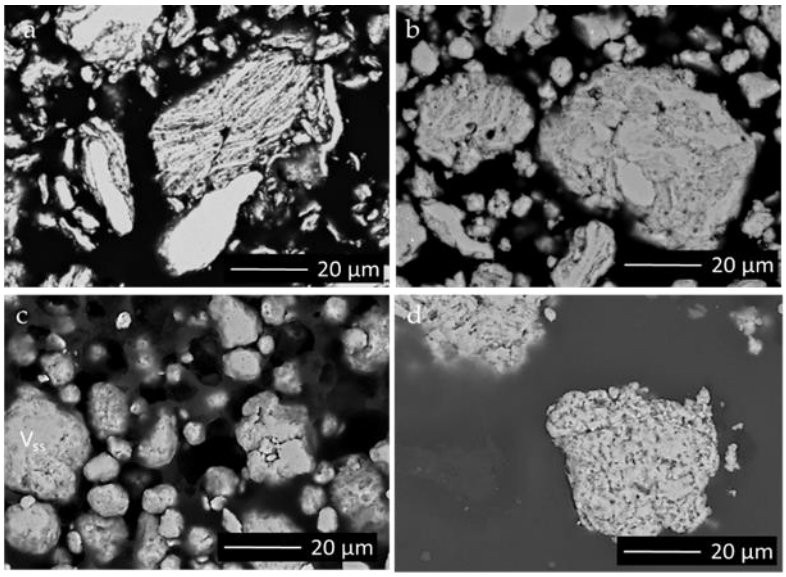

Figure A.2: Milling progress of V-9Si-19B after a) 2 h of MA, b) 10 h of MA, c) 20 h of MA and d) 20 h MA and heat treatment at 1400 °C (1h).

Table A.4: Oxygen concentration of raw material and V-9Si-5B, V-9Si-13B and V-9Si-19B.

	Oxygen concentration, ppm		
raw material	V	Si	B
	5100 ± 428	10783 ± 350	705 ± 22
milling duration, h	**V-9Si-5B**	**V-9Si-13B**	**V-9Si-19B**
1	8248 ± 275	11088.2 ± 521	9790 ± 173
2	10176 ± 382	9988.3 ± 433	16032 ± 1397
5	79624 ± 1194	9897± 647	14971 ± 750
10	7870 ± 672	6471.8 ± 566	11103 ± 1203
20	814462 ± 1409	6588.9 ± 1027	8535 ± 281
50	8393 ± 521	5920 ± 812	10480 ± 1188
20 HT	21357 ± 478	21098 ± 611	24583 ± 358

Table A.5: Particle size distribution of V-9Si-5B, V-9Si-13B and V-9Si-19B.

	particle size d_{50}, µm		
milling duration, h	V-9Si-5B	V-9Si-13B	V-9Si-19B
1	27.3	36.8	36.6
2	31.9	37.7	39.9
5	29.5	39.5	31.1
10	23.1	36.0	28.4
20	24.7	27.4	26.7
50	27.6	29.1	25.9
20 HT	25.7	24.9	27.3

Table A.6: Micro hardness HV 0.1 of V-9Si-5B, V-9Si-13B and V-9Si-19B.

	microhardness, GPa		
milling duration, h	V-9Si-5B	V-9Si-13B	V-9Si-19B
1	6.62 ± 1.46	5.28 ± 1.5	8.84 ± 1.69
2	6.85 ± 0.97	7.92 ± 2.7	6.77 ± 1.44
5	7.41±1.01	8.41 ± 1.1	7.65 ± 1.47
10	8.39±1.45	9.57 ± 1.7	8.04 ± 1.95
20	8.29±1.19	12.21 ± 2.0	8.82 ± 1.17
50	8.13±1.84	10.84 ± 2.2	9.15 ± 1.96
20 HT	10.97 ± 0.99	12.03 ± 1.9	11.71 ± 1.13

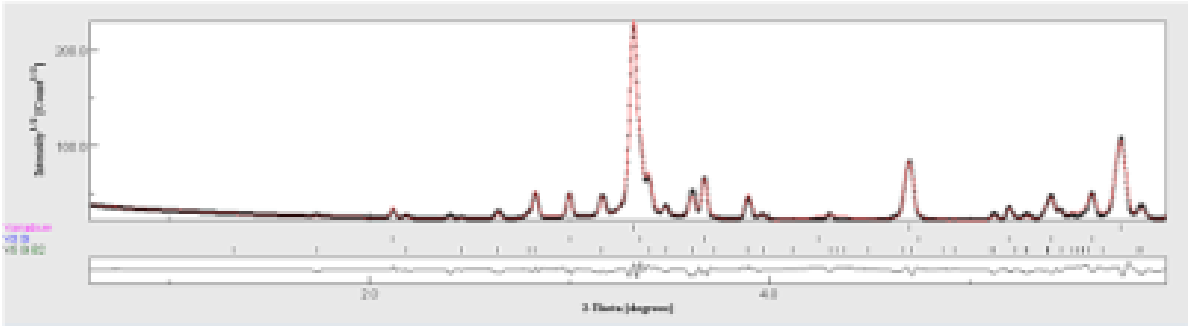

Figure A.3: XRD data of a V-9Si-5B alloy manufactured via DED.

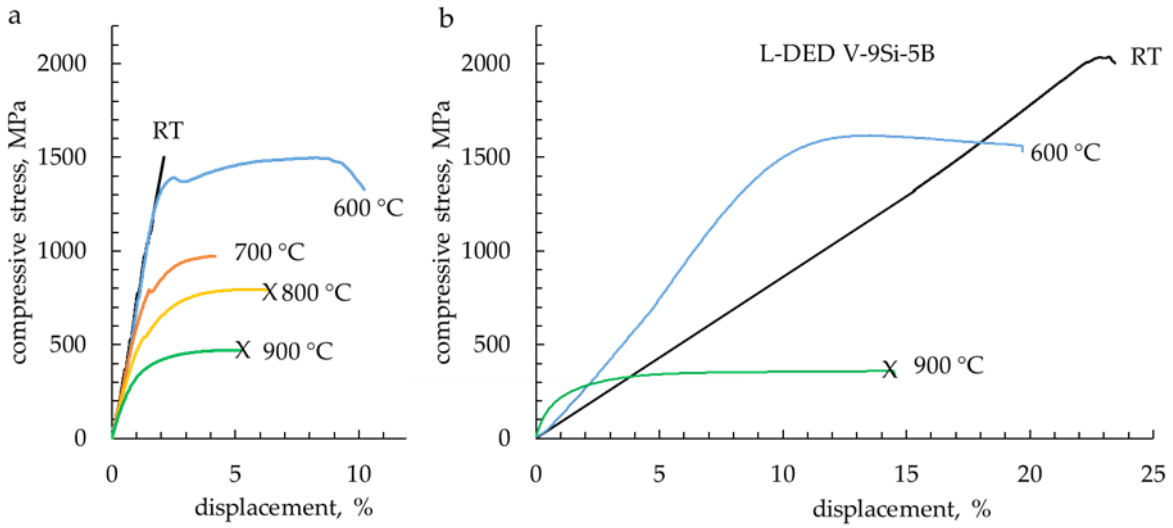

Figure A.4: Stress strain curves from compression tests conducted for a) FAST V-9Si-5B and b) DED V-9Si-5B. Since a larger amount of sample material was available for the FAST V-9Si-5B alloy, more extensive investigations could be carried out.

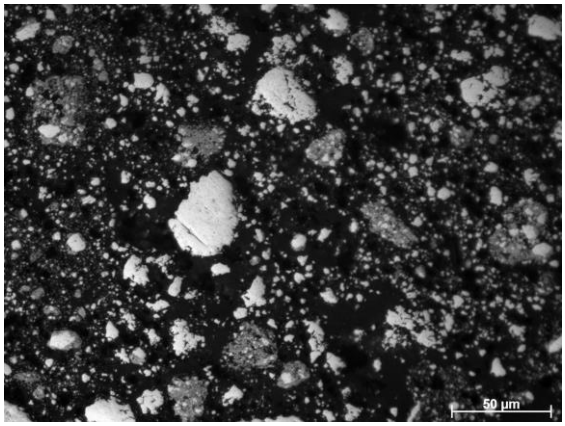

Figure A.5: Light microscopy image showing the shows the large variance of particle sizes in a bimodal V-9Si-13B system after 50 h of milling with WC tools at a rotational speed of 200 rpm in a planetary ball mill.

References

[1] MTU entwickelt neuen Werkstoff für Turbinenschaufeln. https://www.flugrevue.de/flugzeugbau/titanaluminid-mtu-entwickelt-neuen-werkstoff-fuer-turbinenschaufeln/, april 2021.

[2] W. Smarsly. *Werkstoffe für Luftantriebe-Symposium 30 Jahre GWP Gesellschaft für Werkstoffprüfung mbH*. Zorneding, 2007.

[3] Y. Koizumi, T. Kobayashi, T. Yokokawa, Z. Jianxin,M. Osawa, H. Harada,Y. Aoki, M. Arai. *Development of Next-Generation Ni-Base Single Crystal Superalloys*. Journal of the Japan Institute of Metals - Conference Paper, 2004, doi: 10.7449/2004/Superalloys_2004_35_43.

[4] Aircraft turbine with a view of the individual components. https://www.sourcingstreamlined.com/aviation/part-types/aircraft-turbine-engine-parts/, april 2021.

[5] W. O. Soboyejo, T.S. Srivatsan. *Advanced structural materials: Properties, Design, Optimization, and Applications*. CRC Press, Boca Raton, 2006.

[6] H. Clemens, S. Mayer. *Pulvermetallurgische Herstellung von innovativen Hochtemperaturwerkstoffen*. BHM Berg- und Hüttenmännische Monatshefte, doi: 10.1007/s00501-018-0704-1, 2018.

[7] D. Sturm, M. Heilmaier, H. Saage, M. Paninski, G.J. Schmitz, A. Drevermann, M. Palm, F. Stein, N. Engberding, K. Kelm,S. irsen. *Creep strength of centrifugally cast Al-rich TiAl alloys*. Materials Science and Engineering A, 510–511:373–376, 2009.

[8] C.H. Zenk, S. Neumeier, N.M. Engl, S.G. Fries, O. Dolotko, M.Weiser, S. Virtanen, M. Göken. *Intermediate Co / Ni-base model superalloys — Thermophysical properties , creep and oxidation*. Scripta Materialia, 112:83–86, 2016.

[9] O.N. Senkov, S.V. Senkova, C. Woodward, D.B. Miracle. *Low-density , refractory multi-principal element alloys of the Cr – Nb – Ti – V – Zr system : Microstructure and phase analysis*. Acta Materialia., 61a(5):1545–1557, 2013.

[10] M. Krüger, B. Köppe-Grabow. *Process-Oriented Microstructure Evolution of Vss -V_3Si-V_5SiB_2 Materials. Praktische Metallographie*, doi: 10.3139/147.110456, 2017.

[11] M. Krüger. *High temperature compression strength and oxidation of a V-9Si-13B alloy*. Scripta Materialia, 121:75–78, 2016.

[12] H. Matsui, K. Fukumoto, D.L. Smith, H. M. Chung, W. van Witzenburg, S.N. Votinov. S*tatus of vanadium alloys for fusion reactors*. Journal of Nuclear Materials, 233-237:92–99, 1996.

[13] D.L. Smith, B.A. Loomis, D.R. Diercks. *Vanadium-base Alloys For Fusion Reactor Applications - A Review*. Journal of Nuclear Materials, 135:125–139, 1985.

[14] T. Muroga, T. Nagasaka, K. Abe, V.M. Chernov, H. Matsui, D.L. Smith, Z.-Y. Xu, S.J. Zinkle. *Vanadium alloys – overview and recent results*. Journal of Nuclear Materials, 307–311:547–554, 2002.

[15] M. Krüger, V.Bolbut, F. Gang, G. Hasemann. *Microstructure Variations and Creep Properties of Novel High Temperature V-Si-B Materials*. JOM, 68(11):2811-2816, 2016.

[16] G. Hasemann, C. Müller, D. Grüner, E. Wessel, M. Krüger. *Room temperature plastic deformability in V-rich V-Si-B alloys*. Acta Materialia., 175:140–147, 2019.

[17] T. Mukherjee, J. S. Zuback, A. T. DebRoy. *Printability of alloys for additive manufacturing*. Nature, doi: 10.1038/srep19717, 2016.

[18] G. Witt, A. Wegner, J. T. Sehrt. *Neue Entwicklungen in der additiven Fertigung - Beiträge aus der wissenschaftlichen Tagung der Rapid.Tech 2015*. Springer Vieweg, 2015.

[19] J. Choi, Y. Chang. *Characteristics of laser aided direct metal/material deposition process for tool steel*. Int. J. Mach. Tools Manuf., 45(4–5):597–607, 2005.

[20] R. M. Mahamood. *Laser Metal Deposition Process of Metals, Alloys and Composite Materials*. Springer, Berlin, 2018.

[21] S. J. Zinkle, H Matsui, D.L Smith, A.F Rowcliffe, E van Osch, K Abe, V.A Kaza. *Research and development on vanadium alloys for fusion applications*. Journal of Nuclear Materials, 258–263(1 A):205–214, 1998.

[22] H. Bei, E.P. George, E.A. Kenik, G.M. Pharr. *Microstructures and mechanical properties of V–V3Si eutectic composites*. Zeitschrift für Metallkunde, 95:505–512, 2004.

[23] V. V Shyrokov, C.B. Vasyliv, O.V. Shyrokov. *Ways of improving the high-temperature work service of vanadium and some alloys used in reactors*. Journal of Nuclear Materials, 394(1):114–122, 2009.

[24] G. Gottstein. *Physikalische Grundlagen der Materialkunde*. Springer, Berlin Heidelberg, 2007.

[25] B.A. Loomis, D.L. Smith. *Vanadium alloys for structural applications in fusion systems: a review of vanadium alloy mechanical and physical properties*. Journal of Nuclear Materials, 191–194:84–91, 1992.

[26] B.B. de Lima-Kuehn, A.A.A.P. da Silvaa, P.A. Suzukia, G.C. Coelho, C.A. Nunes. *Microstructural Characterization of As-Cast V-Si Alloys and Reevaluation of the Invariant Reactions Involving the Liquid Phase of the V-Si System*. Materials Research., 19(5):1122-1126, 2016.

[27] H. Massalski, T.B. Murray, J.L. Bennett, L.H. Baker. B*inary alloy phase diagrams*. ASM International, Ohio, 1990.

[28] G. Sauthoff. Intermetallics. VCH, Weinheim, doi.org/10.1002/nadc.19960440432, 1995.

[29] E.Z. Medvedev, A.I. Dolgikh, V.Y. Ivanovskiy, A.L. Kuznetsov, Y V. Gubanov, V.A. Kurmayev. *X-ray emission spectra and the electronic structure of compounds V_3Si and V_3Ge alloyed with transition metals*. Physics of Metals and Metallography, 57(2):29-36, 1984.

[30] R.Z. Fleischer, R.L. Gilmore, R.S. Zabala. *Elastic moduli of polycrystalline, high-temperature binary intermetallic compounds*. Acta Metall., 37(10):2801–2803, 1989.

[31] K. Nghiep, D.M. Quyen, N.H. Paufler, P. Bertram, M. Kleinstuck, A. Kramer, U. San Martin. *Influence of Chemical Composition on Dislocation Structure and its Change by Plastic Deformation of V_3Si Single Crystals*. Krist. und Tech., 15:733–741, 1980.

[32] N.H. Nghiep, D.M. Paufler, P. Kramer, U. Kleinstock, K.Quyen. *Creep deformation of V3Si single crystals*. Journal of Materials Science, 15:140-1 146, 1980.

[33] G. Ilonce,T. W. Berbee. *Superconductivity in V-Si and V-Si-C alloy films*. Physica Status Solidi, 47(2):357-364, 1978.

[34] J. F. Smith. *Phase diagrams of binary vanadium alloys*. ASM Int., 1989.

[35] C. Zhang, Y. Du, W. Xiong, H. Xu, P. Nash, Y. Ouyang. *Thermodynamic modeling of the V – Si system supported by key experiments*. Comput. Coupling Phase Diagrams Thermochem., 32:320–325, 2008.

[36] T. Ishimasa, Y. Fukano. *Related content Crystal Structure and Morphology of Fine Particles of Vanadium Silicides*. Japanes J. Appl. Sci., 22:6–11, 1983.

[37] X. Tao, H. Chen, X. Tong, Y. Ouyang, P. Jund, J. Tedenac. *Structural , electronic and elastic properties of V_5Si_3 phases from first-principles calculations*. Comput. Mater. Sci., 53(1):169–174, 2012.

[38] H.H. Hausner. *Modern Developments in Powder Metallurgy*. Springer US, 1966.

[39] L. Liu, S. Casadio, M. Magini, C. A. Nannetti. *Formation of the intermetallic compound VSi2 and a VSi2-SiC composite by mechanical alloying*. Journal of Alloys Compounds, 227(1):76–81, 1995.

[40] J. Williams, M. Akinc. *Oxidation Behavior of V_5Si_3 based materials*. Intermetallics, 6:269-275, 1998.

[41] H. Nowotny, E. Dimakopoulou, H. Kudielka. *Untersuchungen in den Dreistoffsystemen: Molybdän-Silizium-Bor, Wolfram-Silizium-Bor und in dem System: VSi_2-$TaSi_2$*. Monatshefte für Chemie, 88(2):180–192, 1957.

[42] H. Inui. *Plastic deformation of single crystals of VSi_2 and $TaSi_2$ with the C40 structure*. Intermetallics, 6:723–728, 1998.

[43] R.J. Schutz, L.R. Testardi. *The formation of vanadium silicides at thin- film interfaces*. J. Appl. Phys., doi: 10.1063/1.326718, 1979.

[44] J. Schmelzer, T. Baumann, S. Dieck, M. Krüger. *Hardening of V-Si alloys during high energy ball milling*. Powder Technology 294:493–497, 2016.

[45] M. Krüger, J. Schmelzer, M. Helmecke. *Similarities and differences in mechanical alloying processes of V-Si-B and Mo-Si-B powders*. Metals, doi:10.3390/met6100241, 2016.

[46] H. Kudielka, H. Nowotny, G. Findeisen. *Untersuchungen in den Systemen: V-B, Nb-B, V-B-Si und Ta-B-Si*. Monatshefte fiir Chemie, 88(6), 1957.

[47] C.A. Nunes, B.B. De Lima, G.C. Coelho, P.A. Suzuki. *Isothermal section of the V-Si-B system at 1600 °C in the V-VSi_2-VB region*. J. Phase Equilibria Diffus., 30(4):345–350, 2009.

[48] A.A.A.P. Da Silva, N. Chaia, F. Ferreira,G.C. Coelho, J.-M. Fiorani, N. David, M. Vilasi, C.A. Nunes. Thermodynamic modeling of the V-Si-B system. Calphad, 5i9:199–206, 2017.

[49] C. A. Nunes, B. B. De Lima, G. C. Coelho, P. Rogl, P. A. Suzuki. *On the stability of the V_5B_6-phase*. Journal of Alloys Compounda. 370:164–168, 2004.

[50] B.B. De Lima, C.A. Nunes, G.C. Coelho, P.A. Suzuki, P. Rogl. *Evaluation of the Invariant Reactions of the V-B System*. JPEDAV, 25(2):134–139, 2004.

[51] D.M. Dimiduk, J.H. Perepezko. *Mo-Si-B alloys: Developing a revolutionary turbine-engine material*. MRS Bull., 28(9):639–645, 2003.

[52] G. Hasemann, D. Kaplunenko, I. Bogomol. *Near-Eutectic Ternary Mo-Si-B Alloys : Microstructures and Creep Properties*. JOM, 68(11): 2847-2853, 2016

[53] G. Hasemann, M. Krüger, M. Palm, F. Stein. *Microstructures of ternary eutectic refractory Me-Si-B (Me = Mo, V) alloy systems*. Mater. Sci. Forum, 941:827–832, 2018.

[54] J. Becker, *Dissertation: Development of density reduced Mo-Si-B alloys*. Otto-von-Guerick-Universität Magdeburg, 2019.

[55] A C.N.D.A.P. Reis, C.A. Nunes. *Caracterizacao microestrutural e quimica de ligas V-Si-B*. Rev.

Bras. Apl. Vacuo, 26(2):79–82, 2007.

[56] G. Hasemann. *Experimental study of the liquidus surface in the V-rich portion of the V-Si-B system*. Journal of Alloys and Compounds, 824:153843, 2020.

[57] J.H. Schneibel. *Mo-Si-B Alloy Development*. 17th Annu. Conf. Foss. energy Mater.,865:3–9, 2003.

[58] M. Krüger. *Dissertation: Pulvermetallurgische Herstellung und Charakterisierung von oxidationsbeständigen Molybdänbasislegierungen für Hochtemperaturanwendungen*. Berlin, 2010.

[59] G.A. Henshall, M.J. Strum, B.P. Bewlay, J.A. Sutliff. *Ductile-Phase Toughening in V-V_3Si In Situ Composites*. Metall. Mater. Trans. A, 28:2555–2564, 1997.

[60] D.P. Mason, D.C. Van Aken. *On The Creep Of Directionally Solidified $MoSi_2$-Mo_5Si_3 Eutectics*. Acta metall. mater., 43(3):1201-1210, 1995.

[61] G. Hasemann, I. Bogomol, D. Schliephake, P. I. Loboda, M. Krüger. *Microstructure and creep properties of a near-eutectic directionally solidified multiphase Mo-Si-B alloy*. Intermetallics, 48:28–33, 2014.

[62] M. Regenberg, G Hasemann, C Müller, M Krüger. *Microstructure-property relations of eutectic V-Si and V-B alloys*. IOP Conference Series Materials Science and Engineering, doi: 10.1088/1757-899X/882/1/012014, 2020.

[63] C. Müller, G. Hasemann, M. Regenberg, U. Betke, M. Krüger. *Microstructure and compression properties of V_{ss}-V_3B_2 eutectic alloys in the V-Si-B system*. Materials, 13(9):2100, 2020.

[64] P. Jehanno, M. Heilmaier, H. Saage. *Assessment of the high temperature deformation behavior of molybdenum silicide alloys*. Materials Science and Engineering, 463(A):216–223, 2007.

[65] P.R. Santhanam, E.L. Dreizin. *Predicting conditions for scaled-up manufacturing of materials prepared by ball milling*. Powder Technol., 221:403–411, 2012.

[66] M. Krüger, S. Franz, H. Saage, M. Heilmaier, J.H. Schneibel, P. Jehanno,M. Böning, H. Kestler. *Mechanically alloyed Mo-Si-B alloys with a continuous α-Mo matrix and improved mechanical properties*. Intermetallics, 16(7):933–941, 2008.

[67] I.D. Radomysel'skii, V.P. Solntsev, O.V Evtushenko. *Powder metallurgy of vanadium and its alloys*. Powder Metallurgy Materials, Parts, and Coatings, 5:367–372, 1987.

[68] R. Kieffer, H. Braun. *Vanadium, Niobium, and Tantalum (Russian translation)*. Metall. Moscow, 1986.

[69] F. Eisenkolb. *Advances in Powder Metallurgy (Russian translation)*. Metall. Moscow, 1969.

[70] C.T. Wang, E.F. Baroch, S.A. Worcester, Y S. Shen. *Preparation and properties of high-purity vanadium and V-15Cr-5Ti*. Met. Trans, 6:1683–1689, 1970.

[71] P.F. Zheng, T. Nagasaka, T. Muroga, and J. M. Chen. *Investigation on mechanical alloying process for vanadium alloys*. J. Nucl. Mater., 442(1-3):330–S335, 2013.

[72] W. Schatt, K.-P. Wieters, B. Kieback. Pulvermetallurgie: *Technologien und Werkstoffe*. Springer, Berlin-Heidelberg, 2007.

[73] H. U. Kessel, J. Hennicke, J. Schmidt, T. Weißgärber, B.F. Kieback, M. Herrmann, J. Räthel. *FAST: field assisted sintering technology- a new process for the production of metallic and ceramic sintering materials*. Heimdall Verlag, Witten, 2006.

[74] O. Guillon, J. Gonzalez-Julian, B. Dargatz, T. Kessel, G. Schierning, J. Räthel, M. Herrmann. *Field-Assisted Sintering Technology / Spark Plasma Sintering : Mechanisms ,*

Materials , and Technology Developments. doi: 10.1002/adem.201300409, 2014.

[75] E. Baril, L.P. Lefebvre, Y. Thomas. *Interstitial elements in titanium powder metallurgy : sources and control*. Powder metallurgy,54(3):183–187, 2011.

[76] C. Zhong, A. Gasser, J. Kittel, J. Fu, Y. Ding, R. Poprawe. *Microstructures and tensile properties of Inconel 718 formed by high deposition-rate laser metal deposition*. J. Laser Appl., doi: https://doi.org/10.2351/1.4943290, 2016.

[77] J. Yu, M. Rombouts, G. Maes, F. Motmans. *Material properties of Ti_6Al_4V parts produced by laser metal deposition*. Physics Procedia, 39:416–424, 2012.

[78] J. Yu, M. Rombouts, G. Maes. *Cracking behavior and mechanical properties of austenitic stainless steel parts produced by laser metal deposition*. doi: 10.1016/j.matdes.2012.08.078, 2013.

[79] L. Xue, A. Theriault, B. Rubinger, D. Parry, F. Ranjbarab, M. Doyon. *Manufacturing structural components by laser consolidation*. Ind. Laser User, 36:31–33, 2004.

[80] T.M. Smith, A.C. Thompson, T.P. Gabb, C.L. Bowman, C.A. Kantzos. *Efficient production of a high-performance dispersion strengthened , multi-principal*. Sci. Rep., doi: 10.1038/s41598-020-66436-5, 2020.

[81] Y. Jialin. *Selective laser melting additive manufacturing of advanced nuclear materials V-6Cr-6Ti*. Mater. Lett., 209:268–271, 2017.

[82] O. Bouaziz , N. Guelton. *Modelling of TWIP effect on work-hardening*. Materials Science and Engineering A, 319–321:246–249, 2001.

[83] D. Gu, Y. Shen, G. Meng. *Growth morphologies and mechanisms of TiC grains during Selective Laser Melting of Ti – Al – C composite powder*. Mater. Lett., 63(29): 2536–2538, 2009.

[84] D. Gu, Y. Shen, Z. Lu. *Preparation of $TiN – Ti_5Si_3$ in-situ composites by Selective Laser Melting*. Mater. Lett., 63(18–19):1577–1579, 2009.

[85] M. Rösler, J. Harders, H. Bäker. *Mechanical behavior of engineering materials*. Springer, Heidelberg, 2007.

[86] J. Pelleg. *Creep in Ceramics*. Springer, 2017. .

[87] H.J. Maier, T. Niendorf, R. Bürgel. *Handbuch Hochtemperatur-Werkstofftechnik*. Springer-Vieweg, 2015.

[88] V. Bolbut, *Dissertation: Development of Mo-Hf-B and Mo-Zr-B alloys for high-temperature application*. Otto-von-Guericke-Universität Magedburg, 2018.

[89] K. Natesan, M. Uz. *Oxidation performance of V-Cr-Ti alloys*. Fusion Eng. Des., 51–52:145–152, 2000..

[90] J.G. Keller, D.L. Douglas. *The High-Temperature Oxidation Behavior of Vanadium-Aluminum Alloys*. Oxid. Met., 36, 1991.

[91] M. Krüger. *Habilitationsschrift: Innovative metallische Hochtemperaturwerkstoffe*. Otto-von-Guericke-Universität Magdeburg, 2017.

[92] J.D. Klicker, H.B. Bomberger. *A Study on Controlling High Temperature Oxidationof Vanadium-Base alloys*. 1961.

[93] D. Sturm, M. Heilmaier, J.H. Schneibel, P. Jéhanno, B. Skrotzki, H. Saage. *The influence of silicon on the strength and fracture toughness of molybdenum*. Mater. Sci. Eng. A, 463(1–2):107–114, 2007.

[94] C.A. Krier. *Coatings for the protection of refractory metals for oxidation*. Defense metall deformation center, Batelle Memorial Istitute, Columbus, 1961.

[95] S. Mathieu, N. Chaia, M. Le Flem, M. Vilasi. *Multi-layered silicides coating for vanadium*

alloys for generation IV reactors Surface & Coatings Technology Multi-layered silicides coating for vanadium alloys for generation IV reactors. Surf. Coat. Technol., 206(22):4594–4600, 2012.

[96] G. Hasemann, C. Harris, M. Krüger, J. H. Perepezko. *Coating reactions on vanadium and V-Si-B alloys during powder pack-cementation*. Materials, 13(18):2–8, 2020.

[97] C. Suryanarayana. *Mechanical alloying and milling*. Progress in Materials Science, 46:1-184, 2001.

[98] H.Q. Trinh, J.O. Jo, S.B. Lee, Y.S. Mok. *Preparation of red nitride phosphor from powder mixture of metal nitrides using spark plasma sintering*. Curr. Appl. Phys., 14(8):1051–1056, 2014.

[99] P.K.N.J.-L. Huang. *Novel synthesis of ceramic nanocomposites using SPS, strengthening of alumina ceramic matrix nanocompsites using spark plasma sintring*. Advances in Ceramic Matrix Composites, 2014.

[100] I.M. Fedorchenko, A.R. Adrievsky. *The mechanism of sintering in single-component systems.* Powder Metall., 2:47–171, 2014.

[101] V. V. Skorokhod. *Science of Sintering: Evolution of Ideas, Advances, Current Challenges, and New Trends. I. From Natural Philosophy to Physics of Sintering*. Powder Metall Met Ceram, 53:529–540, 2015.

[102] A.Al-Qudsi, M. Kammler, A. Bouguecha, C. Bonk, B.-A. Behrens. *Comparison between different numerical models of densification during solid-state sintering of pure aluminium powder Comparison between different numerical models of densification during solid-state sintering of pure aluminium powder*. doi: 10.1007/s11740-014-0574-7, 2015.

[103] S.-J.L. Kang. *Sintering: Densification, Grain Growth and Microstructure*. Butterworth-Heinemann, 2004.

[104] M. Prakasam, J. Locs, D. Salma-Ancane, K. Loca, A. Largeteau, L. Berzina-Cimdina. *Fabrication , Properties and Applications of Dense Hydroxyapatite : A Review*. J. Funct. Biomater.,doi: 10.3390/jfb6041099, 2015.

[105] M. Suárez, A. Fernández, J.L. Menéndez, R. Torrecillas, H.U. Kessel, J. Hennicke, R. Kirchner, T. Kessel. *Challenges and Opportunities for Spark Plasma Sintering : A Key Technology for a New Generation of Materials*. http://dx.doi.org/10.5772/53706, 2013.

[106] E.A. Olevsky, D.V Dudina, *Field- Assisted Sintering*, Springer, 2018.

[107] X. Guan,Y. F. Zhao. *Modeling of the laser powder–based directed energy deposition process for additive manufacturing: a review*. Int. J. Adv. Manuf. Technol., 107:1959–1982, 2020.

[108] B. Graf, A. Gumenyuk, M. Rethmeier. *Laser metal deposition as repair technology for stainless steel and titanium alloys*. Physics Procedia, 39:376 – 381, 2012.

[109] M. Kurek, W. Brniak. *Printing techniques : Recent developments in pharmaceutical technology*. Acta Poloniae Pharmaceutica, 74(3):753-763, 2017.

[110] E. Brandl, V. Michailov, B. Viehweger, C. Leyens. *Surface & Coatings Technology Deposition of Ti – 6Al – 4V using laser and wire , part I : Microstructural properties of single beads*. Surf. Coat. Technol., 206(6):1120–1129, 2011.

[111] P.A. Kobryn, E.H. Moore, and S.L. Semiatin. *The Effect Of Laser Power And Traverse Speed On Microstructure, Porosity, And Build Height In Laser-Deposited Ti-6Al-4V*. Scripta mater., 43:299–305, 2000.

[112] A. Saboori, D. Gallo, S. Biamino, P. Fino, M. Lombardi. *An Overview of Additive Manufacturing of Titanium Components by Directed Energy Deposition : Microstructure and*

Mechanical Properties. doi: 10.3390/app7090883, 2017.
[113] D. Schulze. *Pulver und Schüttgüter (Vol. 2)*. Springer, Berlin Heidelberg, 2009.
[114] D. Schulze. *Flow Properties of Powders and Bulk Solids*. Braunschweig, 2006.
[115] J.F. Carr, D.M. Walker. *An Annular Shear Cell for Granular Materials*. Powder Technology, 1(6):369-373, 1968.
[116] J.W. Olesik. *Elemental analysis using ICP-OES and ICP / MS. Analytical Chemistry*. 63(1), 1991.
[117] C. Spieß, L. Teichert, G. Schwarzer, H. Behnken, H. Genzel. *Moderne Röntgenbeugung*. Springer, Wiesbaden, 2014.
[118] J.I. Goldstein, D.E. Newbury, J.R. Michael, N.W.M. Ritchi, J.H. Scott, D.C. Joy. *Scanning electron microscopy and X-Ray Microanalysis*. Springer New York, 2003.
[119] J.P. Eberhardt. *Structural and Chemical Analysis of Materials*. Chichester: John Wiley & Sons Ltd., 1991.
[120] "DIN EN ISO 6507-1 Metallische Werkstoffe - Härteprüfung nach Vickers - Teil 1: Prüfverfahren," 2018.
[121] H. Blumenauer. *Werkstoffprüfung*. Leipzig: VEB Deutscher Verlag für Grundstoffindustrie, 1977.
[122] M.E. Kassner. *Fundamentals of Creep in Metals and Alloys*. Butterworth-Heinemann, 2015.
[123] T.A. Parthasarathy, M.G. Mendiratta, D.M. Dimiduk. *Oxidation mechanisms in Mo-reinforced $Mo_5SiB_2(T_2)$–Mo_3Si alloys*. Acta Materialia, 50:1857–1868, 2002.
[124] J. VandeVondele, M. Krack, F. Mohamed, M. Parrinello, T. Chassaing, J. Hutter. *Quickstep: Fast and accurate density functional calculations using a mixed Gaussian and plane waves approach*. Commun. Comput. Phys., 167:103–128, 2005.
[125] J. Hutter, M. Iannuzzi, F. Schiffmann, and J. Vandevondele. *CP2K : atomistic simulations of condensed matter systems*. doi: 10.1002/wcms.1159, 2014.
[126] B.G. Lippert, J. Hutter, M. Parrinello, B.G. Lippert. *A hybrid Gaussian and plane wave density functional scheme*. doi: 10.1080/002689797170220, 2010.
[127] H.J. Monkhorst, J.D. Pack. *Special points for Brillonin-zone integrations*. Phys. Rev. B, 13:5188-5192, 1976.
[128] J. VandeVondele, J. Hutter. *Gaussian basis sets for accurate calculations on molecular systems in gas and condensed phases*. Chem Phys, doi: 10.1063/1.2770708, 2007.
[129] S. Goedecker, M. Teter, J. Hutter. *Separable dual-space Gaussian pseudopotentials*. Phys. Rev. B, 54:1703–1710,1996.
[130] C. Hartwigsen, S. Goedecker, J. Hutter. *Relativistic separable dual-space Gaussian pseudopotentials from H to Rn*. Phys. Rev. B., 58:3641–3662, 1998.
[131] M. Krack. *Pseudopotentials for H to Kr optimized for gradient-corrected exchange-correlation functionals*. Ther. Chem Acc, doi: 10.1007/s00214-005-0655-y, 2005.
[132] J.P. Perdew, K. Burke, M. Ernzerhof. *Generalized Gradient Approximation Made Simple*. Phys Rev Letter, 3:3865–3868, 1996.
[133] A. Togo, I. Tanaka. *First principles phonon calculations in materials science*. Scripta Mat., 108:1–5, 2015.
[134] O.K. Andersen, H.L. Skriver, H. Nohi, B. Johansson. *Electronic Structure Of Transition Metal Compounds ; Ground-State Properties Of The 3d-Monoxides In The Atomic Sphere Approximation*. Pure Appl. Chem, 52:93–118, 1979.

[135] O.K. Andersen, O. Jepsen. *Explicit, First-Principles Tight-Binding Theory*. Phys. Rev. Lett., 53:2571, 1984.
[136] O.K. Andersen. *TB-LMTO v4.7*. Max-Planck-Institut für Festkörperforschung Stuttgart.
[137] J.P. Perdew, J.A. Chevary, S.H. Vosko, K.A. Jackson, M.R. Pederson, D.J. Singh, C. Fiolhais. *Atoms, molecules, solids, and surfaces: Applications of the generalized gradient approximation for exchange and correlation*. Phys Rev B, 46:6671–6687, 1992.
[138] L. Lü, M. O. Lai. *The Mechanical Alloying Process*. in Mechanical Alloying, Boston, MA: Springer US, 23-67, 1998.
[139] J.S. Benjamin. *Dispersion Strengthened Superalloys by Mechanical Alloying*. Metall. Trans.,l:2943–2951, 1970.
[140] P.R. Soni. *Mechanical alloying: Fundamentals and Applications*. Cambridge International Science Publishing, 1999.
[141] W. Hume-Rothery, G.W. Mabott, K.M. Channel Evans. *The Freezing Points, Melting Points, and Solid Solubility Limits of the Alloys of Silver, and Copper with the Elements of the B Sub-Groups*. Philos. Trans., 233:1–97, 1934.
[142] G. Zhang, X. Lin, R. Wang, G. Liu, J. Sun. *Tensile properties and strengthening mechanisms of Mo–Si alloy*. Int. Journal of Refractory Metals and Hard Materials 29(5):608–613, 2011.
[143] R.L. Fleischer. *Substitutional solution hardening*. Acta Metall., 11:203–209, 1963.
[144] O. Vöhringer. *Der Einfluß von Legierungsart und -konzentration auf die Streckgrenze von -Kupferlegierungen*. Zeitschrift für Met., 65:352–358, 1974.
[145] L.A. Gypen, A. Deruyttere. *The combination of atomic size and elastic modulus misfit interactions in solid solution hardening*. Scr. Metall., 15:815–820, 1981.
[146] R. Labusch. A Statistical *Theory of Solid Solution Hardening*. Phys. Stat. Sol,. 41:659–669, 1970.
[147] E.O. Hall. *Yield Point Phenomena in Metals and Alloys*. Springer, 1970.
[148] T.G. Nieh, J. Wadsworth. *Hall-Petch relation in nanocrystalline solids*. Scr. Metall. Mater., 25:955–958, 1991.
[149] M.T. Rad, G. Boussinot, M. Apel. *Dynamics of grain boundary premelting*. Sci. Rep., doi: 10.1038/s41598-020-77863-9, 2020.
[150] S. Hong, B. Kim. *Effects of lifter bars on the ball motion and aluminum foil milling in tumbler ball mill*. Mater. Lett., 57:275–279, 2002.
[151] K. Höffl. *Zerkleinerungs- und Klassiermaschinen*. Springer-Verlag, Berlin-Heidelberg, 1986.
[152] M. Krüger, J. Schmelzer, M. Helmecke. *Similarities and Differences in Mechanical Alloying Processes of V-Si-B and Mo-Si-B Powders*. Metals., doi: 10.3390/met6100241,2016.
[153] P. FENG, X. Wang, Y. Qiang, X. Qu. *Energy analysis of mechanical alloying of molybdenum disilicide in a new-type high energy vibrating ball mill*. J. China Univ. Min. Technol., 18(3):449–453, 2008.
[154] M. Abdellaoui, E. Gaffet. *The physics of mechanical alloying in a modified horizontal rod mill: Mathematical treatment*. Acta Mater., 44(2):725–734, 1996.
[155] D.R. Maurice, T.H. Courtney. *The Physics of Mechanical Alloying - a 1st Report*. Metall. Trans. A, Physical Metall. Mater. Sci., 21:289–303, 1990.
[156] J. Kano, H. Mio, F. Saito, M. Miyazaki. *Correlation of grinding rate of gibbsite with impact energy in tumbling mill with mono-size balls*. Miner. Eng., 14(10):1213–1223, 2001.

[157] T. Yang, X. Guo, Y. Luo. *Microstructural evolution of mechanically alloyed Mo–Si–B–Zr–Y powders*. Int. J. Refract. Met. Hard Mater., 56:35–43, 2016.
[158] G.B. Schaffer, J. S. Forrester. *The influence of collision energy and strain accumulation on the kinetics of mechanical alloying*. J. Mater. Sci., 32(12):3157–3162, 1997.
[159] M. Abdellaoui, E. Gaffet. *The physics of mechanical alloying in a planetary ball mill: Mathematical treatment*. Acta Metall. Mater., 43(3):1087–1098, 1995.
[160] H. Stroppe. *Physik* (in German), Carl Hanser Verlag GmbH & Co. KG, München, 2011.
[161] M. Krüger, O. Kauss, K. Naumenko, C. Burmeister, E. Wessel, J. Schmelzer. *The potential of mechanical alloying to improve the strength and ductility of Mo – 9Si – 8B – 1Zr alloys – experiments and simulation*. Intermetallics, 113:106558, 2019.
[162] P.A. Cundall, O. D. L. Strack. *A discrete numerical model for granular assemblies*. Geotechnique, 29(1):47–65, 1979.
[163] H. Hertz. *Über die Berührung fester elatischer Koerper*. J. für die reine Angew. Math, 92:156–171, 1881.
[164] R.D. Mindlin. *Compliance of elastic bodies in contact*. J. Appl. Mech., 16:259–268, 1949.
[165] C. Burmeister, L. Titscher, S. Breitung-Faes, A. Kwade. *Dry grinding in planetary ball mills: Evaluation of a stressing model*. Adv. Powder Technol., 29(1):191–201, 2018.
[166] A. Rosenkranz, S. Breitung-Faes, S. Kwade. *Experimental investigations and modelling of the ball motion in planetary ball mills*. Powder Technol., 212:224–230, 2011.
[167] C. Burmeister, A. Stolle, R. Schmidt, K. Jacob, S. Breitung-Faes, A. Kwade. *Experimental and Computational Investigation of Knoevenagel Condensation in Planetary Ball Mills*. Chem. Eng. Technol., 37:857–864, 2014.
[168] K.P. Gupta. *The Ni-Si-V (Nickel-Silicon-Vanadium) System*. J Phs Eqil Diff, 26(4):385–389, 2005.
[169] C. Suryanarayana. *Mechanically induced fcc phase formation in nanocrystalline hafnium Mechanically induced fcc phase formation in nanocrystalline hafnium.* doi: 10.1063/1.3100037, 2009.
[170] P.J. Yvon, R. B. Schwarz. *Effects of iron impurities in mechanical alloying using steel media*. J. Mater. Res., 8(2):1992–1994, 1993.
[171] D. Wang, L.-S. Fan. *Particle characterization and behavior relevant to fluidized bed combustion and gasification systems. in Fluidized Bed Technologies for Near-Zero Emission Combustion and Gasifaication*, Woodhead Publishing Series in Energy, 2013.
[172] K. Schwister, V. Leven. *Verfahrenstechnik für Ingnieure*. Carl Hanser Verlag GmbH & Co. KG, München, 2014.
[173] F.C. Bond. *Crushing and grinding calculations*. Br. Chem. Eng, 6:378–385, 1991.
[174] M. Stieß. *Mechanische Verfahrenstechnik 2.* Springer, Berlin-Heidelberg, 1997.
[175] A. Jankovic, H. Dundar, R. Mehta. *Relationships between comminution energy and product size for a magnetite ore.* Journal of The Southern African Institute of Mining and Metallurgy, 110:17–20, 2010.
[176] E. Müller, C. Oestreich. *Handling of Highly Dispersed Powders*. Shaker Verlag, Aachen, 2004.
[177] A. Gupta, D. S. Yan. *Mineral Processing Design and Operation*. Elsevier: New York, 2006.
[178] J. Kano, H. Mio, F. Saito. *Correlation of size reduction rate of inorganic materials with impact energy of balls in planetary ball milling*. J. Chem. Eng. Japan, 32(4):445–448, 1999.
[179] H. Mio, J. Kano, F. Saito. *Scale-up method of planetary ball mill*. doi: 10.1016/j.ces.2004.07.020,

2004.

[180] V. Domnich, Y. Aratyn, W.M. Kriven, Y. Gogotsi. *Temperature Dependence Of Silicon Hardness : Experimental Evidence Of Phase Transformations*. Rev. Adv. Mater.Sci., 17:33–41, 2008.

[181] R.B. Schwarz. *Microscopic model for mechanical alloying*. Materials Science Forum, 269-272:665-674, 1998.

[182] J. Eckert. *Relationships Governing The Grain Size Of Nanocrystalline Metals And Alloys*. NanoStructured Materials, 6:413-416, 1995.

[183] J. Li, T. Ohmura, K. Tsuzaki. *Evaluation of Grain Boundary Effect on Strength of Fe – C Low Alloy Martensitic Steels by Nanoindentation Technique*. Materials Transaction, 46(6):1301–1305, 2005.

[184] N.R. Tao, Z.B. Wang, W.P. Tong, M.L. Sui, J. Lu, K. Lu. *An investigation of surface nanocrystallization mechanism in Fe induced by surface mechanical attrition treatment*. Acta Materialia, 50(18):4603-4616, 2002.

[185] J. Eckert, L. Schultz, K. Urban. *Formation of quasicrystalline and amorphous phases in mechanically alloyed Al-based and Ni-Ti-based alloys*. Acta Metall. Mater., 39(7):1497–1506, 1991.

[186] R.B. Schwarz, R.R. Petrich, C.K. Saw. *The synthesis of amorphous Ni-Ti alloy powders by mechanical alloying*. J. Non. Cryst. Solids, 76(2-3):281–302, 1985.

[187] B.B. De Lima-Kuhn, A.A.A.P. Da Silvaa, P.A. Suzukia, G.C. Coelho, C.A. Nunes. *Microstructural characterization of as-cast V-Si alloys and reevaluation of the invariant reactions involving the liquid phase of the V-Si system*. Mater. Res., 19(5):1122–1126, 2016.

[188] M. Krüger, P. Jain, K. S. Kumar, M. Heilmaier. *Correlation between microstructure and properties of fine grained Mo-Mo_3Si-Mo_5SiB_2 alloys*. Intermetallics, 48:10–18, 2014.

[189] *Thermodynamic Properties of Inorganic Materials comiled by SGTE*. Springer, Berlin Heidelberg, 2007.

[190] L. Liu, C. Sun, C. Zhang, P.M. Voyles, J. Fournelle, A. Handt, J.H. Perepezko. *Examination of B in the Mo solid solution (Moss) in Moss + Mo_5SiB_2 + Mo_2B alloys*. Scripta Mater., 163:62–65, 2019.

[191] Y.W. Kwon, C.T. Liu. *Effect of particle distribution on initial cracks forming from notch tips of composites with hard particles embedded in a soft matrix*. Compos. Part B Engineering, 32(3):199–208, 2001.

[192] J. Zhang, W. Z. Han. *Oxygen solutes induced anomalous hardening, toughening and embrittlement in body-centered cubic vanadium*. Acta Mater., 196:122–132, 2020.

[193] C.C. Koch, J.D. Whittenberger. *Mechanical milling/alloying of intermetallics*. Intermetallics, 4(5):339–355, 1996.

[194] T. Sossaman, R. Sakidja, J.H. Perepezko. *Influence of minor Fe addition on the oxidation performance of Mo – Si – B alloys*. Scripta. Mater., 67(11)891–894, 2012.

[195] G. Hasemann. *Unpublished oxidation experiments*. 2016.

[196] I. Moravcik, A. Kubicek, L. Moravcikova-Gouvea, O. Adam, V. Kana, V. Pouchly, A. Zadera, I. Dlouhy. *The Origins of High-Entropy Alloy Contamination Induced by Mechanical Alloying and Sintering*. Metals, doi.org/10.3390/met10091186, 2020.

[197] M. Krüger, P. Jain, K. S. Kumar, M. Heilmaier. *Correlation between microstructure and properties of fine grained Mo-Mo_3Si-Mo_5SiB_2 alloys*. Intermetallics, 48:10-18, 2014.

[198] M. Krüger, O. Kauss, K. Naumenko, C. Burmeister, E. Wessel, J. Schmelzer. *The potential of mechanical alloying to improve the strength and ductility of Mo–9Si–8B–1Zr alloys – experiments and simulation*. Intermetallics, 113:106558, 2019.

[199] C. Colinet, J.C. Tedenac. *First principles calculations of the stability of the T2 and D88 phases in the V-Si-B system*. Intermetallics, :50:108–116, 2014.

[200] F.A. Rioult, S.D. Imhoff, R. Sakidja, J.H. Perepezko. *Transient oxidation of Mo-Si-B alloys: Effect of the microstructure size scale*. Acta Mater, 57(15):4600–4613, 2009.

[201] M. Krüger, D. Schliephake, P. Jain, K. S. Kumar, G. Schumacher, M. Heilmaier. *Effects of Zr additions on the microstructure and the mechanical behavior of PM Mo-Si-B alloys*. JOM, 65(2):301–306, 2013.

[202] K. Edalati, Z. Horita, R.Z. Valiev. *Transition from poor ductility to room-temperature superplasticity in a nanostructured aluminum alloy*. Sci. Rep.,8:6740, 2018.

[203] R.M. Mahamood. *Laser Metal Deposition of Metals and Alloys*. Springer, 2018.

[204] W. Li, J. Zhang, X. Zhang, F. Liou. *Effect of optimizing particle size on directed energy deposition of Functionally Graded Material with blown Pre-Mixed Multi-Powder*. Manuf. Lett., 13:39–43, 2017.

[205] A. Popovich, V. Sufiiarov. *Metal Powder Additive Manufacturing*. https://doi.org/10.5772/63337, 2016.

[206] S. Spitans, H. Franz, E. Baake. *Numerical Modeling and Optimization of Electrode Induction Melting for Inert Gas Atomization (EIGA)*. Metall. Mater. Trans. B, doi: 10.1007/s11663-020-01934-5, 2020.

[207] G. Witt, A. Wegner, J.T. Sehrt. *Neue Entwicklungen in der Additiven Fertigung*. Springer Vieweg, 2016.

[208] J. Schmelzer, S.-K. Rittinghaus, A. Weisheit, M. Stobik, J. Paulus, K. Gruber, E. Wessel, C. Heinze, M. Krüger. *Printability of gas atomized Mo-Si-B powders by laser metal deposition.* Int. J. Refract. Met. Hard Mater., doi: 10.1016/j.ijrmhm.2018.08.016, 2019.

[209] G.K.L. Ng, A.E.W. Jarfors, G. Bi, H.Y. Zheng. *Porosity formation and gas bubble retention in laser metal deposition*. Appl Phys A, 97:641–649, 2009.

[210] R.A.B. Devine. *Si02 / Si interface degradation and the role of interstitiel oxygen*. J. Phys., III(6):1569–1594, 1996.

[211] J. Williams, M. Akinc. *Oxidation behavior of V_5Si_3 based materials*. Intermetallics, 6(4):269–275, 1998.

[212] S.-K. Rittinghaus, J. Schmelzer, M. W. Rackel, S. Hemes, A. Vogelpoth, U. Hecht, A. Weisheit. *Direct Energy Deposition of TiAl for Hybrid Manufacturing and Repair of Turbine Blades*. Materials, doi: 10.3390/ma13194392, 2020.

[213] J. Gibson, S. Schröders, C. Zehnder., S. Korte-Kerz. *Towards nanoindentation at application-relevant temperatures – A study on CMSX-4 alloy and amdry-386 bond coat*. Beyond Nickel-Based Superalloys, II:1–19, 2016.

[214] S.J. Sun, Y.Z. Tian, H.R. Lin, X.G. Dong, Y.H. Wang, Z.J. Wang, Z.F. Zhang. *Temperature dependence of the Hall–Petch relationship in CoCrFeMnNi high-entropy alloy*. J. Alloys Compd., 806:992–998, 2019.

[215] A. V. Sergueeva, N. A. Mara, and A. K. Mukherjee. *Grain boundary sliding in nanomaterials at elevated temperatures*. J. Mater. Sci., 42(5):1433–1438, 2007.

[216] N. Tsuno, S. Shimabayashi, K. Kakehi, C. Rae, R. Reed. *Tension/compression asymmetry in*

yield and creep strengths of ni-based superalloys. Proc. Int. Symp. Superalloys, doi: 10.7449/2008/superalloys_2008_433_442, 2008.

[217] F. Appel, J.D.H. Paul, M. Oehring, U. Fröbel, U. Lorenz. *Creep behavior of TiAl alloys with enhanced high-temperature capability*. Metall. Mater. Trans. A Phys. Metall. Mater. Sci., 34(10):2149–2164, 2003.

[218] B. T. Dubiel, A. Czyrska-Filemonowicz. *Microstructural changes during creep of CMSX-4 single crystal Ni base superalloy at 750°C*. J. Microsc., 237(3):364–369, 2010.

[219] C. Körner, M. Ramsperger, C. Meid, D. Bürger, P. Wollgramm,M. Bartsch, G. Eggeler. *Microstructure and Mechanical Properties of CMSX-4 Single Crystals Prepared by Additive Manufacturing*. Metall. Mater. Trans. A Phys. Metall. Mater. Sci., 49(9):3781–3792, 2018.

[220] H. Saage, M. Krüger, D. Sturm, M. Heilmaier, J.H. Schneibel, E. George, L. Heatherly, C. Somsen, G. Eggeler, Y. Yang. *Ductilization of Mo-Si solid solutions manufactured by powder metallurgy*. Acta Mater., 57(13):3895–3901, 2009.

[221] F. Kies, X. Wu, B. Hallstedt, Z. Li, C. Haase. *Enhanced precipitation strengthening of multi-principal element alloys by κ- and B2-phases*. Mater. Des., 198:109315, 2021.

[222] T. Boegelein, S.N. Dryepondt, A. Pandey, K. Dawson, G.J. Tatlock. *Mechanical response and deformation mechanisms of ferritic oxide dispersion strengthened steel structures produced by selective laser melting*. Acta Mater., 87:201–215, 2015.

[223] S.-K. Rittinghaus, M.B. Wilms. *Oxide dispersion strengthening of γ -TiAl by laser additive manufacturing*. Journal of Alloys and Compounds, 804:457-460, 2019.

[224] J. H. Perepezko. The hotter the engine, the better. Materials Science, 326(5956):1068–1069, 2009.

[225] T. Moriyama, K. Yoshimi, M. Zhao, T. Masnou, T. Yokoyama, J. Nakamura, H. Katsui, T. Goto. *Intermetallics Room-temperature fracture toughness of MoSiBTiC alloys*. Intermetallics, 84:92–102, 2017.

[226] N.J. Grant, O. Preston, F.V. Lenel. *Dispersed hard particle strengthening of metals*. JOM, 9(3):349–360, 1957.

[227] S. Yamasaki, M. Mitsuhara, K. Ikeda, S. Hata, H. Nakashima. *3D visualization of dislocation arrangement using scanning electron microscope serial sectioning method*. Scr. Mater., 101:80–83, 2015.

[228] G. Hasemann, I. Bogomol, D. Schliephake, P. I. Loboda, M. Krüger. *Microstructure and creep properties of a near-eutectic directionally solidified multiphase Mo-Si-B alloy*. Intermetallics, 48:28–33, 2014.

[229] J.H. Schneibel. *High temperature strength of Mo-Mo_3Si-Mo_5SiB_2 molybdenum silicides.* Intermetallics 11(7):625–632, 2003.

[230] J. Becker, D. Fichtner, S. Schmigalla, S. Schultze, C. Heinze, Y. Küsters, G. Hasemann, J. Schmelzer, M. Krüger. *Oxidation response of additively manufactured eutectic Mo-Si-B alloys*. IOP Conf. Ser.: Mater. Sci. Eng. 882:012002, 2020.

[231] A. Mukherjee, S. P. Wach. *Kinetics of the oxidation of vanadium in the temperature range 350-950°C*. J. Less-Common Met., 92(2):289–300, 1983.

[232] J. G. Keller. *The High-Temperature Oxidation Behavior of Vanadium-Aluminum Alloys*. Oxidation of Metals, 36:439–464, 1991.

[233] V. Supatarawanich, D.R. Johnson, C.T. Liu. *Effects of microstructure on the oxidation behavior of multiphase Mo-Si-B alloys*. Mater. Sci. Eng. A, 344(1-2):328–339, 2003.

[234] G. Hasemann, T. Baumann, S. Dieck, S. Rannabauer, M. Krüger. *Polymer-Derived Ceramics as Innovative Oxidation Barrier Coatings for Mo-Si-B Alloys*. Metall. Mater. Trans. A Phys. Metall. Mater. Sci., 46(4):1455–1460, 2015.

[235] M. Krüger, J. Schmelzer, I. Smokovych, J. Lopez Barrilao, G. Hasemann. *Processing of Mo silicide powders as filler particles in polymer-derived ceramic coatings for Mo-Si-B substrates*. Powder Technol., 352:381–385, 2019.

[236] A. Lange, R. Braun. *Magnetron-sputtered oxidation protection coatings for Mo-Si-B alloys*. Corros. Sci., 84:74–84, 2014.

[237] J.H. Perepezko. *Surface Engineering of Mo-Base Alloys for Elevated-Temperature Environmental Resistance*. Annu. Rev. Mater. Res., 45:519–542, 2015.

[238] A. Lange, M. Heilmaier, T.A. Sossamann, J.H. Perepezko. *Oxidation behavior of pack-cemented Si-B oxidation protection coatings for Mo-Si-B alloys at 1300°C*. Surf. Coatings Technol., 266:57–63, 2015.